Intrinsic Diversity in Hippocampal Neurons: Phenomenological and Integrative
Descriptions of Quantitative Dynamics

A dissertation submitted in partial fulfillment of the requirements for the degree of
Doctor of Philosophy at George Mason University

by

Siva Venkadesh Iyappan Latha
Master of Science
University of Georgia, Athens, 2012
Bachelor of Technology
College of Engineering, Guindy, 2007

Director: Giorgio A. Ascoli, University Professor
George Mason University

Spring Semester 2020
George Mason University
Fairfax, VA

DEDICATION

This dissertation is dedicated to my loving wife Alicia.

ACKNOWLEDGEMENTS

TABLE OF CONTENTS

LIST OF TABLES

LIST OF FIGURES

ABSTRACT

INTRINSIC DIVERSITY IN HIPPOCAMPAL NEURONS: PHENOMENOLOGICAL AND INTEGRATIVE DESCRIPTIONS OF QUANTITATIVE DYNAMICS

Siva Venkadesh Iyappan Latha, Ph.D.

George Mason University, 2020

dissertation Director: Dr. Giorgio A. Ascoli

Simulations of neural systems promise to offer powerful frameworks to formulate and test hypotheses about the physical interactions intrinsic to the brain. A comprehensive characterization of experimentally observed neuronal diversity using a modeling system is necessary to simulate biologically realistic brain networks at the cell type level. Biophysically detailed model descriptions typically limit the scalability of such network simulations as they specify hundreds of equations governing each neuron's intrinsic dynamics. On the other hand, simple phenomenological models, which compactly describe the patterns of neuronal excitability through dynamical bifurcations, often lack experimentally identifiable parameters. This makes it challenging for such models to quantitatively account for the intrinsic diversity experimentally observed among the neurons. In this work, compact model descriptions that comprehensively capture the intrinsic dynamical diversity observed among the rodent hippocampal

neurons are created. Both point-neuron and compact multi-compartment models are optimized using evolutionary algorithms. These optimized models reflect the intrinsic differences among hippocampal neuron types both qualitatively and quantitatively. In addition, this work describes the collective dynamics of an ensemble of bursting neurons based on their self-organizing properties. Measures are formulated to quantify the metastable nature of the neural ensembles. Such integrative descriptions of neuronal dynamics can complement their intrinsic descriptions to accurately simulate biological neural circuits.

CHAPTER 1: INTRODUCTION

The mammalian brain presents a multitude of challenges in the understanding of its complexity. The mouse brain contains approximately 70 million neurons (Herculano-Houzel et al., 2006), each making thousands of connections with other neurons. In addition, neurons have enormous diversity in their genetic expression, morphology, electrophysiology, and intrinsic dynamics (Wheeler et al., 2015). The number of neurons, whose activity can be recorded in parallel from an awake animal, is currently less than 1000 and is expected to double every seven years (Hong and Lieber, 2019; Stevenson and Kording, 2011). Such technological limitations hinder the experimental interrogation of large-scale neuronal interactions and highlight the importance of *simulating* those interactions in the brain. Thus, biologically realistic simulations of large-scale neuronal interactions are increasingly considered as necessary tools (Markram et al., 2015) to advance our understanding of the physics of the brain.

The goal of simulating a brain region requires precise descriptions of its individual components at a sufficient level of detail. Such descriptions include, but are not limited to, the morphological features of neurons that determine their connectivity structure and the ranges of their intrinsic dynamics. *Hippocampome.org*, a comprehensive knowledgebase of neuron types in the rodent hippocampal formation, identifies over 100 morphological types based on their axodendritic patterns across the

layers of the hippocampal formation (Wheeler et al., 2015) to describe their known and

potential connections (Rees et al., 2016). In addition, the knowledgebase describes the

ranges of passive and active electrophysiological, synaptic, and molecular properties for

each neuron type, based on tens of thousands of pieces of empirical evidence, assembled

from the peer-reviewed published literature.

The qualitative and quantitative differences in the intrinsic dynamics among

neurons result from specific combinations and distributions of various ion-channel

mechanisms along the soma, axons, and dendrites. Intrinsic dynamics of a neuron can be

mathematically described by the rules governing the kinetics of various ion channels

(Hodgkin and Huxley, 1952). However, morphologically detailed descriptions of intrinsic

dynamics, which typically include hundreds of equations, significantly limit the

scalability of the network simulations (Bezaire et al., 2016; Markram et al., 2015;

Morgan and Soltesz, 2008). On the other hand, phenomenological models, based on the

bifurcation mechanisms of neuronal excitability, such as the Izhikevich model (IM)

(Izhikevich, 2003), can compactly describe the intrinsic dynamics with only two

equations, thereby making them computationally desirable. However, the bifurcation

parameters of such models, which lack biological interpretability, need to be estimated in

order to account for the qualitative diversity and quantitative variability commonly

observed in the intrinsic dynamics of the neurons.

In the next three chapters of this dissertation, I address the problem of

phenomenologically describing the diverse intrinsic dynamics experimentally observed in

hippocampal neuron types. In chapter 2, I review different classes of models, which

include both biophysical and phenomenological descriptions, and their tradeoffs. Then, I summarize a previous method that systematically characterized the intrinsic dynamics of hippocampal neurons, in terms of their temporal patterns of activation (Komendantov et al., 2019). Finally, I describe computational modeling of intrinsic dynamics as an optimization problem and discuss relevant issues. Special emphasis is placed on the appropriate configuration of the evolutionary algorithm (EA) that respects the parameter interactions in the IM to robustly optimize its parameters.

In chapter 3, I present an optimization pipeline based on the EA to tune the nine parameters of the IM, to reproduce various temporal features of the experimentally identified spike patterns. The reliability of this technique is illustrated by modeling nine distinct classes of simple behavior phenotypes identified in (Komendantov et al., 2019). I also discuss how incorporating the spike-pattern class definitions into the fitness landscape can robustly identify a cloud of possibilities in the IM parameter space for a certain phenotype. In addition, I demonstrate the scalability of the approach by optimizing models with up to four compartments, which were simulated on CARLsim (Beyeler et al., 2015), a high-performance GPU-based simulator.

While chapter 3 presents models for simple-behavior neuron types that elicit qualitatively similar responses for different inputs, in chapter 4, I present a comprehensive list of models for 120 neuron types/subtypes identified in *Hippocampome.org*. This covers 45 unique spike-pattern phenotypes, which include phenotypes with qualitatively different response patterns under different inputs. Both

point-neuron and multi-compartment IM descriptions are publicly available at *Hippocampome.org*, with an online feature to simulate the point-neuron dynamics.

In addition to the model-fitting results, I report novel findings from various analyses, which include a comparison of descriptive powers between point-neuron and multi-compartment models, a comparison of dendritic integration properties between the optimized multi-compartment IMs and previously published morphologically detailed multi-compartment models, and correlation analysis between the bifurcation parameters of the IM and various biological features. The comprehensive mapping of 120 neuron types/subtypes as clouds of possibilities in the IM parameter space, provides sampling regions for neuronal groups to construct biologically realistic circuits of the rodent hippocampus.

While *precise* phenomenological descriptions of individual components, among other factors, are important for the scalable simulations of hippocampal circuits, such network simulations face further conceptual challenges. Biological neurons have intrinsic plasticity and exhibit flexible working ranges by adjusting their excitability levels (Marder, 2011; Marder and Goaillard, 2006). In addition, cortical network dynamics are homeostatically tuned to achieve self-organized criticalities (Ma et al., 2019). Therefore, integrative-level descriptions, such as the patterns of self-organization among neural ensembles, are valuable and could complement the descriptions of individual components to accurately simulate network dynamics. Toward this end, in chapter 5, I describe the low-dimensional interactions among the broad class of intrinsically bursting neurons within the conceptual framework of "metastability" (Freeman and Holmes, 2005; Tognoli

and Kelso, 2014). Bursting neurons are multiple-time-scale systems, where the fast-spiking dynamics are modulated by slower mechanisms. Bursting dynamics can also be characterized based on the complex periodic loops observed in the phase portrait of the IM. Here, I quantitatively describe and distinguish the metastability that emerges from the collective dynamics of different classes of neurons. Such quantitative descriptions of self-organization are useful to identify the optimal ranges in subregions of a high-dimensional network parameter space.

Finally, chapter 6 provides a summary of this dissertation. It also suggests a possible future direction with a brief literature review, which ties various chapters of this dissertation together. In addition, several supporting figures and tables are included in the appendix. Appendix also includes a paper that I coauthored, which details firing pattern identification protocols in detail.

CHAPTER 2: COMPUTATIONAL MODELING AS A MEANS TO DEFINING NEURONAL SPIKE PATTERN BEHAVIORS[⊥]

1. <u>Introduction</u>

Information processing in the nervous system is facilitated by the rich, intrinsic computational properties of the neurons. These properties are revealed in their excitability and various temporal patterns of activation. The precise timing of voltage spikes during this activation is crucial for the representation of information (Buzsáki & Chrobak, 1995; O'Keefe & Recce, 1993; Gütig & Sompolinsky, 2006). The patterns of these voltage spikes are distinguished by several qualitative features such as fast spiking, bursting, spike frequency adaptation, bursting followed by spiking, and latency to spike. In many cases, a neuron exhibits several of these features under different experimental conditions. Thus, a neuron can be qualitatively characterized by the set of all different experimentally observed spike pattern types, which defines its spike pattern behavior.

Computational simulations have been invaluable to the investigation of neuronal dynamics. Biophysically detailed Hodgkin-Huxley (Hodgkin & Huxley, 1952) type models have provided great insights into the computational properties of the neurons. Other simpler spiking models such as the Leaky Integrate and Fire models have been

used to investigate the collective dynamics of neurons in large networks. Several such abstract models have been proposed for different applications. A particular model becomes the choice for a study by taking into account the factors such as its biophysical meaning, simulation cost, and computational possibilities. Section 2 provides a brief background on the computational properties of a neuron and a survey of the existing abstract models that capture these properties in varying levels of detail.

Traditionally, morphology has been the major characterizing factor that defines a neuron type. From a modeling perspective, characterization based on electrophysiological properties such as membrane capacitance, time constant and spike amplitude might seem relevant. However, these properties are highly sensitive to the experimental conditions and hence, not very reliable. In addition, there could be several possible configurations of morphological and electrophysiological parameters that result in a single computational property. Therefore, in order to investigate the information processing in the nervous system, it is more useful and relevant to characterize the neuron types based on their spike pattern behaviors.

Of particular interest to this chapter is the representation of a neuron type as *possibilities* in an abstract model space, where these possibilities encapsulate its known behaviors. Such a representation is valuable for the following reasons: Firstly, it might provide key insights into the existence of computational subtypes within a certain morphologically characterized neuron type, or, it might suggest a new direction towards characterizing neurons entirely based on their detailed neuro-computational properties. Secondly, in order to create a biologically realistic large scale spiking neural network

(SNN) model of a brain region, the individual neuronal models in that SNN should accurately represent the complex behaviors exhibited by the real neurons. Definition of these behaviors in the model space offers a sampling region for the neurons in such large scale SNN simulations and allows one to investigate the collective dynamics of several neuron types with distinct behaviors. However, this requires a framework that allows a systematic analysis and categorization of different experimentally observed behaviors. One such framework is discussed in section 3. Finally, sections 4 and 5 discuss the overall strategy to model the spike pattern behaviors and the issues that need consideration.

2. <u>Computational model of a neuron</u>

Several abstract models have been proposed to capture the computational properties of a neuron in varying levels of detail. On one end, the Hodgkin-Huxley (HH) model (Hodgkin & Huxley, 1952), which is a four dimensional system, incorporates the persistent K^+ and transient NA^+ current dynamics in order to explain the generation of an action potential in a neuron. The HH model has been traditionally used to study the dynamics of a single neuron in detail at the level of ion channel gating mechanisms. On the other end, the leaky-integrate-and-fire model (LIF), which is described by a single linear differential equation, simply defines a spike event based on a voltage threshold. The LIF's have been widely used in SNN simulations to investigate the network level dynamics and to solve practical problems in machine learning (Gütig & Sompolinsky, 2006; Yu et al., 2014; Ghosh-Dastidar & Adeli, 2009). In between these two, there is a wide spectrum of models that capture the computational properties of real neurons to

8

different extents. In these models, the biophysical accuracy is usually traded off for a lower model simulation cost. The preference for a particular model might be made by weighing its biophysical details against its cost of simulation. However, the biophysical details are useful and relevant, when one is interested in investigating the factors that affect the single neuron dynamics such as the morphology of the neuron (Saraga et al., 2003), backpropagation of action potentials (Yu et al., 2008), or the ionic currents (Goldwyn & Shea-Brown, 2011). For other investigations, it is more meaningful to discuss the model preference in terms of the neuro-computational possibilities allowed in that system rather than its biophysical details.

2.1. Neuro-computational properties

Neuron is a dynamical system (Izhikevich, 2007) and the excitability of a neuron can be described by the bifurcation mechanisms revealed in its phase portrait (Izhikevich, 2000). The bifurcation from resting state of the membrane voltage (stable equilibrium) to repetitive spiking can be caused by a single parameter – the strength of the injected current. There are two major bifurcation mechanisms that broadly define the neuro-computational properties (Izhikevich, 2001): In a neuron that undergoes Andronov-Hopf bifurcation, perturbing the stable equilibrium results in a damped oscillation towards the resting state. In the case of saddle-node bifurcation, such perturbation results in an exponential convergence towards the resting state. The former is known as resonator neurons and the latter as integrator neurons. The resonators do not have a clearly defined voltage threshold to generate an action potential, whereas integrators do. An integrator's action potential is an *all-or-none* response, whereas a resonator can generate an action

potential with large or intermediate amplitude. An integrator's firing response is directly proportional to the frequency of the input signal. The resonators require specific frequency components in the input signal to elicit a response. In addition, inhibitory input signals can promote spiking response in resonators, whereas inhibition always impedes an integrator's response. Thus, these two classes differ in some of the fundamental neuro-computational properties. Apart from being an integrator or a resonator, the biological neurons also exhibit different qualitative neuro-computational features in their activation patterns such as bursting, bursting followed by spiking, spike frequency adaptation, and latency to spike. Therefore, a good abstract model of a neuron should be able to reproduce all of these features.

2.2. Biophysically meaningful models

The Hodgkin-Huxley model (Hodgkin & Huxley, 1952) precisely captures the mechanisms of action potential generation in a neuron. It describes the dynamics of membrane voltage (V) using voltage-gated Na^+ and K^+ currents and an Ohmic leak current (I_{Na}, I_K and I_l respectively):

$$C \cdot \frac{dV}{dt} = I - I_{Na} - I_K - I_l$$

$$I_{Na} = g_{Na} \cdot m^3 \cdot h \cdot (V - E_{Na})$$

$$I_K = g_K \cdot n^4 \cdot (V - E_K)$$

$$I_l = g_l \cdot (V - E_l)$$

Here, C is the membrane capacitance and I is the externally injected current. The transient I_{Na} is further described by the state variables corresponding to three activation gates (m) and one inactivation gate (h). Similarly, the persistent I_K is described by the

10

state variable corresponding to four activation gates (n). The variables m, h and n define the probabilities of opening/closing of their respective ion channels. E_{Na}, E_K and E_l are the Nernst equilibrium potentials. Although this four dimensional system can capture the rich neuro-computational properties of a biological neuron, it is computationally very expensive to simulate. Consequently, the HH type models are not ideal to be used to build large scale neural networks.

Another biophysically meaningful model was suggested by Morris and Lecar (ML) (Morris & Lecar, 1981), which reduced the HH model and included only two state variables. This model omitted the I_{Na} inactivation and approximated its activation by including an instantaneous Ca^{2+} current as follows:

$$C \cdot \frac{dV}{dt} = I - I_{Ca} - I_K - I_l$$

$$I_{Ca} = g_{Ca} \cdot M_\infty(V) \cdot (V - E_{Na})$$

$$I_K = g_K \cdot W \cdot (V - E_K)$$

$$I_l = g_l \cdot (V - E_l)$$

Here, the state variable W describes the probability that a K^+ channel is in open state and $M_\infty(V)$ describes the instantaneous I_{Ca} activation. Although the ML model reduces the dimensionality of the HH model, it requires a significantly small time step for the simulation in order to accurately reproduce the spike times (Izhikevich, 2004), which makes it still computationally expensive. In addition, this model does not capture spike frequency adaptation or tonic bursting.

2.3. Integrate and Fire (IF) Models

The simplest and one of the most widely used spiking models of a neuron is the leaky integrate and fire (LIF) model, which describes the membrane voltage (V) using only a leak current and a membrane time constant (τ). When V reaches a threshold level (V_t), it is instantaneously reset to a resting level (V_r), which marks a spike event.

$$\tau \cdot \frac{dV}{dt} = -(V - E_l)$$

$$if \; V \geq V_t \; then \; V = V_r$$

Although widely used in large scale SNN simulations due to its simplicity, this model cannot reproduce several important neuro-computational properties including bursting, spike frequency adaptation, or resonance. A few variations of the LIF model have been introduced in order to capture some of these properties. For instance an LIF with Adaptation adds another differential equation to incorporate spike frequency adaptation. Here, the dynamics of an activation gate is introduced (g), which decays with time constant τ after a spike event.

$$\tau \cdot \frac{dV}{dt} = -(V - E_l) - g \cdot (V - E_K)$$

$$\frac{dg}{dt} = \frac{e \cdot \delta(t) - g}{\tau}$$

Other variations of LIF such as IF-or-Burst (IFB) (Smith et al., 2000), Resonate-and-Fire (RF) (Izhikevich, 2001), and Quadratic IF (QIF) (Ermentrout, 1996) models add some neuro-computational properties to the basic LIF model. However, the QIF cannot reproduce bursting or resonance, the RF cannot reproduce spike frequency adaptation or be an integrator, and the IFB cannot reproduce subthreshold resonance or bursting

followed by spiking. Brette and Gerstner incorporated the features of Izhikevich model

(described below) into an IF model and created a two dimensional model known as

Adaptive Exponential IF (AdEx) (Brette & Gerstner, 2005). This model has not only

been shown to reproduce several neuro-computational properties qualitatively (Brette &

Gerstner, 2005), but also performed well in a quantitative single-neuron modeling

competition (Jolivet et al., 2008).

2.4. Izhikevich model

Izhikevich proposed a simple model (IM) of spiking neuron with two differential

equations (Izhikevich, 2003) and showed that this model was able to reproduce many

neuro-computational properties qualitatively. In addition to the membrane voltage (V), a

membrane recovery variable (U) was included in the equation as follows:

$$\frac{dV}{dt} = 0.04V^2 + 5 \cdot V + 140 - U + I$$

$$\frac{dU}{dt} = \boldsymbol{a}(\boldsymbol{b} \cdot V - U)$$

$$if\ V \geq\ 30mV\ then\ V = \boldsymbol{c},\ U = U + \boldsymbol{d}$$

The recovery variable U approximates the activation of I_K and the inactivation

of I_{Na} in the HH model. Similar to the IF models, it defines a spike cutoff value to reset

the state variables. The parameter *'a'* is the time constant for the recovery variable U.

The parameters '*b*' and '*a*' collectively determine whether the model is an integrator or

resonator. Typically, the model is an integrator, when $b < a$, and resonator when $b > a$.

The parameters *'c'* and *'d'* are after-spike reset values for V and U respectively. The

resting voltage in this model is between -70 mV and -60 mV depending on the value of

'b'. A slight variation of this model conveniently includes additional parameters such as resting voltage (V_r), threshold voltage (V_t) and cell capacitance (*C*) without affecting its computational efficiency (Izhikevich, 2010):

$$\boldsymbol{C} \cdot \frac{dV}{dt} = \boldsymbol{k} \cdot (V - \boldsymbol{V_r}) \cdot (V - \boldsymbol{V_t}) - U + I$$

$$\frac{dU}{dt} = \boldsymbol{a} \cdot \{\boldsymbol{b} \cdot (V - V_r) - U\}$$

$$if\ V = \boldsymbol{V_{peak}}\ then\ V = \boldsymbol{c},\ U = U + \boldsymbol{d}$$

The parameter *'k'* defines the shape of the spike upstroke and V_{peak} defines the spike cutoff value.

Unlike the biophysically detailed models, the IM has been shown to capture several neuro-computational properties with a very low simulation cost (Izhikevich, 2004). Consequently, this model has been used in a number of large scale SNN simulations (Izhikevich & Edelman, 2008; Beyeler et al., 2014; Nageswaran et al., 2009). Therefore, the IM is the most appropriate choice if one wants to build a large scale SNN with neuro-computationally diverse single neuron models. However, to create such diversity, the nine parameters of this model that collectively determine its neuro-computational properties, need to be known.

Qualitatively characterizing the neuro-computational properties as tonic spiking or bursting is useful to evaluate different abstract models as done in (Izhikevich, 2004). However, the real neurons exhibit more complex behaviors like bursting and spiking with frequency adaptation under different current stimulation levels (e.g. CA1 Neurogliaform neuron). Therefore, before truly exploring the neuro-computational possibilities in the

parameter space of the IM, one needs a systematic approach to classify the known spike

pattern types and categorize different behaviors of real neurons. The following section

discusses one such framework developed in a previous work.

3. <u>Spike pattern behaviors</u>

In a previous work (Wheeler et al., 2015), more than 100 neuron types in the

rodent hippocampal formation were identified based on their axonal and dendritic

locations across the hippocampal layers. A knowledge base (Hippocampome.org) was

created and it includes the morphological, electrophysiological and molecular marker

evidences for all neuron types, where information is available in the literature.

Experimentally recorded voltage traces of these neuron types were analyzed and a firing

pattern classification scheme was developed based on the presence of transient/steady-

state and silence/spiking/bursting components in a firing pattern (Komendantov et al.,

2019) (Table 2.1). Consequently, more than 10 different firing pattern types were

identified among all the hippocampal neuron types. Representative cases for different

spiking and bursting/stuttering pattern types are listed in tables 2.2 and 2.3 respectively. It

should be noted that a neuron type can exhibit more than one of these types under

different experimental conditions (e.g. different levels of current injection). For instance,

a CA1 Bistratified interneuron elicited spike trains of the types D.PSTUT and D.NASP at

400pA and 600pA current injection levels respectively (Pawelzik et al., 2002). The set of

all different spike pattern types known to be elicited by a neuron type defines its

behavior. However, since these neuron types have been primarily characterized based on

morphology, one must consider the possibility of electrophysiological subtypes in the

context of spike pattern behaviors.

Table 2.1: A scheme for firing pattern classification

	Transient response	Steady-state response
Silence	Delay (D)	Silence (SLN)
Spiking	Adapting Spiking (ASP)	Non-Adpating Spiking (NASP)
Bursting	Transient Stuttering (TSTUT), Transient Slow Wave Bursting (TSWB)	Persistent Stuttering (PSTUT), Persistent Slow Wave Bursting (PSWB)

As listed in table 2.4, a neuron type belongs to the 'multi-behavior' category,

when a single neuron of that type is known to elicit two different firing pattern types (e.g.

D.NASP and NASP for two different current injection levels). If different neurons of the

same type elicited different firing pattern types for the same current injection level under

identical experimental conditions, then electrophysiological 'subtypes' exist for that

neuron type. If the current injection levels were different in this scenario, the existence of

subtypes is not conclusive, since it could also be a multi-behavior neuron type ('subtypes

or multi-behavior').

Table 2.2: Exemplar spiking pattern types in the hippocampus
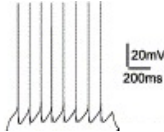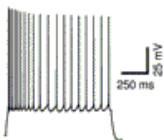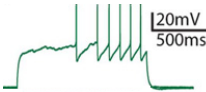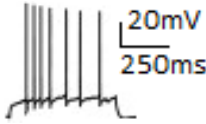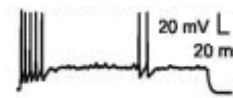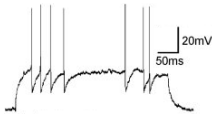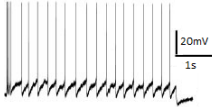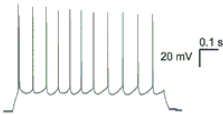
Firing pattern type *Neuron type**	Experimental recording
NASP *CA1 BC CCK+ (i)2232* (Cope et al., 2002)	
ASP.NASP *CA3 Pyramidal (e)23223p*** (Podlogar & Dietrich, 2006)	
D.NASP *DG Neurogliaform (i)3000p* (Armstrong et al., 2011)	
D.ASP.NASP *CA2 Pyramidal (e)2333p* (Chevaleyre & Siegelbaum, 2010)	

Table 2.3: Exemplar bursting/stuttering pattern types in the hippocampus

Firing pattern type *Neuron type**	Experimental recording
PSTUT *CA2 SP-SR (i)-0302* (Mercer et al., 2012)	
D.PSTUT *CA1 Bistratified (i)0333* (Pawelzik et al., 2002)	
TSTUT.NASP *EC - LV Deep Pyramidal (e)-220033* (Hamam et al., 2002)	
TSWB.NASP *CA1 Pyramidal (e)2223p* (Zemankovics et al., 2010)	

17

ASP.SLN
MEC LV Superficial PC
(e)213330
(Canto & Witter, 2012)
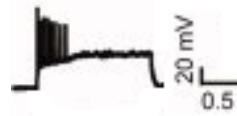
TSWB.SLN
CA3 Pyramidal
*(e)23223p***
(Chevaleyre &
Siegelbaum, 2010)

* Naming scheme for neuron types is based on (Wheeler et al., 2015);
Note that firing pattern identification protocols have been updated since the publication of this chapter. See (Komendantov et al., 2019) for the most recent firing pattern classes
** Neuron *sub*types

Table 2.4: Possible categories of behavior for a neuron type 'N' that exhibited more than one firing pattern type

Scenario	Behavior category	Response of neuron N_1		Response of neuron N_2	
		For I_1	For I_2	For I_1	For I_2
1	Recording from a single neuron	**Multi-behavior**	FPT_1	FPT_2	-	-
2		**Subtypes**	FPT_1	-	FPT_2	-
3	Recordings from multiple neurons	**Subtypes and Multi-behavior**	FPT_1	FPT_3	FPT_2	-
4		**Subtypes or Multi-behavior***	FPT_1	-	-	FPT_2

FPT: Firing pattern type, *I*: Input current injection level, N_1 and N_2 are two different neurons of the type *N*. * Non conclusive category. It also includes the cases where the recordings were made under different experimental conditions regardless of the current injection levels (e.g. different room temperatures, different animal species)

Finally, a neuron type can also satisfy the criteria for both 'subtype *and* multi-behavior'. Definition of spike pattern behaviors in the IM parameter space might give useful insights into the 'subtypes *or* multi-behavior' category. For instance, if different spike pattern types of a behavior from the 'subtypes *or* multi-behavior' category cannot be reproduced in a single IM, it might suggest the existence of computational 'subtypes' within that neuron type. However, one must also take into account the possible limitations of the IM in these cases. From a modeling perspective, this requires optimization and exploration of the IM parameters. The next two sections discuss various methodologies to achieve this and the associated challenges in the context of parameter optimization.

4.   <u>Evolutionary algorithm as a tool for modeling neuronal dynamics</u>

An Evolutionary algorithm (EA) is a powerful tool to tackle optimization problems. The EA is guided by a fitness function, which is used to evaluate the quality of the points in the parameter search space. The objective of using an EA for an optimization problem is usually concerned with choosing the appropriate type of the algorithm and its configuration, and the definition of the fitness function. The possible choices for an EA include, but not limited to, genetic algorithm (GA), evolutionary strategies (ES), genetic programming (GP), and particle swarm optimization (PSO). Each of these nature-inspired algorithms has their own set of features, but they all have a common core template: A population of candidate solutions goes through small changes

for several iterations in order to explore and exploit the search space with the guidance of a fitness function.

4.1. Model optimization using the EA

A number of studies have addressed the optimization problem in the context of neuronal models and different approaches for tuning the model parameters have been discussed in the literature. With the goal of fitting the model responses to voltage traces recorded from the biological neurons, these studies mainly differ in the following details: (a) the choice of the optimization algorithm, (b) the type of the neuronal model used and (c) the fitness function definition.
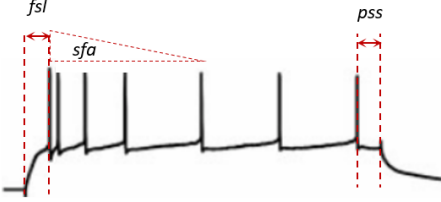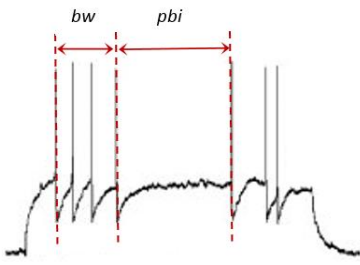
On the model spectrum, simple models such as the adaptive IF, adaptive threshold IF, adaptive exponential IF and Izhikevich models have been optimized using the GA and PSO (Rossant et al., 2010; Lynch & Houghton, 2015; Rossant et al., 2011). The parameters of the biophysically meaningful models such as ML and HH with multiple compartments have also been optimized using the GA and ES (Gerken et al., 2006; Van Geit et al., 2007; Karen et al., 2005; Druckmann et al., 2007). However, the major aspect that characterizes these studies is the fitness function which defined the objectives. As mentioned before, the goal of this optimization problem is to create models whose responses are close to the experimentally recorded voltage traces. There are different ways to capture this goal in the fitness function. One approach is to directly compare the points of the experimental voltage trace with those of the model response. The problem with this approach is that the fitness function becomes very sensitive to small time shifts in the spike train (Van Geit et al., 2008; LeMasson & Maex, 2001). Another similar

20

approach called the phase plane trajectory density (PPTD) method avoids this problem (LeMasson & Maex, 2001). The PPTD method excludes the time parameter and plots two time-dependent variables such as the voltage $V(t)$ and its first derivative dV/dt for the comparison. Using this method as a fitness measure, a Purkinje cell model with 1600 compartments and 24 free parameters has been tuned (Van Geit et al., 2007). The effects of using different fitness functions on the performance of the GA for a HH model with 19 free parameters has been studied in (Karen et al., 2005): These functions were based on direct comparison of voltage traces, the PPTD method, and the comparison of inter-spike intervals. The fitness function that combined all these three modes of analysis was shown to be the most effective. Another approach is to use the features of a spike pattern such as spike frequency, AP width, and AP overshoot in the fitness function (Druckmann et al., 2007). The major advantage of this approach is that the features can be selectively included in the fitness function. For instance, if one decides that the shape of the spike upstroke is not relevant to their study, and only interested in reproducing a certain spike frequency, the fitness function can be configured accordingly. In (Gerken et al., 2006), the input current – firing frequency curve was used to tune the ML model with six free parameters. Finally, the possibility of using spike coincidences as the fitness measure has been explored with IF and Izhikevich models (Rossant et al., 2010; Lynch & Houghton, 2015; Rossant et al., 2011). This approach was based on the number of coincidences between the experimentally recorded spikes and the model spikes, where coincidences were defined using a small temporal window. On a benchmark dataset, this approach worked well with the IF models, but performed poorly with the Izhikevich model.

4.2. Feature-based fitness function

As an optimization problem, the objective here can be broadly defined as follows: implement a fitness function that can reduce the model error in terms of spike times. However, as mentioned earlier, the spike pattern behaviors are characterized by the higher level temporal features such as first spike latency (*fsl*) and spike frequency adaptation (*sfa*). Therefore, it is useful to include these features in the fitness function rather than the spike times. This allows one to give importance to one feature over the other by assigning different weights to their respective errors. In addition, the right combination of these features can implicitly represent the original goal of reproducing accurate spike times. As an example, consider the experimentally recorded voltage trace from a CA3 pyramidal neuron given in table 2.5 (top trace (Hemond et al., 2008)). The spike times of this pattern can be implicitly represented as objectives by simply including the following features as described in the table: *fsl*, *pss*, *sc* and *sfa* during the first five spikes. Thus, the fitness function for such an *ASP.NASP* pattern could be defined as $-\sum_{f \in S} w_f . E_f$, where $S: \{fsl, sfa, pss, sc\}$, and w and E are the weight and the error associated with a feature. However, this fitness function will not work for a spike pattern of the type D.PSTUT (table 2.5, bottom trace (Pawelzik et al., 2002)), which will require its own set of features in order to capture its spike times. For such a stuttering or bursting spike pattern, additional features such as *bc, bw,* and *pbi* as described in table 2.5 should be included in the fitness function. Therefore, for each of the different spike pattern types, a minimal set of higher level temporal features to be used as fitness measures, needs to be identified.

Table 2.5: Possible quantitative features of spike patterns to be included in the fitness function

Spike pattern	Features
	First spike latency **(fsl)**: Duration between the onset of input current stimulation step and the first spike
	Post spike silence **(pss)**: Duration between the last spike and the end of input current stimulation step
	Spike count **(sc)**: Number of spikes recorded
	Spike frequency adaptation **(sfa)**: Reduction in the frequency of spikes following the first spike
	Burst count **(bc)**: Number of bursts recorded. A burst is a cluster of high frequency spikes followed by a period of quiescence
	Burst width **(bw)**: Duration of a burst
	Post burst interval **(pbi)**: Duration of quiescence following the burst

4.3. Fitness landscape with a feature based function

To our knowledge, optimization algorithms have not been successfully used to fit the IM responses to experimental voltage recordings. As mentioned before, on a benchmark optimization test, the IM performed poorly using an EA compared to the Adaptive, Adaptive threshold, and Adaptive exponential IF models (Rossant et al., 2010; Lynch & Houghton, 2015; Rossant et al., 2011). The major factor that affects the performance of an EA is the nature of the problem fitness landscape. The fitness landscape is the hypersurface in the parameter search space and it defines the relationship

between the parameters and the fitness value. As the search for the optimal parameters is guided by this landscape, its topographical features directly affect an EA's performance. These features can be used to assess the computational complexity of an optimization problem (Chiong, 2009) and knowledge about the fitness landscape will be helpful in choosing the appropriate algorithm and its configuration.

The major problem that any EA faces is the premature convergence to local optima (Eshelman, 2014). This happens when the population of candidate solutions reaches fitness peaks that are better than the neighboring regions, but are not the globally best. If all the candidate solutions reach the same local optimum, there is very little chance of further exploration of the search space by the algorithm. This problem is more severe in the rugged landscapes (Kolarov, 1997), which contain several of these locally optimal peaks. The parameters of the IM create such rugged regions in the fitness landscape (fig. 2.1). In these landscapes, the gradient information about the fitness is not very reliable and this has a negative effect on the performance of the EA.
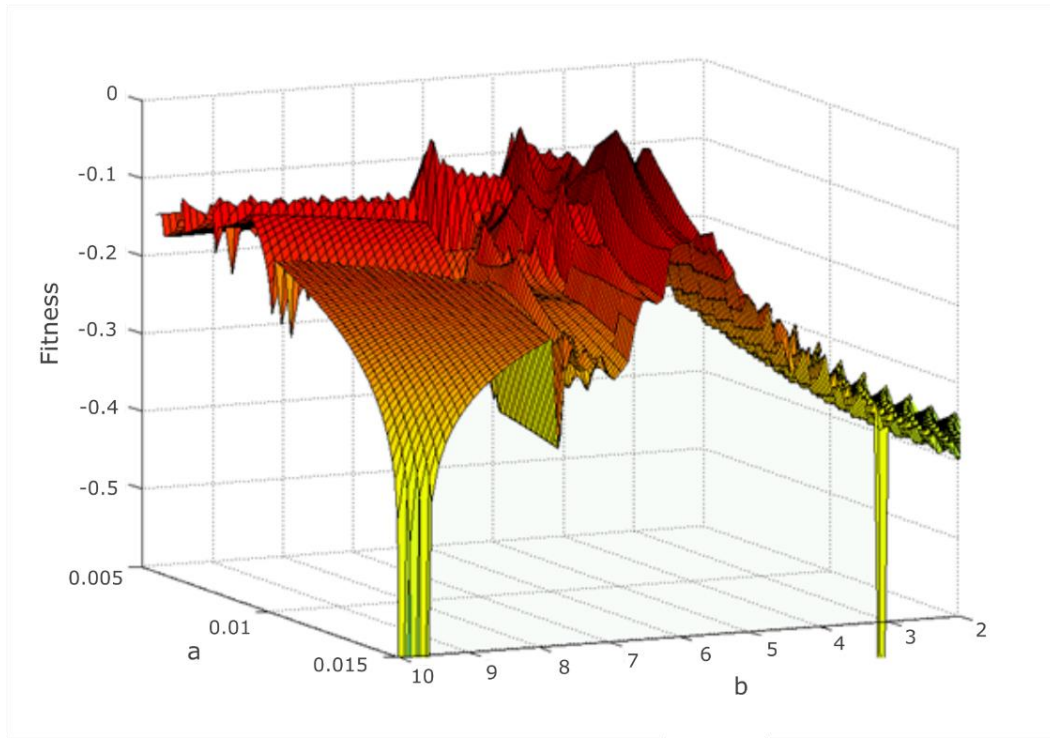
Figure 2.1: A rugged region in the fitness landscape created by the IM parameters 'a' and 'b'.
The fitness function included errors on features fsl, sfa, pss, sc as described in section 4.1 for the trace given in table 1.5 (top). Fitness values range from 0.

Another problem is the epistatic interaction among the parameters in creating the fitness landscape. In the context of optimization, epistasis is defined as the dependency of a parameter's contribution to the fitness value on the state of other parameters. The higher the epistatic interactions among the parameters, the harder it is for the EA to optimize them (Davidor, 1991). There are strong interactions among the Izhikevich model parameters to create a fitness landscape, and an example is given in (fig. 2.2). The region shaded in blue corresponds to the model responses that are not biologically valid, hence it is assigned the lowest fitness value. As obvious from this figure, this region is not defined independently by the parameters 'k' *or* 'Vt', but collectively by *both* 'k' *and* 'Vt'.

Therefore, independently varying one of these genes might break the building blocks representing such interaction. Finally, the noise introduced in the fitness landscape creates a different problem. Fitness is evaluated by comparing the model responses with the experimentally recorded spikes. Since these electrophysiological recordings are not completely devoid of measurement errors, the resulting fitness landscape might not be an accurate representation of the theoretical objective we would want to achieve.
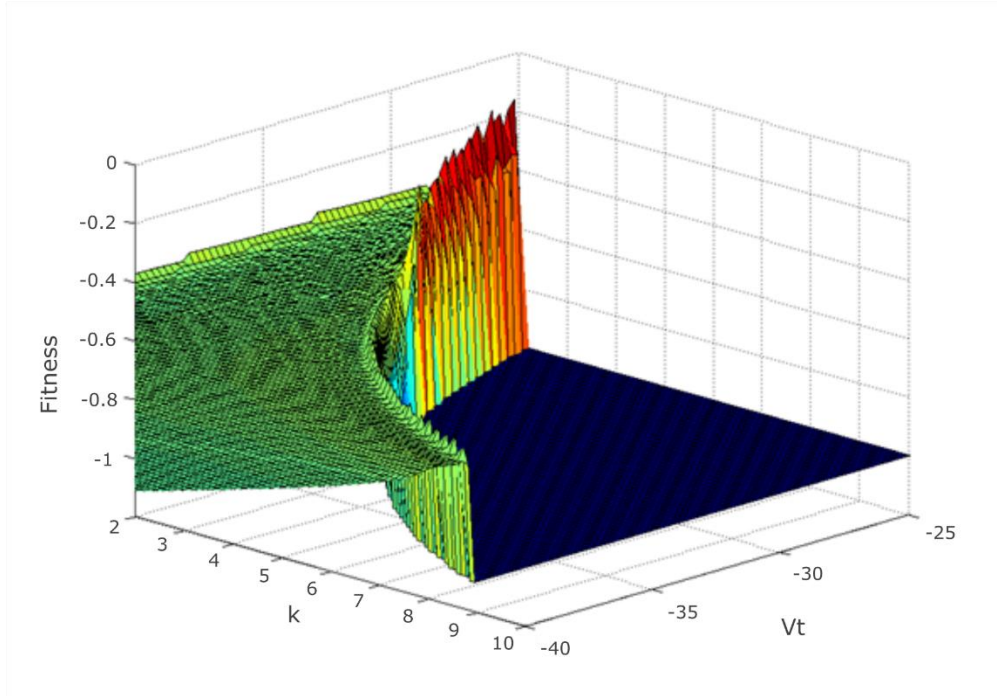
Figure 2.2: Epistatic interaction between the parameters 'k' and 'Vt' to define invalid region (shaded in blue) in the parameter space.

It is necessary to consider the facts discussed above when configuring the EA to optimize the IM parameters. There is no practicable method that directly solves the problem of premature convergence caused by the rugged landscapes. Maintaining

diversity in the population has been shown to be a general strategy to avoid premature convergence to the local optima. However, it is crucial to achieve the right balance between exploration and exploitation of the search space (De Jong, 2006). For instance, too much selection pressure with very little mutation might exploit only the local regions without really exploring other regions of the search space. On the other hand, too much mutation with very little selection pressure would always explore different regions without really climbing to their peaks. Therefore, a proper balance between the mutation/crossover operations and the selection pressure might mitigate the effects of rugged fitness landscapes. Knowledge of epistatic interactions among the parameters will be helpful to devise schemes that could prevent building blocks from being destroyed by the variation operators such as crossover. Although there is no guarantee, appropriately configuring an EA with the knowledge of the problem landscape maximizes its chances of reaching the global optimum.

5. <u>Modeling spike pattern behaviors</u>

The goal of the problem under discussion is not just to fit IM responses to the experimental voltage recordings. It is to characterize the neuron types in terms of IM parameters and their relationships that define their behaviors. Although developing a strategy that can fit IM responses to individual voltage traces (as discussed in section 4.1) is a necessary objective, modeling a behavior requires further considerations, which are discussed below.

5.1. Optimization objectives with a behavior

A neuron type can exhibit more than one firing pattern type as listed in table 1.4. The set of all different firing pattern types exhibited by a neuron type under different experimental conditions (such as different input current injection) defines its behavior. For example, the CA1 Bistratified neuron is known to produce the firing pattern type D.PSTUT (table 2.5, bottom trace (Pawelzik et al., 2002)). In addition, a firing pattern of the type D.NASP has also been recorded from this neuron type (Pawelzik et al., 2002). The objectives of modeling such behaviors can be defined in the fitness function in one of many ways. One method is to extend the approach described in section 4.1, and simply sum up the weighted feature errors across multiple firing pattern types. However, this approach will not be very useful and informative with cases where there are conflicting objectives in the fitness function. Before pointing out and illustrating an alternate approach, it is useful to consider the scenarios that could possibly create such conflicting objectives. As explained in section 2.2, modeling the spike pattern behaviors might give useful insights into the 'subtype *or* multi-behavior' class of neuron types. If a neuron type indeed has multiple subtypes, then the voltage traces recorded from these different subtypes might be computationally impossible to be represented in a single IM, and thus creating conflicting objectives. With this consideration, an alternate approach to define such objectives is to use the Multi Objective Optimization (MOO) (Deb, 2001; Coello et al., 2002).

The MOO is a useful technique to deal with conflicting objectives. Rather than trying to find a single optimal solution for a problem, the MOO attempts to find a Pareto

front of optimal solutions, where optimality is defined by the notion of 'dominance': A candidate solution *'A'* dominates another candidate solution *'B'*, if and only if *'A'* is not worse than *'B'* in all objectives, and *'A'* is strictly better than *'B'* in at least one objective. Thus, in a MOO with conflicting objectives, the candidate solutions that are *not* dominated by others form the Pareto front of solutions. In principle, features of a single experimental voltage trace (e.g. *fsl, sc,* and *pss* from a recording of type D.NASP) could be viewed as the multiple objectives for the MOO. However, considering the rich dynamics of Izhikevich model, there might not necessarily be any trade-off between the features of a single spike pattern. In other words, the features *fsl* and *sc* are not conflicting objectives in a D.NASP voltage trace when Izhikevich model is used. Such tradeoffs are more likely to occur among the objectives across different firing pattern types. For instance, one may try to fit a single model to both NASP and TSWB.NASP pattern types by only varying the input current, which might not be possible in the IM. However, trying to do so with the MOO might give useful insights into the nature of trade-off among the features that characterize these spike pattern types.

5.2. Parameter space exploration

Besides conflicting objectives, one must also take into account the possible inadequacy of objectives while constraining a model. Several neuron types have not been investigated in detail in the literature, and as a result, the available experimental evidences might not be sufficient to create accurate model representations. These cases should be viewed as a parameter exploration problem rather than an optimization. The EA's have been largely used as the parameter optimizers with the goal of reaching a

single global optimum. However, their optimization capability highly relies on their ability to effectively explore the parameter space. In principle, due to their stochastic nature, an appropriately configured EA should be able to reach multiple global optima across different trials.

As an illustration, the EA was run to optimize the IM parameters (including the input current) for arbitrarily defined feature constraints for four different spike pattern types. Across different stochastic trials, the EA identified multiple points in the search space that reproduced these constraints (fig. 2.3A). Representative model response for each spike pattern type is given in fig. 2.3B. Some observations could be made from this figure from the point of view of the spike pattern behaviors. Although only a weak adaptation was added to the NASP constraints in order to produce an ASP.NASP pattern, these two patterns were clearly separated in the IM parameter space. Very few neuron types have been known to exhibit 'multi-behavior' with these two spike pattern types. However, more definite constraints need to be defined for each spike pattern type to explore the possibilities of such behaviors in the IM parameter space.
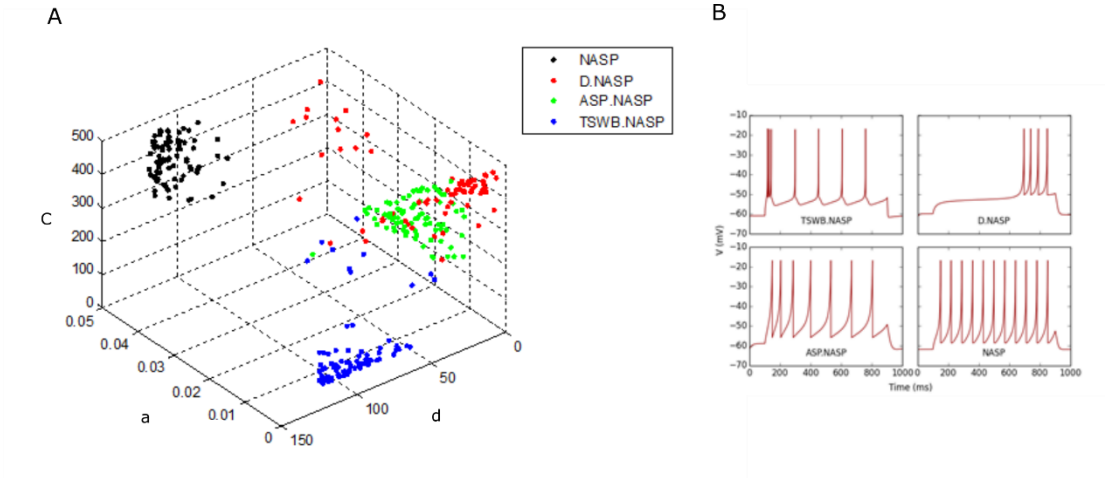
Figure 2.3: Parameter space exploration with stochastic EA trials
A: Regions in the IM parameter space representing four different spike pattern types. Only the dimensions 'C', 'a', and 'd' are shown. B: Representative IM responses for four spike pattern types TSWB.

6. <u>Summary</u>

In sum, defining spike pattern behaviors in the IM parameter space might reveal their characterizing features and will help to fill the gap in the knowledge about certain behaviors. In addition, this will be valuable to large scale SNN simulations that aim to investigate the collective dynamics of several neuron types with distinct behaviors. In order to create a biologically realistic, but computationally efficient SNN, its individual neuron models should capture the complex behaviors of the real neurons. Achieving this goal will provide a platform to develop theories that could causally link the neuro-computational properties at neuronal level to network behavior and to the emerging computational properties at the network level. This requires techniques that are not only capable of optimizing the model parameters, but also capable of effectively exploring the parameter space.

CHAPTER 3: EVOLVING SIMPLE MODELS OF DIVERSE INTRINSIC DYNAMICS IN HIPPOCAMPAL NEURON TYPES[1]

The diversity of intrinsic dynamics observed in neurons may enhance the computations implemented in the circuit by enriching network-level emergent properties such as synchronization and phase locking. Large-scale spiking network models of entire brain regions offer a platform to test theories of neural computation and cognitive function, providing useful insights on information processing in the nervous system. However, a systematic in-depth investigation requires network simulations to capture the biological intrinsic diversity of individual neurons at a sufficient level of accuracy. The computationally efficient Izhikevich model can reproduce a wide range of neuronal behaviors qualitatively. Previous studies using optimization techniques, however, were less successful in quantitatively matching experimentally recorded voltage traces. In this article, we present an automated pipeline based on evolutionary algorithms to quantitatively reproduce features of various classes of neuronal spike patterns using the Izhikevich model. Employing experimental data from Hippocampome.org, a comprehensive knowledgebase of neuron types in the rodent hippocampus, we demonstrate that our approach reliably fit Izhikevich models to nine distinct classes of

experimentally recorded spike patterns, including delayed spiking, spiking with adaptation, stuttering, and bursting. Importantly, by leveraging the parameter-exploration capabilities of evolutionary algorithms, and by representing qualitative spike pattern class definitions in the error landscape, our approach creates several suitable models for each neuron type, exhibiting appropriate feature variabilities among neurons. Moreover, we demonstrate the flexibility of our methodology by creating multi-compartment Izhikevich models for each neuron type in addition to single-point versions. Although the results presented here focus on hippocampal neuron types, the same strategy is broadly applicable to any neural systems.

1. **Introduction**

In the last decade, several projects have built large-scale models of brain regions in an attempt to advance our understanding of how the nervous system functions (Izhikevich & Edelman, 2008; Eliasmith et al., 2012; Markram et al., 2015; Hendrickson et al., 2016). The biological realism in these models has been captured in varying levels of detail. One of the characterizing features of biological neural networks is the diversity observed in the intrinsic dynamics of individual neurons. This diversity likely contributes to the emergent properties of neural networks and, consequently, plays a major role in the information processing in the nervous system (Padmanabhan & Urban, 2010; Tripathy et al., 2013; Pozzorini et al., 2015). Therefore, a biologically realistic large-scale network model of a brain region should take into account intrinsic behavioral diversities both within and between neuron types.

Hippocampome.org is a comprehensive knowledgebase of 122 morphologically identified neuron types in the rodent hippocampal formation (Wheeler et al., 2015). One of the motivations behind developing this knowledgebase was to create a real-scale computational model of the entire hippocampus. Towards achieving this goal, we aim to create individual neuronal models using the electrophysiological and spike pattern properties of neuron types available at Hippocampome.org. In deciding which modeling system to use, we considered simulation costs. High simulation costs of biophysically detailed Hodgkin-Huxley-type neuronal models often impose limits on the scale of network models. Conversely, simpler models, such as leaky integrate-and-fire neurons, cannot capture the wide range of dynamics observed in the hippocampus. Models such as Izhikevich (Izhikevich, 2003) and Adaptive Exponential Integrate-and-Fire (AdEx) (Brette & Gerstner, 2005) have been shown to qualitatively reproduce various firing pattern classes observed experimentally in real neurons, while still being computationally efficient. Therefore, these simpler models with lower simulation costs allow large-scale modeling of biological neural networks in a computationally efficient manner. In this work, we create Izhikevich Models (IMs) that reproduce quantitatively comparable features of various hippocampal spike pattern classes through parameters optimization.

The dynamics of Izhikevich models are highly nonlinear and error landscapes that are defined over the resulting parameter spaces typically exhibit properties that make them difficult to optimize, such as multiple local optima. As such, several studies have turned to non-convex, derivative-free optimization methods such as evolutionary algorithms (EAs) to fit a neuronal model's responses to experimentally recorded voltage

traces. The models used in these studies range from simple spiking models such as AdEx (Rossant et al., 2010, 2011; Lynch & Houghton, 2015) to biophysically detailed Hodgkin-Huxley type models with multiple compartments (Keren et al., 2005; Gerken et al., 2005; Druckmann et al., 2007; Geit et al., 2007). Previous studies have also used various techniques such as a feature-based error function (Druckmann et al., 2007) and a phase plane trajectory density method (Geit et al., 2008) to create the error landscape for the EA search. Rössert et al. (2016) created an approach to simplify morphologically detailed microcircuit models to their point-neuron counterparts by applying soma-synaptic correction (to account for dendritic attenuation and delay) and constraining Generalized Integrate-and-Fire neurons around an *in vivo*-like working point. Rounds et al. (2016) used EAs to match firing rates of IMs in a network to experimental recordings in the retrosplenial cortex. However, to our knowledge, optimization techniques have not been successfully used to fit intrinsic IM responses to experimental data. On benchmark optimization tests, the IM showed poor performance compared to other simple models (Rossant et al., 2010, 2011; Lynch & Houghton, 2015). This might be due to the failure to identify an appropriate EA configuration such as the choice of error function and variation operators that are well-suited for the IM parameter space.

Apart from its capability to quantitatively fit IM's responses to experimental voltage traces, the novelty of our automated modeling framework is the integration of spike pattern classification protocols. Previous work (Komendantov et al., 2017) identified 23 distinct spike pattern classes overall, among the 89 morphologically distinct hippocampal neuron types in Hippocampome.org for which experimental recordings

were available. A behavior for a certain neuron type was defined based on the set of all experimentally recorded spike patterns. If a neuron type exhibited spike patterns of more than one class under different experimental conditions (e.g. bursting and regular spiking for different current stimulation strengths), it was marked as a multi-behavior type. In contrast, a neuron type was marked as a single-behavior type, if all spike patterns recorded from the same neuron under different experimental conditions fell into the same qualitative class. Neuron types with only a single experimentally recorded spike pattern were also marked as single-behavior.

This article presents the modeling approach and results for single-behavior neuron types. We report at least one example for each of the nine distinct single-behavior types, with the goal of illustrating both the approach and the IM's ability to quantitatively reproduce a variety of neuronal behaviors observed in the hippocampus. The single behaviors reported here include spiking with and without frequency adaptation, delayed spiking, bursting, and intermittent spiking or stuttering. In addition to simple point-neuron (single-compartment) models, multi-compartment IMs were created, where the number of compartments varied from two to four depending on the dendritic invasion of a neuron type across hippocampal layers. For example, the somata of hippocampal pyramidal cells in the principal layer extend basal dendrites in the oriens layer and apical trees in the radiatum layer that reach to the lacunosum-moleculare. Thus, these neurons can be represented as 4 compartments, one for each layer (as illustrated in the Methods below). This stratification is important because it segregates the synaptic inputs: distal lacunosum moleculare dendrites, for example, are the targets of entorhinal projections,

36

while dendrites in radiatum receive intra-hippocampal connections. Although finer morphological variability observed across various neuron types may also contribute to network dynamics, compartmentalized dendritic integration of distinct laminar inputs is likely to play a crucial computational role in cortical circuits. Furthermore, dendrites located in separate layers typically have different active and passive properties from each other and from the soma. A previous large-scale model of the thalamo-cortical system used multi-compartment IMs (Izhikevich & Edelman, 2008). However, that model did not capture the signal transmission properties between the dendrites and soma in a biologically accurate way. In addition, the dendritic compartments did not reflect the appropriate balance of active and passive properties. Another novelty of our automated modeling approach is its capability to create accurate dendritic representations in the multi-compartment IMs. Our dendritic compartments exhibit generally known active and passive properties of the dendrites of real neurons.

2. Materials and Methods

In this article, a certain spike pattern class will be used to denote a neuron type's "behavior," since all the neuron types discussed here were examples of single-behavior types. It is worth mentioning that 14 of the 23 distinct spike pattern classes observed in the hippocampus are part of the multi-behavior types and, hence, not reported in this article. Modeling multi-behavior cases requires a different approach, which we are pursuing but remains beyond the scope of this article.

2.1. Spiking Model

We reproduced spike patterns by using the nine-parameter variant of the IM (Izhikevich, 2007) because we found that the EA could reliably find better solutions with this IM than the originally proposed four-parameter formalism. IMs have been shown to reproduce qualitatively many spike patterns observed in biological neurons. The state variables membrane voltage (V) and membrane recovery variable (U) govern this two-dimensional system. The recovery variable U approximates the channel kinetics of Hodgkin-Huxley type models (Hodgkin and Huxley, 1952), making it computationally much cheaper to simulate. Parameter 'a' is the time constant for the recovery variable U. Parameter 'b' defines the degree of coupling between the state variables V and U. Parameters 'b' and 'a' collectively determine whether the model is an integrator or resonator (Izhikevich, 2001). Parameters 'V_{min}' and d' are after-spike reset values for V and U, respectively. Parameter 'k' defines the shape of the spike upstroke, and V_{peak} defines the spike cutoff value. Parameters V_r and V_t are resting and threshold voltages, respectively, and C is cell capacitance.

$$C \cdot \frac{dV}{dt} = k \cdot (V - V_r) \cdot (V - V_t) - U + I \tag{1}$$

$$\frac{dU}{dt} = a \cdot \{b \cdot (V - V_r) - U\} \tag{2}$$

$$if\ V = V_{peak}\ then\ V = V_{min},\ U = U + d$$

In addition, we created multi-compartment (MC) models for each neuron type based on the dendritic invasion across the hippocampal layers (Figure 3.1), whereas each compartment represents the part of the dendritic tree present in a given layer.

Compartments were coupled using an asymmetric mechanism. For example, the MC layout for the CA2 pyramidal neuron type depicted in Figure 1 defines the compartment-specific coupling currents as follows:

$$I_{SP} = G_1 \cdot P_1 \cdot (V_{SP} - V_{SO})$$

$$+G_2 \cdot P_2 \cdot (V_{SP} - V_{SR}) \tag{3}$$

$$I_{SO} = G_1 \cdot (1 - P_1) \cdot (V_{SO} - V_{SP}) \tag{4}$$

Here, Stratum Pyramidale (*SP*) denotes somatic compartment, and Stratum Oriens (*SO*), Stratum Radiatum (*SR*) and Stratum Lacunosum-Moleculare (*SLM*) (Figure 1) are dendritic compartments. I_{SP} is the total coupling current at compartment *SP*, which results from the differences in the voltage between *SP* (V_{SP}) and *SO* (V_{SO}), and between *SP* and *SR* (V_{SR}). G_1 and G_2 are coupling constants, and P_1 and P_2 (with values between 0.01 and 0.99) determine the degree of asymmetry in the coupling, where a value of 0.5 denotes symmetric coupling.
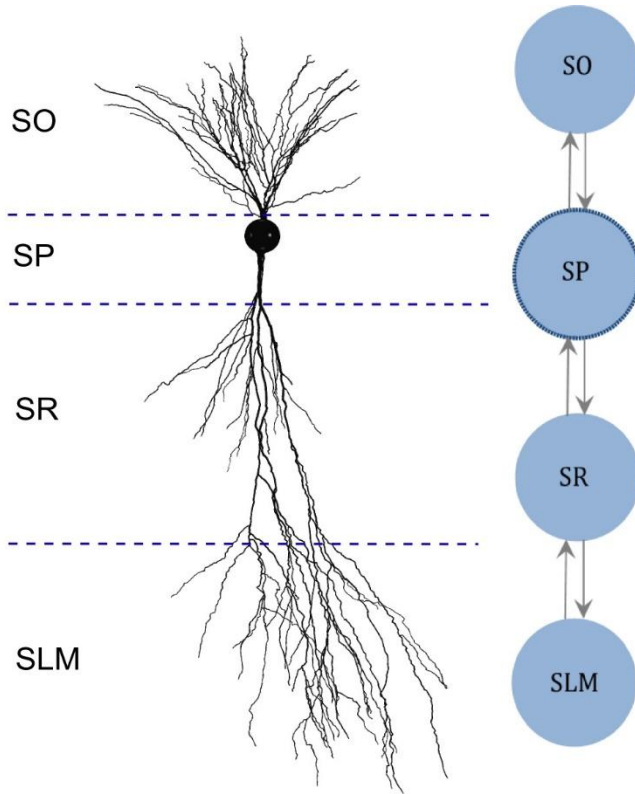
Figure 3.1: Multi-compartment model layout based on the morphology
(Left) Digitally reconstructed morphology of a CA2 pyramidal neuron (Wittner and Miles, 2007), reproduced from Neuromorpho.org (Ascoli et al., 2007). Layer boundaries are approximate. (Right) Layout of the multi-compartment model for CA2 Pyramidal neuron type. The number and the layout of compartments are determined based on the invasion of dendrites across the layers of CA2. SO, Stratum Oriens; SP, Stratum Pyramidale; SR, Stratum Radiatum; SLM, Stratum Lacunosum-Moleculare.

2.2. Identification of spike pattern classes

To classify the model behaviors, we used the same protocol developed for identifying various transient and steady-state elements of experimentally recorded spike patterns from the hippocampus (Komendantov et al., 2017). Transient elements include: Delay (D), if the latency to spike is sufficiently long; Adapting Spiking (ASP), if the spike frequency decreases over time; Transient Stuttering (TSTUT), if a quiescent period follows a cluster of high frequency spikes; and Transient Slow-Wave Bursting (TSWB),

if TSTUT is followed by a slow after-hyperpolarizing potential. Steady-state elements include: Silence (SLN), if the quiescence following the last spike is sufficiently long; Non-Adapting Spiking (NASP), if no spike frequency adaptation is identified in non-interrupted firing; Persistent Stuttering (PSTUT), if at least one sufficiently long quiescent period separates two clusters of high frequency spikes; and Persistent Slow-Wave Bursting (PSWB) if slow after-hyperpolarizing potential is present in an otherwise PSTUT pattern.

Given a sufficiently long duration of input current, transients will always be followed by a steady-state in a spike pattern. For example, ASP followed by NASP was identified in the spike pattern experimentally recorded from a CA3 Basket-CCK neuron (Szabo et al., 2010) and this pattern is an instance of the class ASP.NASP (Figure 3.2A). The identified class of an experimentally recorded spike pattern represented the target class for model spike pattern. Thus, the criteria that defined a target class were used to validate the model behavior under the given input current. For details on the spike pattern classification criteria, see Komendantov et al., (2017) and Hippocampome.org[1].

2.3. Evolutionary optimization of model parameters

Many varieties of EAs exist along with numerous ways of implementing their specific components (De Jong, 2006). We employed a non-overlapping generational model of evolution and used elitism to ensure that the best individuals were always preserved in the population. In this section, we describe the specific components of the EA.

---

[1] http://hippocampome.org/php/Help_Principles_of_Classification_of_Firing_Pattern_Elements.php
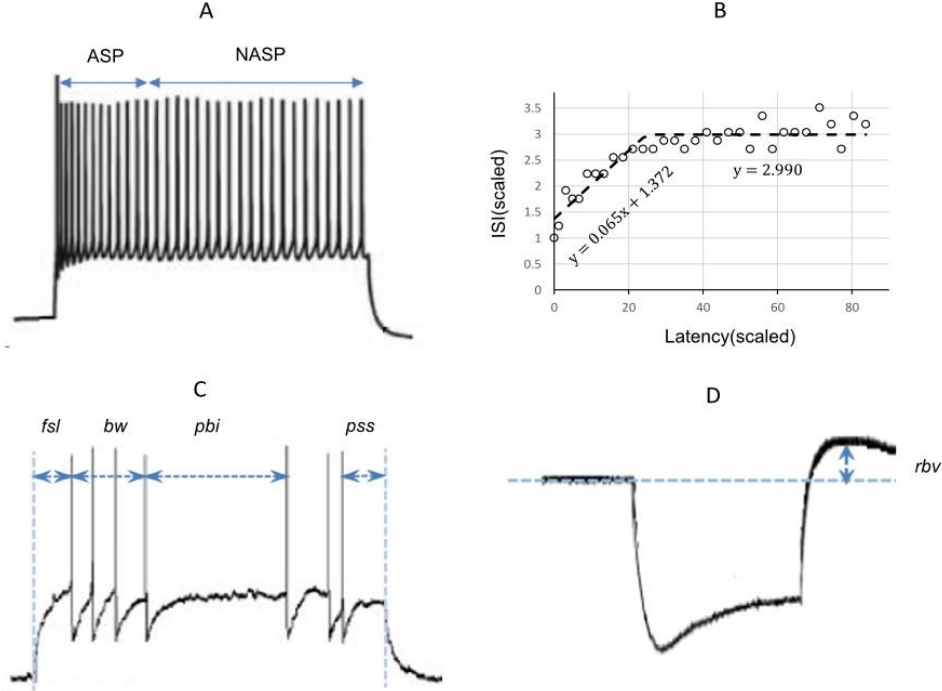
Figure 3.2: Characterizing features of neuronal spike patterns and subthreshold voltage traces
(A) A spike pattern trace recorded from a CA3 Basket-CCK neuron (Gulyás et al., 2010; Hippocampome.org) exhibiting a transiently adapting spiking (ASP.) behavior followed by a steady-state non-adapting spiking behavior (NASP), which is an instance of the class "ASP.NASP." (B) The adapting behavior is quantified by plotting inter-spike intervals (ISI) against their latencies and extracting the parameters of piecewise linear fits, such as slopes and Y-intercepts. (C) Stuttering behavior of a CA1 Bistratified neuron (Pawelzik et al., 2002; Hippocampome.org). *fsl*, first-spike latency; *pss*, post-spike silence. The features *bw* (burst width), and *pbi* (post-burst interval) characterizes the stuttering behavior. (D) A subthreshold voltage trace recorded from a CA1 OR-LM neuron (Oliva et al., 2000; Hippocampome.org) for a hyperpolarizing current stimulation. The difference between the resting potential and the peak voltage *(rbv)* after the current stimulation stops characterizes the rebound behavior of this neuron.

2.4. EA configuration

Each individual in the evolutionary population consisted of a complete

configuration of the IM we are seeking to tune. We represented these configurations as

vectors of floating-points. During the search of the parameter space, we bounded each

value within an allowed range. Choosing a biophysically reasonable range for each

parameter up front has a significant effect on the efficiency of the optimization

procedure, and through preliminary EA runs, we found that different behavior classes required slightly different ranges for some parameters.

When tuning a single-compartment model, each parameter vector contained $9+n_I$ elements (genes), representing the 9 parameters of the IM ($k, a, b, d, C, V_r, V_t, V_{peak}, V_{min}$) and n_I input currents. n_I equaled the number of voltage traces (which were recorded for different input currents) a model was fit to. A small range encompassing each experimentally injected input current ($I_{exp.}$), $[I_{exp.} - 10, I_{exp.} + 10]$ pA was included in the EA search. By allowing the EA to search within a small range, we boosted the exploration and identified more optimal points (across multiple EA trials) that are very similar in the phenotype. This design also helped to achieve more reliable fitting in cases where a single model was fit to multiple traces (See section 3.2). In rare cases, where the experimental input current was unknown, an unbounded range of $[50, 800]$ pA was included for the search. The multi-compartment models had a larger number of parameters: if c is the number of compartments, we require $8c+1$ parameters representing c compartments (the parameter V_r is the same for all c compartments), plus $2(c-1)$ parameters representing coupling parameters for consecutive compartment pairs, and n_I input currents.

We first initialized a population of these vectors by sampling uniformly from within each parameter's allowed range. We used a fixed population size of 120 individuals for single-compartment IMs and of 400 for multi-compartment IMs. An exception was the 4-compartment ASP.SLN fast-spiking model, which we found was easier to optimize with a larger population size (800). After initializing the population,

and at each generational cycle thereafter, we immediately selected the 10% of the population with the lowest error to survive to the next generation.

We filled the remainder of the child population by selecting parents via binary tournament and by applying two-point crossover and a mutation operator. Each gene had a probability of mutation between 0.1 and 0.3. For the parameters *d, C, G,* and *I,* we applied an integer random-walk mutation: when selecting one of those genes for mutation, an integer increment or decrement was applied with equal probability. All remaining parameters were mutated by reset: a new floating-point value was randomly chosen out of that gene's allowed range. The EA was run until a maximum number of generations was reached. This number varied between 500 and 5000 depending on the number of compartments in the model and the class of behavior the model was fit to.

2.5. Error function

We employed a feature-based error function to quantitatively reproduce the spike pattern. Features for more than 250 experimentally recorded spike patterns are available at Hippocampome.org. These features include first-spike latency (*fsl*), post-spike silence (*pss*), spike frequency adaptation parameters (*sfa*), burst width (*bw*), post-burst interval (*pbi*) and rebound voltage amplitude (*rbv*) (Figure 2). Spike frequency adaptation (*sfa*) was quantified as previously detailed (Komendantov et al., 2017) with a piecewise linear regression on the inter-spike intervals (ISIs) by extracting the parameters of linear fits such as slopes (*m*) and Y-intercepts (*c*) (Figure 3.2B). The error in the model *sfa* was calculated as follows: the two parameters of linear fit (for NASP and ASP. class) or three parameters of piecewise linear fits (for ASP.NASP class) obtained by plotting ISI's

against their latencies to the second spike were compared between experimental and model spike patterns. In addition, the number of ISIs (*nisis*) corresponding to a linear fit was also compared. For a bursting/stuttering class, the number of bursts (*nbs*) and the number of spikes (*nspikes*) within each burst were included.

Spike pattern classification protocols were also incorporated into the error function by dynamically assigning different weight factors to different features. This reduced the number of generations required for the EA to find an acceptable solution. In addition, for certain spike pattern classes, this approach more reliably found solutions across multiple stochastic trials. The error function was defined as:

$$error = \sum_{f \in S} \left(W_f \times \log \left(1 + |exp_f - model_f| \right) \right) \qquad (5)$$

S: $\{fsl, pss, m, c, nisi\}$ for continuous spiking, and

S: $\{fsl, pss, nbs, bw, pbi, nspikes\}$ for interrupted spiking (Figure 2).

Using the spike pattern classification protocols, the qualitative class of a candidate model's spike pattern was first identified. Then, the weight factor W_f was calculated for each feature by comparing the target class with the model spike pattern class During the EA search, each feature weight changed based on that feature's distance from the target class boundary. These class boundaries are given by the set of criteria that define that class (see supplementary material section 1 for pseudocode description of feature weight calculation). This accelerated the search during earlier generations of an EA, when many candidate solutions were outside the target class boundary (fast-exploitation towards

45

narrow regions of interest). Once the population began converging within the target class boundary, this dynamic weight assignment scheme allowed slower exploration and ensured heterogeneity among the best models from within a class (see Results section 3.4).

In order to identify several possibilities, we ran a total of one thousand EA instances for each neuron type, yielding several best models due to the stochastic nature of the EA (different initial populations, stochasticity in variation operators, and selection pressure). At the end of an EA search, the best model was accepted only if its spike pattern class under the given input current matched the target class. If a single-compartment IM failed to reproduce a firing pattern class, two identical compartments were symmetrically coupled. We noticed that coupling effects enriched IM dynamics and were useful to reproduce certain subclasses of stuttering behavior (see Results section for examples).

The parameters of MC models were optimized such that the somatic compartment reproduced features of the experimentally recorded voltage traces both qualitatively and quantitatively using the same techniques discussed previously for single-compartment models. Furthermore, four additional constraints were enforced in order to capture the known general active and passive properties of dendrites in the additional compartments. Unlike the somatic compartment constraints, all MC models shared the same dendritic constraints because of the lack of sufficient experimental dendritic voltage recordings. These general constraints include excitability and input resistance of dendrites relative to the soma as well as forward propagation of spikes and subthreshold signals.

Firstly, the dendritic compartments in MC models were constrained to be less

excitable than the somatic compartment when they were decoupled. The minimum

depolarizing current (I^{rheo}) required to elicit a spike at a compartment was used as the

measure of its excitability (Aou et al., 1992). During the EA search, a ramp current rather

than step currents was used to measure compartment excitabilities. This avoided the need

for a local search for the minimum step current magnitude required to elicit a spike in

each compartment. To reduce capacitive effects in measuring excitability, the ramp

current had minimal slopes and high resolution of discrete increments ($+0.1$ $pA/1$ ms).

Secondly, the decoupled dendritic compartments in MC models were constrained to have

higher input resistances than the somatic compartment. The amplitudes of steady state

voltage deflections from resting voltage (V^{def}) during a strong hyperpolarizing current

input were compared between compartments to measure their relative input resistances.

The spike propagation rate (R) was defined as the ratio between the number of spikes

observed at the destination compartment and the number of spikes initiated at the source

compartment. A few hundred excitatory synapses were stimulated at a dendritic

compartment for spike initiation. On the other hand, a single AMPA synapse was

stimulated at a dendritic compartment and the amplitude of the excitatory post synaptic

potential ($EPSP$) was measured at the somatic compartment. A range of (0.1, 0.9) mV

was enforced for the $EPSP$ amplitude. All synapses used a value of 10 for the weight,

and this value is based on the range used for the multicompartment models by Izhikevich

et al. (2008). The following errors were calculated for each dendritic compartment and

added to the somatic spike pattern error described earlier:

$$error_{rheo} = \begin{cases} 0, I_{dend}^{rheo} \geq I_{soma}^{rheo} \\ \log\left(1 + \left(I_{soma}^{rheo} - I_{dend}^{rheo}\right)\right), I_{dend}^{rheo} < I_{soma}^{rheo} \end{cases} \quad (6)$$

$$error_{vdef} = \begin{cases} 0, V_{dend}^{def} \geq V_{soma}^{def} \\ \log\left(1 + \left(V_{soma}^{def} - V_{dend}^{def}\right)\right), V_{dend}^{def} < V_{soma}^{def} \end{cases} \quad (7)$$

$$error_R = \begin{cases} 0, R = 1 \\ \log\left(1 + (1 - R)\right), R < 1 \end{cases} \quad (8)$$

$$error_{epsp} = \begin{cases} 0, 0.1 \leq EPSP \leq 0.9 \\ \log\left(1 + (0.1 - EPSP)\right), EPSP < 0.1 \\ \log\left(1 + (EPSP - 0.9)\right), EPSP > 0.9 \end{cases} \quad (9)$$

2.6. Model and algorithm implementations

We used the open-source Java-based evolutionary computation system ECJ (Luke et. al, 2015) to tune IM parameters. Single compartment models were simulated using the Apache Commons Mathematics Library[2]. The MC models with up to 39 open parameters were tuned using the parameter tuning interface of CARLsim, an open-source high performance GPU-based spiking neural network simulator (Beyeler et al., 2015). The EA and the single compartment model simulations were run on distributed CPU nodes, and the MC models were run on the GPU nodes available at the Office of Research

---

[2] http://commons.apache.org/proper/commons-math/

Computing at George Mason University. All scripts necessary to reproduce the results reported in this article are publicly available[3].

3. <u>Results</u>

3.1. Models of distinct single behavior types

A total of 33 of 122 neuron types in Hippocampome.org version 1.0 (Wheeler et al., 2015) exhibit single behavior. Nine distinct single-behavior *classes* exist among these neuron types, and, in this article, we present at least one model for each of those classes. It is worth mentioning that different neuron types that exhibit the same qualitative behavior class typically exhibit different quantitative features and excitability levels. Figure 3.3 illustrates an exemplar neuron type for each of the nine distinct single-behavior classes and the corresponding best model from all EA trials. Our simple models were able to reproduce quantitatively comparable spike pattern features for all these classes (see section 3.2 for quantitative comparison). While earlier models reproduced seven qualitatively different classes of spike patterns (Izhikevich, 2003), our models capture the spike pattern features of all observed single-behavior spike patterns in hippocampal neuron types both qualitatively and quantitatively. Importantly, our systematic and more detailed spike pattern classification identifies distinct hippocampal spike pattern classes within general firing behaviors (Komendantov et al., 2017). For instance, among the adapting spike patterns, our approach distinguishes between the patterns that reach a specific steady state such as non-adapting or silence (ASP.NASP and ASP.SLN classes, respectively) and those with experimental recordings that only allow

---

[3] https://github.com/Hippocampome-Org/Time

determination of the transient state (ASP. class). Our models effectively reproduced the

features of these classes (Figure 3: ASP., ASP.SLN, and ASP.NASP).
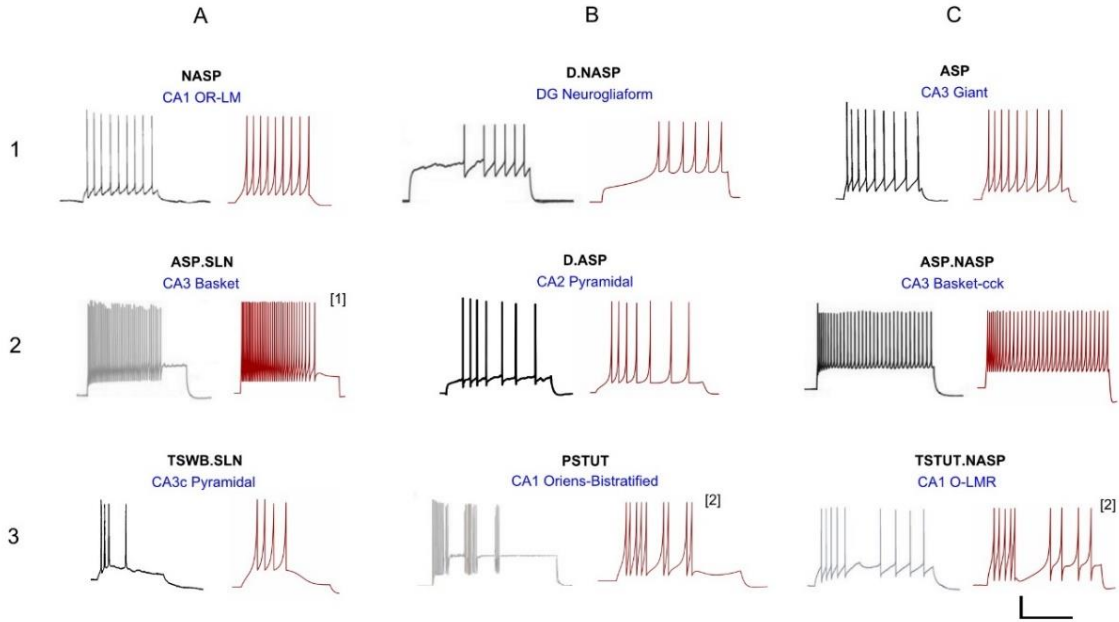
Figure 3.3: Models reproducing the diverse hippocampal spike pattern classes.
Candidate neuron type models for each spike pattern class are displayed as the best IM response across several stochastic EA trials (red traces) along with the corresponding experimental recordings (black traces) digitized by Hippocampome.org from various published sources. The IMs accurately reproduce the features of spike patterns for all classes. Both the experimental and model traces were classified using the same protocols (Komendantov et al., in review). Source of the experimental traces and their calibrations: (1A) Oliva et al. (2000); 25 mV, 350 ms. (1B) Armstrong et al. (2011); 25 mV, 450 ms. (1C) Savić and Sciancalepore (2001); 25 mV, 400 ms. (2A) Gulyás et al. (2010); 20 mV, 400 ms. (2B) Chevaleyre and Siegelbaum (2010); 20 mV, 200 ms. (2C) Gulyás et al. (2010); 25 mV, 300 ms. (3A) Buckmaster et al. (1993); 30 mV, 80 ms. (3B) Chittajallu et al. (2013); 12 mV, 300 ms. (3C) Ali and Thomson (1998); 30 mV, 350 ms. [1] Fast-spiking model with a minimum instantaneous spike frequency of 21 Hz. [2] Two-compartment IM with homogeneous compartments and symmetric coupling. All the other IMs are single-compartment models.

All models shown in Figure 3.3 are single compartment IMs except for PSTUT

and TSTUT.NASP, which were reproduced by coupling two homogenous compartments.

Although stuttering behavior can be modeled in a single compartment IM, multiple

compartments (coupling effects) were required to accurately capture various subclasses

of stuttering behavior such as TSTUT.NASP and TSTUT.ASP. However, the number of compartments for a multi-compartment IM is determined based on the neuronal morphology (see section 2.1) and CA1 O-LMR and CA1 Oriens-Bistratified neurons have both their soma and dendrites in the oriens layer. Thus, MC models were created by symmetrically coupling two identical compartments, unlike the MC IMs with morphologically defined layouts (section 3.3). These two-compartment IMs were able to capture the classes PSTUT and TSTUT.NASP by integrating coupling effects into the IM dynamics. For the EA search, this simply means inclusion of an additional parameter (coupling constant). In many cases, the EA population converged in less than 500 generations, but certain classes required more generations (Figure 3.4). As mentioned in section 2.3.2, we reject the best solution found from a single EA run, if its spike pattern features do not meet the target class criteria (see section 3.5 for discussion on the number of accepted models for different classes). The IM parameters of the nine models from Figure 3.3 are given in Table 3.1.

3.2. Quantitative comparison of spike pattern features

Our approach can reliably fit a model's responses to multiple experimental voltage traces. As an illustration, the model of a CA1 OR-LM neuron type (a variant of the O-LM interneuron superfamily with dendrites in oriens and axons in both radiatum and lacunosum-moleculare) was created by fitting its responses to four distinct experimental voltage traces recorded for different current stimulation strengths (Figure 3.5A). The model reproduces features of spike pattern and subthreshold voltage traces that are quantitatively comparable to the experimental traces (Table 3.2). The model

spike pattern features are reported for the input currents that were selected by the EA (see

Methods). In addition, only the minimum set of features required to fully capture the

temporal properties of spike patterns were included in the error function. For instance,

single spike traces do not require *pss* as an objective feature, when *fsl* and *nspikes* are

included. By allowing a narrow range for input current, the EA was able to reliably fit the

model responses to multiple voltage traces. Although the voltage sag is not as clearly

visible as in the hyperpolarized experimental trace, the corresponding model response

nevertheless has a post-inhibitory rebound potential with a 7 *mV* amplitude. It should be

noted that for multiple voltage trace fitting, we only considered traces that were recorded

under the same experimental conditions (except for the strength of current stimulation),

such as animal species (rat vs mouse), electrode type (patch vs sharp), and temperature
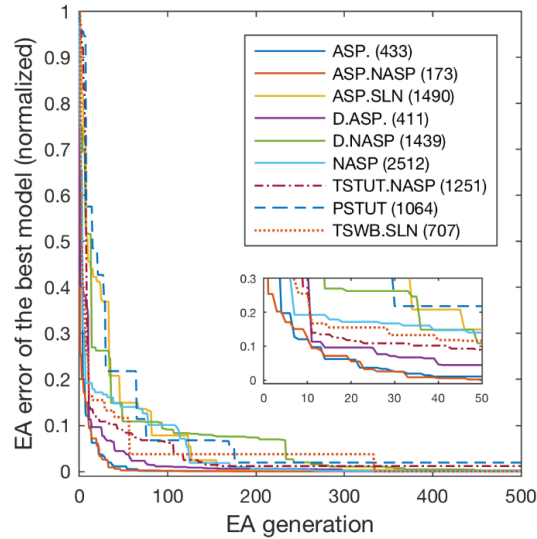
Figure 3.4: Evolution of best models for different spike pattern classes.
The EA was run for 500 generations for the classes ASP. and ASP.NASP, 3,000 generations for NASP and ASP.SLN and 2,000 generations for the remaining classes. Errors typically improved at higher rates in earlier generations, when

models that satisfy target class criteria were found. Improvements in the error beyond 500 generations were generally small and not shown here. The number next to each class label denotes the last generation of error improvement for that class. Inset zooms-in the first 50 generations.

(room vs body). As mentioned in section 3.1, our approach does not only differentiate between different classes of frequency adapting spike patterns, but also reproduces quantitatively comparable parameters of sfa (Figure 3.5B). See supplementary material (section 2) for quantitative comparison between experimental and model traces for all nine classes from figure 3.3.

Furthermore, our approach does not simply identify a single optimal point in the IM parameter space, but instead identifies several possibilities that correspond to the known behaviors of a certain neuron type. The size of such region of possibilities in the parameter space depends on the target behavior class to which the model is constrained as well as the amount of experimental data available for each neuron type. For instance, NASP behavior roughly correspond to the range (0.01, 0.1) for the IM parameter 'a,' whereas ASP., especially a strongly adapting behavior, significantly reduces the possibilities to the range (0, 0.005) for 'a.' Similarly, if multiple experimental voltage traces were recorded for different input current strengths, the possibilities in the IM parameter space are reduced.

Table 3.1: IM parameters for the nine models from Figure 3.3

Neuron type	k	a	b	d	C	Vr	Vt	Vpeak	Vmin	G
CA1 OR-LM (NASP)	0.527	0.00223	6.15	-12	253	-57.25	-42.78	81.81	-44.97	-
DG Neurogliaform (D.NASP)	0.697	0.00107	-30.65	111	242	-74.15	-9.20	17.51	-39.44	-
CA3 Giant (ASP.)	0.609	0.00365	1.84	2	96	-57.58	-37.12	36.42	-49.45	-
CA3 Basket (ASP.SLN)	0.995	0.00385	9.26	-6	45	-57.28	-23.16	18.68	-47.33	-
CA3 Basket-CCK (ASP.NASP)	0.583	0.00574	-1.24	54	135	-59.00	-39.40	18.27	-42.77	-
CA2 Pyramidal (D.ASP.)	5.943	0.00114	-15.89	74	1630	-72.59	-58.78	19.99	-62.65	-
CA1 O-LMR (TSTUT.NASP)	0.326	0.00632	0.40	48	96	-56.44	-27.62	29.48	-51.29	12.00
CA3c Pyramidal (TSWB.SLN)	3.006	0.00189	19.36	104	244	-62.29	-45.27	17.43	-47.37	-
CA1 Oriens-Bistratified (PSTUT)	2.91	0.00168	13.67	35	841	-57.11	-48.50	4.12	-52.94	67.00
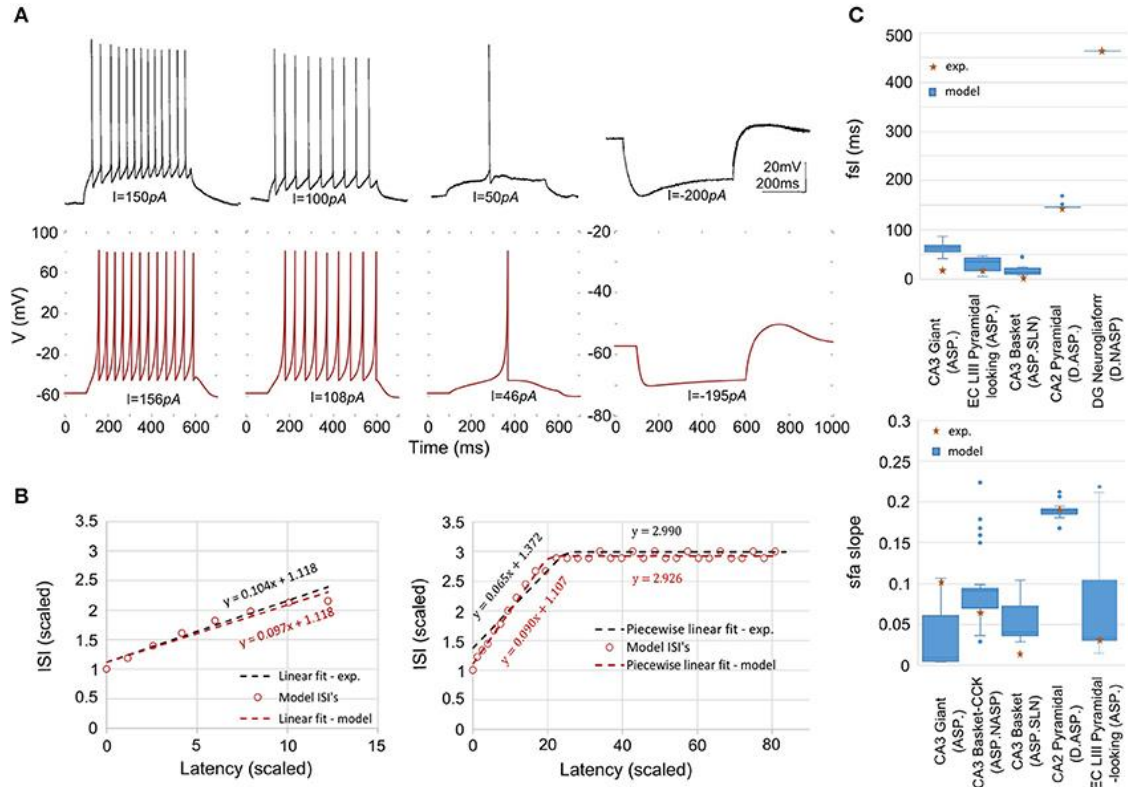
Figure 3.5: Models quantitatively reproducing the features of experimentally recorded spike pattern traces.
(A) Experimental recordings from a CA1 OR-LM neuron (Oliva et al., 2000) for four different current stimulation strengths (top). The IM reproduces the features quantitatively for similar input currents (bottom). Refer to Table 2 for numerical comparison. (B) The IM *sfa* is fit to the experimentally observed *sfa* from a CA3 Giant neuron to generate a spike pattern of class ASP. (left). The IM quantitatively reproduces the ASP.NASP behavior of a CA3 Basket-CCK neuron (right). The slope(s), Y-intercept(s) and the number of ISI's extracted from the experimental linear fit/piecewise linear fits were used as model constraints. (C) The ranges of *fsl*'s (top) and of *sfa* slopes (bottom) exhibited by the accepted IMs for various neuron types.

Table 3.2: Quantitative comparison of spike pattern features between experimental and model traces of the CA1 OR-LM neuron type given in Figure 3.5A.

	I		150pA	100pA	50pA	-200pA
	fsl		40.1ms	30.39ms	200ms	-
	pss		18.38ms	7.31ms	-	-
Exp.	sfa:	c	1.176	1.196	-	-
		nISI	12	8	-	-
	rbV		-	-	-	7mV
	nSpikes		-	-	1	-

55

Model	I		156pA	108pA	46pA	-195pA
	fsl		58.9ms	79.9ms	268ms	-
	pss		8.9ms	3.1ms	-	-
	sfa:	c	1.176	1.198	-	-
		nISI	11	8	-	-
	rbV		-	-	-	7mV
	nSpikes		-	-	1	-

The variability in the quantitative features among all accepted models is given in Figure 3.5C. The experimentally observed feature typically lies within the range of features observed in the corresponding models, with few exceptions. For instance, while the IMs for the CA3 Giant neuron type exhibited a range of *sfa* slopes that encompassed the experimentally observed *sfa* slope (Figure 3.5C bottom), its *fsl* lies outside the model range (Figure 3.5C top). These models were nonetheless accepted because they all satisfy the criteria for the target class (ASP.).

The best model for CA3 Basket (ASP.SLN) showed the highest error in the *sfa* slope among all the adapting classes (Figure 3.5C bottom). Yet, the accepted models for this neuron type not only exhibited the desired class (Figure 3.3, ASP.SLN), but also captured fast-spiking behavior, which plays an important role in network synchronization (Traub et al., 1996; Cardin et al., 2009). It should be emphasized that there is no guarantee that a model fit to a single experimentally recorded fast-spiking trace is indeed a fast-spiking model. For example, if the model of a CA3 Basket fast-spiking neuron type was created by simply fitting to the only available trace (Figure 3.3, ASP.SLN), it might still exhibit non-fast spiking behavior for a lower current input. To avoid this

discrepancy, in fast-spiking models we enforced a minimum instantaneous frequency of 25 *Hz* for a step current close to the rheobase (Figure 3.6). In the end, a neuron type is represented by a set of heterogeneous models with similar behavioral features.
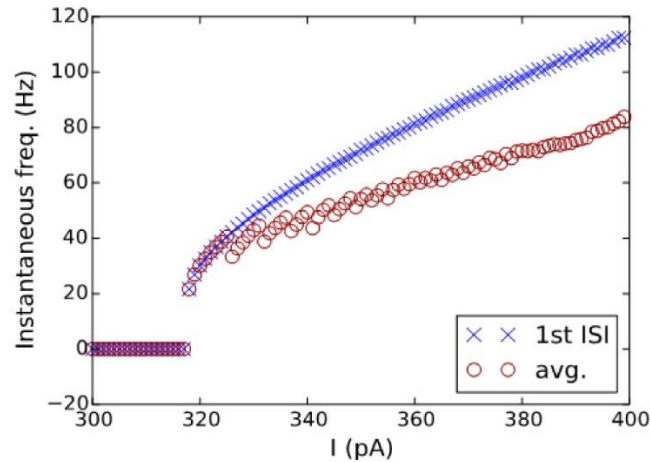
Figure 3.6: I-F characteristics of the fast-spiking model of a CA3 Basket neuron.
Instantaneous frequencies, calculated as the inverse of ISI average (circles) and of the first ISI (crosses), are plotted against the input currents for the model in Figure 3.3(2A). A minimum frequency of 25 Hz was enforced as a constraint, where the best model found by the EA exhibits a minimum frequency of 21 Hz.

3.3. Constrained multi-compartment models

In addition to the simple point-neuron models described in previous sections, we create MC Izhikevich models with heterogeneous compartments for all neuron types with dendrites spanning multiple hippocampal layers. These models capture the differences in the active and passive properties between soma and dendrites as well as coupling mechanisms that allow biologically realistic signal transmission between compartments. However, our MC models do not have branching dendritic arbors, and only consists of up to four compartments. This is because each additional compartment adds ten new

57

parameters for optimization, and tuning hundreds of compartments for each neuron type

is an unrealistic goal. We assume that layer-level segregation of synaptic inputs is

sufficient to significantly increase the computational power of the models in a network.

As an illustration, we present a four compartment model of CA2 pyramidal

neuron type (Figure 3.7). The somatic compartment (SP) reproduced features of

experimentally recorded voltage trace (see Figure 3.3 – 2B) both qualitatively and

quantitatively (Figure 3.7A). Furthermore, we enforced four additional constraints for

MC models as detailed in section 2.3.2. Decoupled dendritic compartments are less

excitable than the somatic compartment (Figure 3.7B) and have higher input resistances

(Figure 3.7C). It should be noted that the dendritic input resistances and excitabilities

were only enforced qualitatively (the quality of being higher or lower) relative to the

somatic compartment. Neither the absolute values nor the magnitudes of the differences

were enforced in the error function (see equations 6 & 7 in section 2.3.2).

In addition, the dendritic compartments allow forward propagation of spikes to

the adjacent compartments. A few hundred excitatory synapses were simultaneously

stimulated in order to initiate a spike at a dendritic compartment, and forward spike

propagation (in the direction towards soma) was verified at the adjacent compartment

(Figure 3.7D). Interestingly, the SLM compartment required an additional depolarizing

current of $1200pA$ in order to initiate a spike, consistent with experimental observations

(Jarsky et al., 2005). Although we enforced a spike propagation rate of 1 for isolated

spikes initiated at a dendritic compartment (see Section 2.3.2), we noticed that the rate

was less than 1 for high frequency dendritic spike trains. Finally, the amplitude of unitary

EPSP measured at the somatic compartment was constrained to be in the biologically

realistic range of (0.1, 0.9) mV (Figure 3.7E).
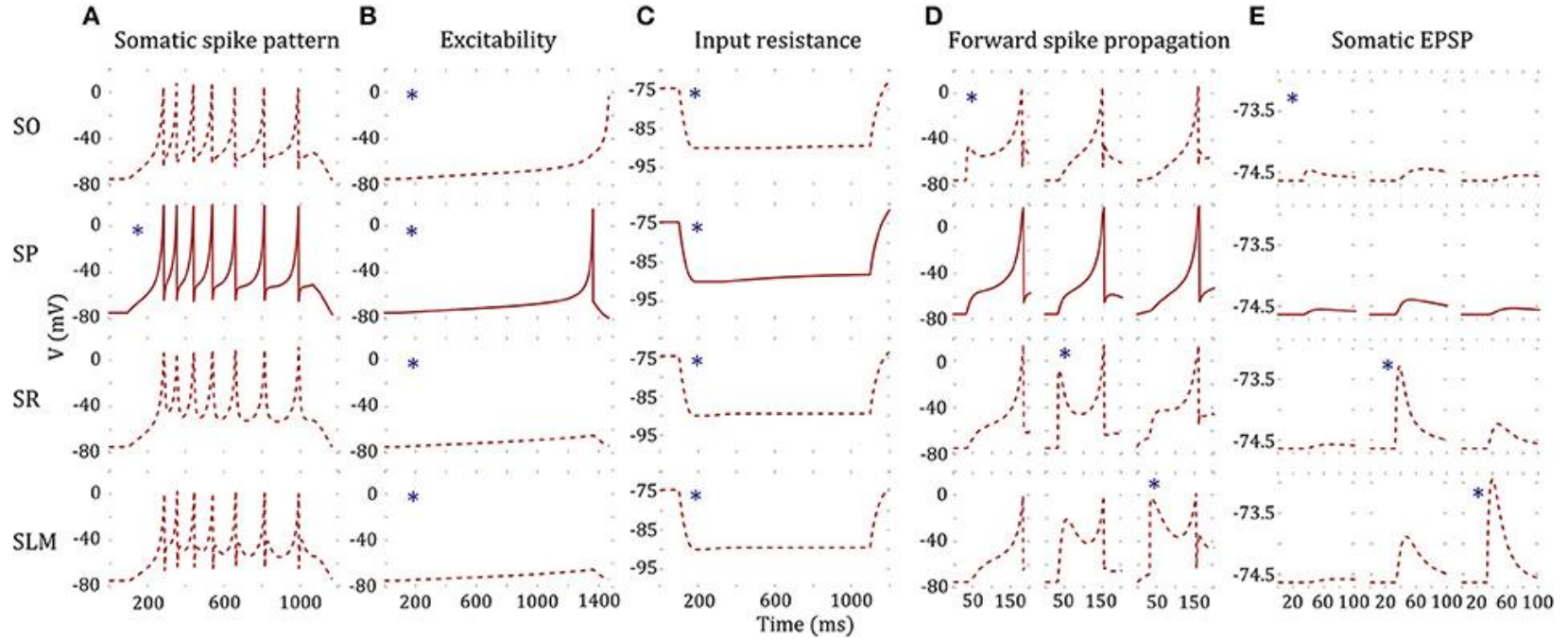
Figure 3.7: A four-compartment model of a CA2 Pyramidal neuron.
*indicates stimulated compartment (using input current/excitatory synapses) (A) Somatic compartment reproduces spike pattern of class D.ASP. for I = 401 pA with *fsl:* 188 ms, *sfa*: *y = 0.173x + 1.017* [compare with experimental trace in Figure 3(2B) and features in Figure 5C]. (B) Decoupled dendritic compartments (DC) are less excitable than the somatic compartment (SC). SC spikes before DC's for ramp current (ramp slope: 0.1 pA/1 ms). (C) Decoupled DC's have higher input resistance (IR) than the SC. IR is measured by the steady state voltage deflection due to a hyperpolarizing current application (−500 *pA*). The amplitudes of voltage deflections are 14.92, 13.66, 14.83, and 14.87 mV for SO, SP, SR, and SLM, respectively. (D) The model and coupling parameters were optimized to enable forward propagation of spikes to the adjacent compartment. A total of 200 excitatory synapses were stimulated at 40 ms to initiate a spike at a DC. The SLM compartment required an additional input current of 1,200 pA to elicit a spike. Only the forward spike propagation was enforced. (E) The model was constrained to evoke a unitary EPSP with amplitude in the range (0.1, 0.9) mV. Excitatory synapses were stimulated at SO, SR, and SLM, and the amplitude of the EPSP was measured at SP. EPSP amplitudes at SP were 0.09, 0.24, and 0.1 mV by stimulating a single synapse at SO, SR, and SLM, respectively.

60

Table 3.3: IM parameters of the 4-compartment model from Figure 3.7

Compartment	k	a	b	d	C	Vr	Vt	Vpeak	Vmin	G	P
SO	0.875	0.004	9.154	41	1163	-74.633	-61.327	7.440	-66.761	170	0.407
SP	1.029	0.002	11.054	40	1164	-74.633	-62.009	18.314	-65.184	-	-
SR	0.840	0.016	10.912	42	1174	-74.633	-62.307	14.142	-63.394	169	0.169
SLM	0.833	0.019	9.471	42	1170	-74.633	-60.468	2.444	-66.223	169	0.348

Even though not directly enforced in the error function, our MC models qualitatively exhibited the known directional voltage attenuation properties of hippocampal neurons: voltage attenuation from a dendritic location to the soma is much higher than in the opposite direction (Mainen et al., 1996; Carnevale et al., 1997; Chitwood et al., 1999; Golding et al., 2005). This behavior was observed in the models because of the higher input resistances of the dendritic compartments and the asymmetric coupling between the compartments. The EA always selected weaker coupling towards the soma than away from it. Optimization of a 4-compartment model required ~20 hours of total execution time on the GPU. This is roughly a 15X speedup from CPU execution. The 39 parameters of the model from Figure 3.7 are given in Table 3.3.

3.4. Variabilities in the intrinsic properties *within* a neuron type

Our models of hippocampal neuron types were constrained using voltage traces digitized from figures in the published literature. It is thus natural to ask: how faithfully does a representative recording from a single neuron, which the authors chose to include in an article, reveal the real intrinsic property of that neuron type? Under the same experimental conditions, a different neuron of the same type might behave slightly differently due to experimental noise and biological variability. A truly accurate model of a neuron type should take into account (and even represent) such intra-neuron type behavioral variabilities. For instance, if the experimental data consist of spike pattern traces recorded from several neurons of the same type under the same experimental conditions, the error function could use statistical measures such as z-score to capture the variability in the models (Druckmann et al., 2007; Markram et al., 2015). However, we

ultimately strive to create spiking models for over a hundred hippocampal neuron types based on the available experimental data as gleaned in Hippocampome.org. Except for a few well-studied neuron types such as CA1 pyramidal neurons, DG granule neurons, and a handful of GABAergic interneurons, the vast majority of neuron types identified in the hippocampal formation to date lack adequate data to represent their behavioral variabilities. While such a paucity of empirical evidence might pose the risk of overfitting the model to experimental noise, two key aspects of our approach synergistically reduce that risk: (i) inclusion of qualitative class criteria in the error function and (ii) parameter space exploration using the EA.

Firstly, we dynamically weigh the feature errors during the EA search with weights determined by comparing the model's spike pattern class to the experimental target (see Methods). This ensures that several near-optimal points in the error landscape represent the appropriate class, even though the exact feature errors might be higher than the globally optimal point (Figure 3.8A). Without such a weight-assignment scheme, a near-optimal point might not necessarily represent the target class, because both the feature that defines a boundary between classes (e.g. *fsl* between ASP. and D.ASP.) and the feature that does not (e.g. *pss* between ASP. and D.ASP.) would equally contribute to the error. Thus, explicitly integrating qualitative definitions in the error function sharply distinguishes the near-optimal points that satisfy class criteria from the ones that do not (Figure 3.8B). This increases the EA's chances of finding the models that reproduce the target class.
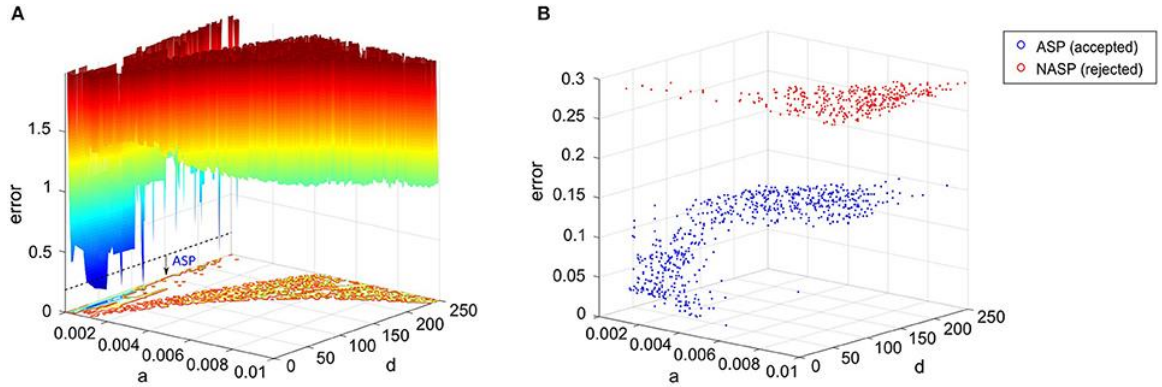
Figure 3.8: Parameter space exploration by the EA in a landscape that integrates qualitative class definitions.
(A) Error landscape created by the features of a CA3 Giant neuron that exhibits a spike pattern of class "ASP." [see Figure 3(1C)]. The dotted line denotes the threshold for model acceptance. All models below this line exhibit quantitative features *similar* to the experimental ones, while strictly adhering to the definitions of the target class (ASP.). This threshold might not necessarily be the same for a different spike pattern of class ASP., since the class definitions were weight factors for the quantitative feature errors rather than separate objectives themselves. The rest of the IM parameters were kept constant to plot this landscape. (B) The best models found by the EA across 1,000 stochastic trials for the same neuron type. A total of 651 accepted models satisfied the criteria for ASP., while all rejected models exhibited NASP. These two classes show clear separation in the search space, which is due to the scaling of class-specific feature errors. The EA identified several best models, which are not present in (A), demonstrating exploration capabilities in a multi-dimensional search space. Notice the difference in the "error" axis scale between the two plots.

Secondly, rather than just exploiting the search space to identify a single optimal point that precisely reproduces the spike times, our approach explores the search space and identifies numerous points that elicit a similar behavior. The similarity is governed by the qualitative class definitions, which are inherent to the error landscape as described before. The EA exploration was boosted by a high-rate reset mutation along with a two-point crossover. The downside of such a configuration is the reduced EA reliability in finding acceptable models in certain cases. For instance, only 651 out of 1000 trials found best models that satisfy the target class criteria (ASP.) for the CA3 Giant neuron type (Figure 3.8B). It is possible to increase this EA reliability by using a step mutation with a lower rate; however, this will be achieved at the cost of global exploration, ultimately resulting in reduced heterogeneity in the accepted models. In the end, a subset of all best

models exhibiting quantitative features with a certain degree of variability is chosen to represent a neuron type (section 3.2). Those features strictly adhere to the criteria for the qualitative class of the spike pattern recorded from that neuron type.

There is no guarantee to avoid over-fitting the best model from a single EA trial to the experimental noise. However, by reducing the acceleration of evolution within the bounds of target class (dynamic feature weight assignment), and identifying several near-optimal points within these bounds (parameter space exploration), we reduce the risk of the best models from all EA trials converging to a single globally optimal point, which might or might not represent a noisy feature. It is worth remembering that a feature threshold of a spike pattern class was statistically inferred from the distribution of that feature from all neuron types (Komendantov et al., 2017).

The accepted models for a single behavior showed notable variation in their parameters, except for TSTUT.NASP (Figure 9A). Such a variation was most prominent for parameters *'a', 'b'* and *'d'*, but only the dimensions *'a'* and *'b'* are shown in Figure 3.9A for the nine single-behavior types. Thus, a wide range of parameters yielded similar behaviors, demonstrating the robustness of our EA in exploring the parameter space. This is also consistent with the notion that a given neuron behavior may result from multiple distinct combinations of ion-channel conductance densities (Marder and Prinz, 2002).
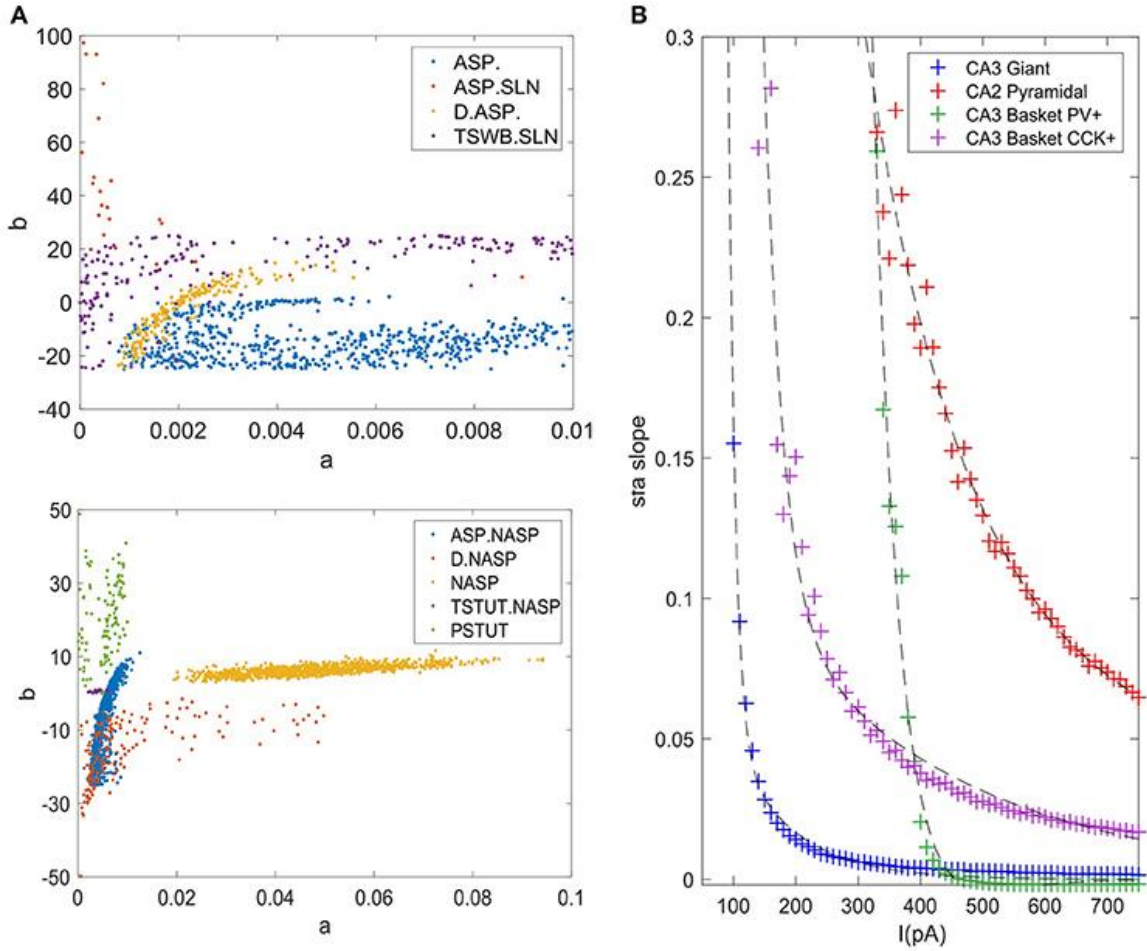
Figure 3.9: Model and feature variabilities across neuron types.
(A) Accepted models from each of the nine single behavior types are plotted on dimensions "*a*" and "*b*" of the IM. Best models from all 1000 EA trials were accepted for NASP (bottom), whereas only 25 models were accepted for ASP.SLN with fast spiking constraint (top). All behaviors that include "ASP." are restricted to the region $a < 0.01$. Stuttering (PSTUT) and fast spiking (ASP.SLN) behaviors are restricted to the region $b > 0$ (top). Notice the difference in axes ranges between top and bottom plots. (B) The slope of *sfa* is plotted as a function of input current (lasting 500 ms) for the best IMs of four neuron types that included "ASP." in their behavior. The *sfa* slope decreases exponentially with linearly increasing input step current. These models show substantial variation in their input dependencies of *sfa* slopes.

3.5. Diversity in the intrinsic properties *across* neuron types

In section 3.4, we discussed within-neuron type variabilities, where several IMs

for a single neuron type reveal slightly different quantitative features for similar input

currents. In addition to this, feature diversities across different neuron types, both

qualitative and quantitative, also likely play a major role in the emergent properties in a network.

Even different neuron types that exhibit similar qualitative behavior might reveal substantial diversity in their quantitative features. For instance, the neuron types that include transient ASP. in their behavior are CA3 Giant (ASP.), CA3 Basket CCK (ASP.NASP), CA3 Basket (ASP.SLN) and CA2 Pyramidal (D.ASP.). The magnitudes of *sfa* experimentally observed from these neuron types were ~0.1 for 100*pA*, ~0.06 for 400*pA,* ~0.02 for 400*pA* and ~0.2 for 400*pA*, respectively (Figure 3.5C). The IMs constrained using these features reveal considerable diversity in the magnitudes of *sfa* among these four models when the input current is gradually increased, as evidenced by plotting *sfa* against a range of input currents '*I*' (Figure 3.9B). For all cases, *sfa* decreased exponentially with linear increases of '*I*'. However, these models showed notable differences in their excitabilities and their *sfa* ranges. Most of the variance in *sfa* slopes for the fast spiking CA3 Basket PV+ model could be explained by a narrow range of inputs (325*pA* – 425*pA*). This window is much larger for the regular spiking CA2 pyramidal model. Figure 3.9B illustrates the diversity of input-dependent *sfa* ranges among these four models. Although experimental data are too sparse to validate such ranges of *sfa*s in the models, the above results demonstrate that our approach can create models with remarkable quantitative diversities, even with limited amounts of data.

The diverse single behavior classes were most separated along the dimensions *'a'* and *'b'* of the parameter space (Figure 3.9A). The four behaviors that include ASP. were restricted to very small values of *'a'* (<0.01), whereas the NASP models converged to a

broad range (0.02, 0.1). As mentioned in section 2.1, *'a'* is the time constant for recovery variable *'U'*, and lower values for *'a'* results in stronger *sfa*. The region *'b' > 'a'* correspond to Andronov-Hopf bifurcation (Izhikevich, 2003) and all the fast-spiking ASP.SLN models were identified in the range (9, 90) for *'b'*. Although only 25 best models from 1000 EA trials satisfied the criteria for ASP.SLN and fast-spiking, these models encompassed a broad range for *'b'* (Figure 3.9A – top).

The optimal region for each class is shown in Figure 3.10. There is a significant overlap between the regions for the classes ASP. and ASP.NASP (see also Figure 3.9A). This is because the difference between these two classes often depends on the input conditions rather than the nine parameters of the model. It is worth mentioning again that in the ASP. class only the transient element is present in the spike pattern. Given a longer duration of input, this pattern will most likely show a steady-state of NASP. The classes NASP and D.NASP encompassed larger regions in the parameter space (Figure 3.9A and Figure 3.10). In the case of D.NASP, this is likely due to the fact that the experimentally injected input current was unknown (see Table A1), and the EA identified several possibilities for similar behavior under a broad range of input currents.
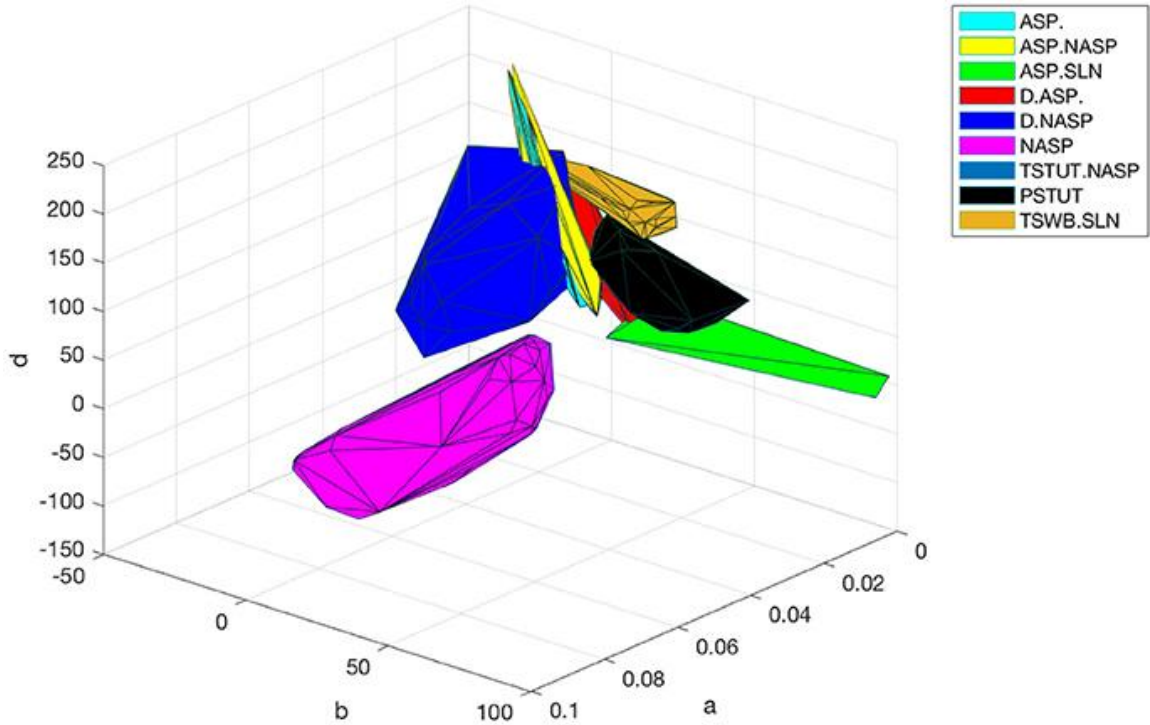
Figure 3.10: Optimal regions of different spike pattern classes.
Region for a class was obtained by plotting the convex hull from all the accepted models. The relationship between parameters "*a*" and "*b*" determines the type of bifurcation and it separates several classes. There is significant overlap between the classes ASP. and ASP.NASP. In general, the EA identified a wide range of optimal points for each class along the dimensions "*a*," "*b*," and "*d*". The classes NASP and D.NASP encompassed larger regions than other classes. The region for TSTUT.NASP, which lies very close to PSTUT (see Figure 3.9A–bottom) is the smallest region and is not visible here.

4. Discussion

A major motivation behind the current work is the intent to create large-scale network models using IMs with both biologically realistic within-neuron type behavioral variabilities and experimentally validated between-neuron type diversity. Our compact model representations of diverse neuron behaviors allow the implementation of hippocampal circuit simulations in a computationally efficient manner. More importantly, our results offer a sampling range for a neuron group in a network model (Figure 3.9A and Figure 3.10). Several studies have shown that neurons have intrinsic plasticity and

undergo homeostatic regulatory mechanisms, which modify their non-synaptic ion-channels such as sodium and delayed-rectifier potassium channels, in order to maintain a certain target activity level in the network (Desai et al., 1999; Aizenman and Linden, 2000; Desai, 2003). This implies similar intrinsic properties or behaviors can arise from various combinations of ion channel conductance densities (Foster and Ungar, 1993; Marder and Goaillard, 2006; Schulz et al., 2006). In the mathematically abstracted IM, this is equivalent to various combinations of parameter interactions. Although it might be difficult to describe such interactions mathematically, a robust EA can identify several optimal points in the multi-dimensional search space that correspond to the known behaviors of a neuron type (Figure 3.8B). Thus, our method represents a neuron type as possibilities in the model parameter space (Figure 3.9A). Such a representation is crucial for a thorough and systematic investigation of the contributions of neuronal intrinsic properties to network behavior and function. Our multi-compartment models extend this platform to investigate the effects of dendritic filtering on the emergent network properties, while still being reasonably compact.

Furthermore, the diversity captured in our models may help experimentalists identify and distinguish real neurons in finer electrophysiological terms. Our models of *sfa* suggest the existence of different critical input windows for different neuron types as explained in section 3.5 (Figure 3.9B). Thus, a neuron exhibiting *sfa* could be characterized by the range of *sfa* slopes and its critical input window. The *sfa* makes a neuron act as high-pass filter (Benda and Herz, 2003) and plays a role in emergent network synchronization (Ermentrout et al., 2001). Two neurons with different input-

dependent *sfa* ranges will likely have different filtering properties, and consequently, may contribute to network synchronization in different ways.

An advantage of using a Pareto-optimal front approach for model optimization (Druckmann et al., 2007) is that it avoids the need to weigh different feature errors. However, the performance of such multi-objective optimization techniques is affected by the number of objectives (Khare et al., 2003) and exponentially increasing population sizes are required to represent high-dimensional Pareto-optimal fronts (Deb, 2014). A single interrupted spike pattern trace (e.g. TSTUT.NASP in Figure 3.3) presents at least eight objectives for optimization (see Table A2, CA1 O-LMR). Moreover, some of our simple models are constrained using several spike pattern traces (Figure 3.5A). With population sizes as small as 120, our approach can efficiently optimize model parameters for several objectives.

On the other hand, the approach created by Rössert et al. (2016) requires a data-driven microcircuit model constructed from morphologically detailed neuron models (such as the one in Markram et al., 2015) as a reference, and such reference models are computationally very expensive. Compared to this approach, our simple models might be less constrained in some cases, but they significantly reduce the open parameter space size to create biologically accurate circuit models. Furthermore, our simplified multi-compartment models intrinsically capture the dendritic voltage attenuation properties without a need for synaptic correction (Section 3.3).

The precise shape of the spike was not captured in some of our models (for example, D.NASP in Figure 3.3). This could be attributed to the quadratic voltage

dependence in the IM voltage equation. The AdEx model (Brette and Gerstner, 2005) , which replaces the quadratic term in the IM with an exponential term for the voltage dependence, has been shown to reproduce more realistic spike shapes (Badel et al., 2008). However, our selection criteria for the models were entirely based on the temporal features of the overall spike pattern, and do not include characteristics of individual spikes. More important for the information processing in a neural network are the excitability of neurons, the precise timing of spikes, and the properties of connections. The shape of the spike is unlikely to play an equally prominent role in network dynamics. In fact, in the nine-parameter IM formalism 'k' and 'Vt' collectively determine the shape of the spike. It is thus possible to obtain realistic spike shape by restricting the ranges for these parameters (e.g. Figure 3.3, ASP.SLN). However, we did not explore these parameter ranges and interactions for all the cases for the reasons mentioned above.

Although only IMs have been presented in this article, our framework can be easily enhanced to include any phenomenologically rich model of spiking behavior. The only part of this framework that is specific to the IM is the EA configuration presented in section 2.3.1. This configuration was identified partly based on the topographical features of error landscape created by the IM parameters. Once an appropriate EA configuration is identified, our error function and spike pattern classification procedures are readily applicable to any alternative model.

In the future, we will enhance our framework to model multi-behavior neuron types. At least fifteen morphological neuron types in the Hippocampome.org exhibit sharply distinguishable qualitative features under different experimental conditions. One

of the commonly occurring multi-behavior types in the hippocampus is stuttering and spiking observed in a single neuron for different current stimulation strengths. For example, a CA1 Bistratified neuron exhibited stuttering and regular spiking behaviors for 400 pA and 600 pA, respectively (Pawelzik and Hughes, 2002). Similarly, a CA1 Neurogliaform projecting neuron exhibited this multi-behavior for 500 pA and 700 pA (Price et al., 2005). Our preliminary work with multi-behavior types revealed vast possibilities for modeling such behaviors using IM, which could also provide insights into the existence of electrophysiological subtypes for a given morphological type.

The categorization of neuron type behaviors as either single-behavior or multi-behavior is solely based on the currently available experimental data. Consequently, it is possible that additional qualitative behaviors will be observed in future experiments from neuron type currently considered to display a single-behavior based on available data. An advantage of our modeling approach is that it identifies many possibilities for the known behaviors of a neuron type in the IM parameter space. Furthermore, the flexibility of our framework allows easier addition of newly observed behaviors from a neuron type to improve the accuracy of its model representations. Eventually, we plan to create models for over a hundred hippocampal neuron types and to make them freely available at Hippocampome.org. Nevertheless, although the modeling framework and the results presented in this article pertain to the hippocampus, our approach could be easily adapted to other brain regions.

CHAPTER 4: SIMPLE MODELS OF QUANTITATIVE FIRING PHENOTYPES IN HIPPOCAMPAL NEURONS: COMPREHENSIVE COVERAGE OF INTRINSIC DIVERSITY[⊥]

Patterns of periodic voltage spikes elicited by a neuron help define its dynamical identity. Experimentally recorded spike trains from various neurons show qualitatively distinguishable features such as delayed spiking, spiking with or without frequency adaptation, and intrinsic bursting. Moreover, the input-dependent responses of a neuron not only show different quantitative features, such as higher spike frequency for a stronger input current injection, but can also exhibit qualitatively different responses, such as spiking and bursting under different input conditions, thus forming a complex phenotype of responses. In previous work, the comprehensive knowledge base of hippocampal neuron types *Hippocampome.org* systematically characterized various spike pattern phenotypes experimentally identified from 120 neuron types/subtypes. In this paper, we present a complete set of simple phenomenological models that quantitatively reproduce the diverse and complex phenotypes of hippocampal neurons. In addition to point-neuron models, we created compact multi-compartment models with up to four compartments, which will allow spatial segregation of synaptic integration in network simulations. Electrotonic compartmentalization observed in our compact multi-

Authors: Venkadesh S, Komendantov AO, Wheeler DW, Hamilton DJ, Ascoli GA

compartment models is qualitatively consistent with experimental observations. The models were created using an automated pipeline based on evolutionary algorithms. This work maps 120 neuron types/subtypes in the rodent hippocampus to a low-dimensional model space and adds another dimension to the knowledge accumulated in *Hippocampome.org*. Computationally efficient representations of intrinsic dynamics, along with other pieces of knowledge available in *Hippocampome.org*, provide a biologically realistic platform to explore the large-scale interactions of various neuron types at the mesoscopic level.

<div align="center">

1. Introduction

</div>

Complex interactions among a myriad of neurons make it challenging to study the functions of brain regions. Although each neuron is different, their landmark features such as the dendritic structure and patterns of somatic voltage spikes help define types of neurons, and such grouping allows for a tractable description and investigation of complex network interactions. For instance, large-scale network models of brain regions can include precisely defined neuronal types to create a biologically realistic platform for hypothesis testing. While neurons differ in their morphological, biochemical and electrophysiological features, precisely what features are useful and relevant for neuronal grouping is a topic of great interest (Petilla Interneuron Nomenclature Group et al., 2008).

A few studies have created large-scale network models of brain regions (Eliasmith et al., 2012; Hendrickson et al., 2016; Izhikevich and Edelman, 2008; Markram et al., 2015). The major methodological difference among these studies is the

level of biological details captured in the individual components of the network and there is often a tradeoff between such biological details and the scale of the network. For example, a microcircuit model of the rat somatosensory cortex (Markram et al., 2015) simulated ~31,000 neurons with ~37 million synapses, where each neuron was a biophysically detailed description of one of 207 morpho-electrical types identified experimentally. On the other hand, a large-scale description of thalamocortical systems (Izhikevich and Edelman, 2008), which used simplified phenomenological neuron models (Izhikevich, 2003), simulated a network of a much larger scale (one million neurons and half a billion synapses), but it only included 22 abstract types among the neurons. Network modeling efforts more specific to the hippocampus include a full-scale model of the CA1 circuit (Bezaire et al., 2016) (~338,000 biophysically detailed neuron models of nine types), a large-scale model of the dentate gyrus (Morgan and Soltesz, 2008) (~52,000 biophysically detailed neuron models of four types) and a large-scale model of CA1 (Ferguson et al., 2017) (~10,000 phenomenological models of two types).

An advantage of biophysically detailed neuron models is that they can include experimentally known distributions of ion channels during model generation. For example, A-type potassium and hyperpolarization-activated currents were distributed non-uniformly (increasing densities with distance from soma) in the CA1 pyramidal models in (Bezaire et al., 2016; Migliore et al., 2018) based on experimental observations. However, hundreds of compartments, each specifying the dynamics of several types of currents require prohibitively large supercomputer resources, if one wants to simulate a large-scale network of biophysically detailed neuron models (Bezaire

et al., 2016; Markram et al., 2015). Increasing the complexity of the model also increases the number of free parameters that cannot be measured experimentally and need to be estimated. On the other hand, highly abstract phenomenological models such as (Izhikevich, 2003) specify only two equations, and they significantly reduce the computational cost of simulating large-scale networks (Beyeler et al., 2015; Ferguson et al., 2017; Izhikevich and Edelman, 2008). However, the parameters that govern such models are not directly biologically interpretable and optimizing their parameters to reproduce quantitatively accurate intrinsic dynamics of neuron types can be difficult (Rossant et al., 2010; Venkadesh et al., 2018). In current work, with a vision of creating a real-scale network model of the rodent hippocampus that nevertheless captures biological details at the mesoscopic level, we have created phenomenological models of 120 hippocampal neuron types and subtypes using their intrinsic dynamics identified experimentally. Recently, a database of simple models for hundreds of neurons of various transgenic types in the mouse primary visual cortex was created with a similar vision (Teeter et al., 2018).

A large-scale literature mining effort created Hippocampome.org (Wheeler et al., 2015), a comprehensive knowledgebase of neuron types in the rodent hippocampal formation (dentate gyrus, CA3, CA2, CA1, subiculum, and entorhinal cortex). This resource provides information on morphology, electrophysiology, and molecular marker profiles of more than 100 neuron types, where the type of a neuron is primarily determined based on the locations of its axon, dendrites and soma across 26 parcels of the hippocampus. A numerical protocol (Komendantov et al., 2018) was developed to

identify the classes of published somatic spike patterns of morphologically identified neuron types. Analysis of a total of 247 traces, which were linked to 90 morphological types, revealed several spike pattern phenotypes, and further divided 22 morphological types into 52 electrophysiological subtypes for a total of 120 neuron types/subtypes. The subtypes of a neuron type, while sharing the same morphological identity, differ in their spike pattern phenotypes. Features of experimentally recorded spike patterns were extracted for a neuron type and a systematic characterization of spike pattern features revealed nine unique families of intrinsic dynamics, such as delayed spiking, non-adapting spiking, simple adapting spiking, and persistent stuttering among hippocampal neurons. Furthermore, many neuron types exhibit different classes of spike patterns for different input currents, resulting in complex spike pattern phenotypes.

In this article, we present a comprehensive set of point neuron models that quantitatively reproduce various spike pattern phenotypes of hippocampal neurons. We also created multi-compartment models that are compact extensions of point neurons in order to allow spatial context for synaptic integration in a network. In addition, our compact multi-compartment (compact-MC) models exhibit electrotonic properties consistent with experimental observations. We also report novel insights into the relationships between abstract model parameters and various biological properties, which were revealed in our correlation analysis. The models were created using an automated modeling framework (Venkadesh et al., 2018), and they further enhance the existing accumulated knowledge in *Hippocampome.org*, where they are freely available to download. By identifying several possibilities for a quantitative phenotype in

phenomenological space, current work comprehensively maps hippocampal neuron types to low-dimensional model subspaces, which can be used as sampling regions for biologically realistic large-scale network simulations of hippocampal circuits.

2. Methods

The class of a spike pattern is identified based on various transient and/or steady-state elements present in the pattern. Transient elements are Delay (D), if the first spike latency (*fsl*) is sufficiently long; Adapting Spiking (ASP), if the inter-spike intervals (*ISIs*) increase over time showing a spike frequency adaptation (*sfa*); Rapidly Adapting Spiking (RASP), if a strong *sfa* is only present in the first two or three ISIs, Transient Stuttering (TSTUT), if a quiescent period follows a cluster of high frequency spikes; and Transient Slow-Wave Bursting (TSWB), if a slow after-hyperpolarizing potential follows a cluster of high frequency spikes. Steady-state elements are Silence (SLN), if the post-spike silence (*pss*) (quiescence following the last spike) is sufficiently long; Non-Adapting Spiking (NASP), if no frequency adaptation is identified in a non-interrupted spiking; Persistent Stuttering (PSTUT), if at least one sufficiently long quiescent period separates two clusters of high frequency spikes; and Persistent Slow-Wave Bursting (PSWB) if a slow after-hyperpolarizing potential is present in an otherwise PSTUT pattern. Thus, the key features are *fsl*, *sfa*, *pss* and the number of ISIs (*nISIs*) for a spiking pattern, and burst widths (*bw*), post-burst intervals (*pbi*), number of bursts (*n_bursts*) and *nISIs* within a burst (*b-nISIs*) for a stuttering/bursting pattern.

A spike pattern can consist of one or more elements, and we use a dot ('.') notation to separate them. A '.' in a spike pattern indicates that the preceding element is a

79

transient (e.g. "ASP" is a transient element in the pattern "ASP.SLN"), and if the pattern

ends with a '.' (e.g. "ASP." or "RASP.ASP."), it serves to mean that this is an incomplete

pattern, where the duration of current injection was too short to elicit one of the steady

state responses. Supplementary text S1 and (Komendantov et al., 2018) provide more

details on the criteria for various spike pattern classes.

The temporal features described above identify the class of a single spike pattern,

and all classes of patterns exhibited by a neuron under different input currents

collectively define the spike pattern phenotype of that neuron. Thus, our approach

emphasizes the temporal patterns in the periodic voltage spikes rather than the shape of

the spike or subthreshold dynamics to define the intrinsic dynamics. Note that a minimum

of two spikes are required to identify a class, hence, single-spike traces are not assigned a

class label in this scheme. However, such single-spike traces are still included as

constraints to help capture the excitability (rheobase) in the models more precisely.

We used the Izhikevich model (IM) (Izhikevich, 2003, 2007) to reproduce spike

pattern phenotypes. This model is governed by the state variables membrane voltage (V)

and membrane recovery variable (U):

$$C \cdot \frac{dv}{dt} = k \cdot (V - V_r) \cdot (V - V_t) - U + I \tag{1}$$

$$\frac{dU}{dt} = a \cdot \{b \cdot (V - V_r) - U\} \tag{2}$$

$$if \; V = V_{peak} \; then \; V = V_{min}, U = U + d$$

where V_r and V_t are the resting and threshold voltages respectively; V_{peak} is the

spike cutoff value, V_{min} is the post-spike reset value for the voltage and C is the cell

capacitance. The parameters k, a, b and d affect the model's intrinsic dynamics both qualitatively (e.g. the type of bifurcation revealed by fast-spiking and non-fast-spiking behaviors) and quantitatively (e.g. rheobase and magnitude of *sfa*). Compact-MC models with up to four compartments were modeled using an asymmetric coupling mechanism for the interaction currents in proximal (I_{prox}) and distal (I_{dist}) compartments (e.g. soma and dendrite, respectively) as described in (Venkadesh et al., 2018):

$$I_{prox} = G \cdot P \cdot \left(V_{prox} - V_{dist}\right) \tag{3}$$

$$I_{dist} = G \cdot (1 - P) \cdot \left(V_{dist} - V_{prox}\right) \tag{4}$$

where G is the coupling strength and P denotes the degree of coupling asymmetry, which determines the influence of a compartment on the overall model dynamics (Pinsky and Rinzel, 1994). It should be noted that each compartment specifies its own set of parameters, except V_r for equations (1) and (2). As reported before (Venkadesh et al., 2018), most of our compact-MC models specify a much weaker coupling toward the soma than away from it, making the somatic compartment dominate the overall model intrinsic dynamics.

Our modeling framework uses evolutionary algorithms (EA) and employs a feature-based error function. By incorporating spike pattern features (*fsl*, *sfa* etc.) and qualitative class criteria (*delay factor*, *number of piecewise linear fit parameters of ISIs* etc.) in the error landscape (Komendantov et al., 2018), our approach enforces a fine level of granularity in the key quantitative features of various spike-pattern classes, as described in our previous work (Venkadesh et al., 2018). The error function was defined as:

$$error = \sum_{f \in S}\left(W_f \times log\ \left(1 + \left|exp_f - model_f\right|\right)\right) \qquad (5)$$

where S: $\{fsl, pss, sfa, nISIs\}$ for a spiking class, and

S: $\{fsl, pss, bw, pbi, n\_bursts, b\_nISIs\}$ for a bursting/stuttering class. W_f is the feature

weight and it was calculated for each feature by comparing the target class with the

model spike pattern class during the EA search. The dynamical scaling of errors for the

key features using this scheme helped adjust the balance between exploration and

exploitation as the population began to converge within the subregion of the target class

(Venkadesh et al., 2018). Using this scheme, we previously identified subregions for

single-behavior neuron types, which show the same class of spike patterns regardless of

the input current strength. However, as mentioned before, many neuron types exhibit

different classes of patterns under different input currents. We noticed for many such

complex phenotypes, the EA with randomly initialized population using broad parameter

ranges showed a bias towards a single class rather than reproducing all the classes of a

phenotype. To reduce this bias in our current work, the EA population was initialized

using the subregions of all desired spike pattern classes, which were identified (in

independent EA runs) for single-behavior types (Venkadesh et al., 2018). It should be

noted, however, that during the EA search, the parameters of the IM could vary beyond

these subregions (using an unbounded mutation operator). Furthermore, we used a higher

population size (240 as opposed to 120 as for single-behavior types). The operators of the

EA (mutation, crossover etc.) were configured by taking into account the features of error

landscape created by the IM parameters (Venkadesh and Ascoli, 2017). In order for a

model found by the EA to be accepted, the classes of its spike patterns must match those of experimental traces. There is, however, one exception: without additional dendritic dynamics, the IM failed to reproduce the RASP.ASP. class of patterns, which show a strong and rapid adaptation (in the first 2 or 3 ISIs) followed by a very weak yet sustained adaptation. Therefore, single-compartment models of seven neuron types, which experimentally showed this complex transient pattern, were accepted with RASP.NASP patterns instead (see results).

Compact-MC models were additionally constrained to exhibit appropriate relative excitabilities and input resistances between soma and dendrites, and sub- and supra-threshold signal propagation properties, as described in our previous work (Venkadesh et al., 2018). The following errors were calculated for each dendritic compartment:

$$error_{rheo} = \begin{cases} 0, I_{dend}^{rheo} \geq I_{soma}^{rheo} \\ \log\left(1 + \left(I_{soma}^{rheo} - I_{dend}^{rheo}\right)\right), I_{dend}^{rheo} < I_{soma}^{rheo} \end{cases} \tag{6}$$

$$error_{vdef} = \begin{cases} 0, V_{dend}^{def} \geq V_{soma}^{def} \\ \log\left(1 + \left(V_{soma}^{def} - V_{dend}^{def}\right)\right), V_{dend}^{def} < V_{soma}^{def} \end{cases} \tag{7}$$

$$error_{R} = \begin{cases} 0, R = 1 \\ \log\left(1 + (1 - R)\right), R < 1 \end{cases} \tag{8}$$

$$error_{epsp} = \begin{cases} 0, 0.1 \leq EPSP \leq 0.9 \\ \log\left(1 + (0.1 - EPSP)\right), EPSP < 0.1 \\ \log\left(1 + (EPSP - 0.9)\right), EPSP > 0.9 \end{cases} \tag{9}$$

where I^{rheo} is the minimum depolarizing current required to elicit a spike and V^{def} is the amplitude of steady-state voltage deflection from the resting voltage for a hyperpolarizing input current in decoupled compartments. R is the spike propagation rate,

defined as the ratio between the number of spikes observed at the destination

compartment and the number of spikes initiated at the source compartment. Several

AMPA synapses (50-200) were stimulated to initiate a spike at a dendritic compartment

and R was calculated for the adjacent compartment for forward-spike propagation.

Finally, a single AMPA synapse was stimulated at a dendritic compartment and the

amplitude of the excitatory post synaptic potential ($EPSP$) was measured at the somatic

compartment. A range of $(0.1, 0.9)$ mV was enforced for the $EPSP$ amplitude. All

synapses used a value of 10 for the weight, unless explicitly mentioned otherwise. For the

comparison against biophysically detailed models, we used the CA1 Pyramidal multi-

compartment model (Jarsky et al., 2005) obtained from ModelDB (McDougal et al.,

2017) (accession number: 116084), which was simulated using the NEURON simulation

environment (Hines and Carnevale, 1997), and the simulated data from (Krueppel et al.,

2011) for DG Granule neuron type. For the analysis of attenuation of back-propagating

spikes, the amplitude of a spike in the IM is measured as the difference between the

maximum of V and the reset V_{min}. In this article, the goodness-of-fit is reported as the

ratio between simulated and experimentally recorded values (for spike pattern features)

and the ratio between somatic- and dendritic-compartments (for excitability and input

resistance) for intuitive understanding. Optimization and simulation scripts are publicly

available at *https://github.com/Hippocampome-Org/Time.*

      Pairwise correlations were performed to explore the relationships between IM

parameters and various pieces of knowledge (PoK) that have been accumulated in

Hippocampome.org. All firing pattern classes and electrophysiological properties and the

20 most cited biomarkers were considered, which resulted in a total of 198 correlations. To analyze statistical co-occurrence with existing categorical knowledge, continuous IM parameters were converted into categorical variables appropriately by marking positive and negative or by labelling top- and bottom- one-third ranges respectively as high and low. Correlations between the categorical variables were evaluated using Barnard's exact test for 2x2 contingency tables. This test provides the greatest statistical power when row and column totals are free to vary (Lydersen et al., 2009). Threshold for statistical significance and false discovery rate for multiple comparisons were conventionally set to 0.05 and 0.25, respectively.

3. Results

3.1. Single-compartment models of diverse intrinsic spike pattern phenotypes

The intrinsic dynamics of a neuron is typically identified in experiments by injecting step input currents of various magnitudes. A neuron's responses to these inputs typically fall into one of two phenotype super-families: (1) a spiking phenotype, where the neuron only exhibits continuous spike pattern classes such as ASP.SLN, NASP, and D.NASP for different input currents (Fig 4.1A-D), and (2) a stuttering/bursting phenotype, where the neuron exhibits an interrupted spike pattern class such as TSWB.SLN, TSTUT.NASP, and PSTUT for at least one input current (Fig 4.2A-D). A spiking or stuttering phenotype could be formed by various combinations of spike pattern classes, and models for four exemplar cases in each of these two phenotype super-families are reported in this article (visit *Hippocampome.org* for a comprehensive list of phenotypes and their models).
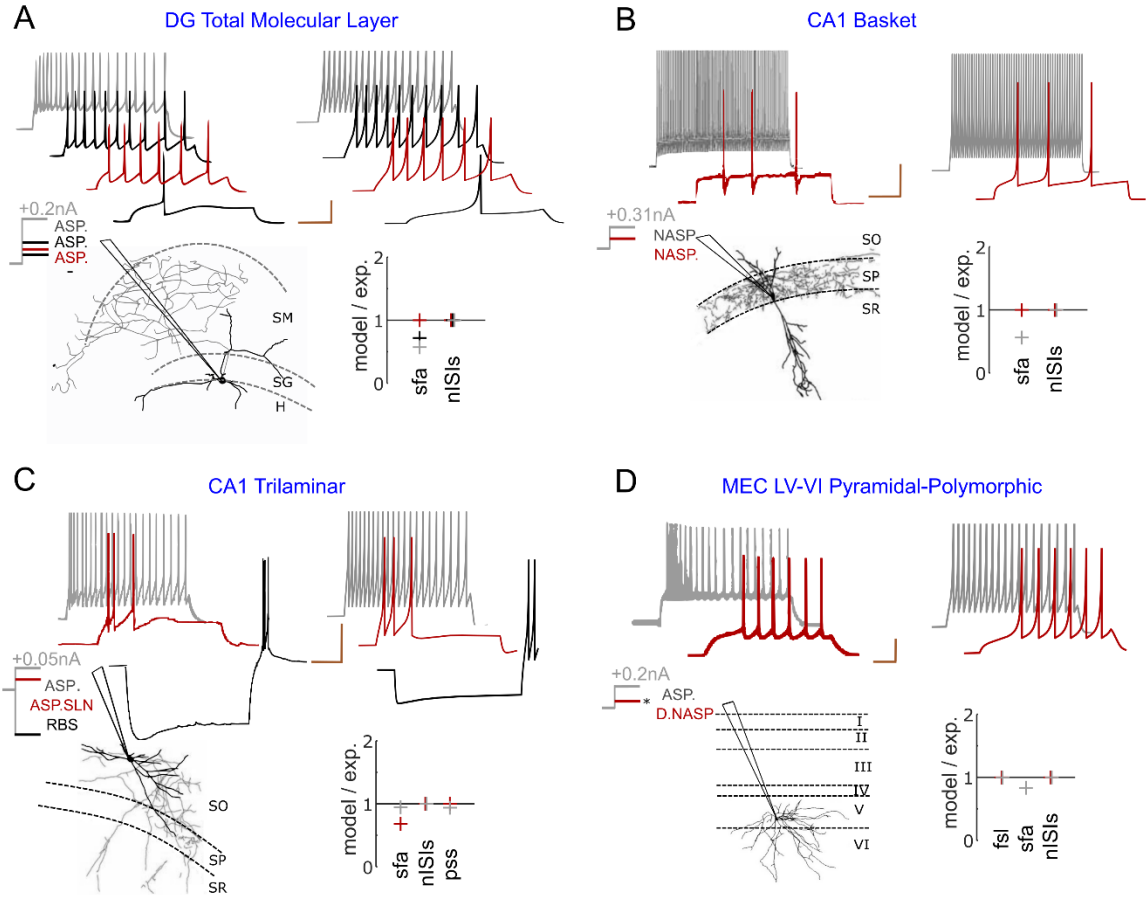
Figure 4.1: Exemplar models of continuous spiking phenotypes.
Each panel displays experimentally recorded voltage traces in the top-left and their morphological identity and magnitudes of somatic current injections in the bottom-left. Traces were digitized by *Hippocampome.org*. Morphological abbreviations: SO - stratum oriens, SP - stratum pyramidale, SR - stratum radiatum, SM - stratum moleculare, SG - stratum granulosum, H – hilus. Model responses for similar input currents ($\pm 0.01nA$ from experimental input) are given in the top-right and the goodness-of-fit is given (only) for key features in the bottom-right (supplementary table S2 reports goodness-of-fit for all features). The traces are highlighted in different colors to visually compare experimental and model responses, and to identify the input current and key features for each trace. Calibration bars denote $200ms$ and $20mV$ in all panels. (A) Simple phenotype of a dentate gyrus (DG) Total Molecular Layer neuron that elicits ASP. patterns under three different input currents (Mott et al., 1997). The digitally reconstructed morphology was reproduced from *NeuroMorpho.org* (Ascoli et al., 2007). (B) Simple phenotype of a CA1 Basket neuron that elicits patterns of class NASP for $+0.15nA$ and $+0.31nA$ (Tricoire et al., 2011). Note that *sfa* in the red trace is not statistically significant to qualify this pattern as ASP. (C) The phenotype of a CA1 Trilaminar neuron shows different classes of patterns for $+0.025nA$ and $+0.05nA$ (Tricoire et al., 2011). In addition, this neuron elicits rebound spikes (RBS) for a hyperpolarizing input of $-0.1nA$. (D) The phenotype of a medial-entorhinal cortex (MEC) neuron shows different classes of patterns for $+0.2nA$ and an unknown input (denoted by '*') just above its rheobase (Canto and Witter, 2012). All experimental traces are whole-cell patch clamp recordings.
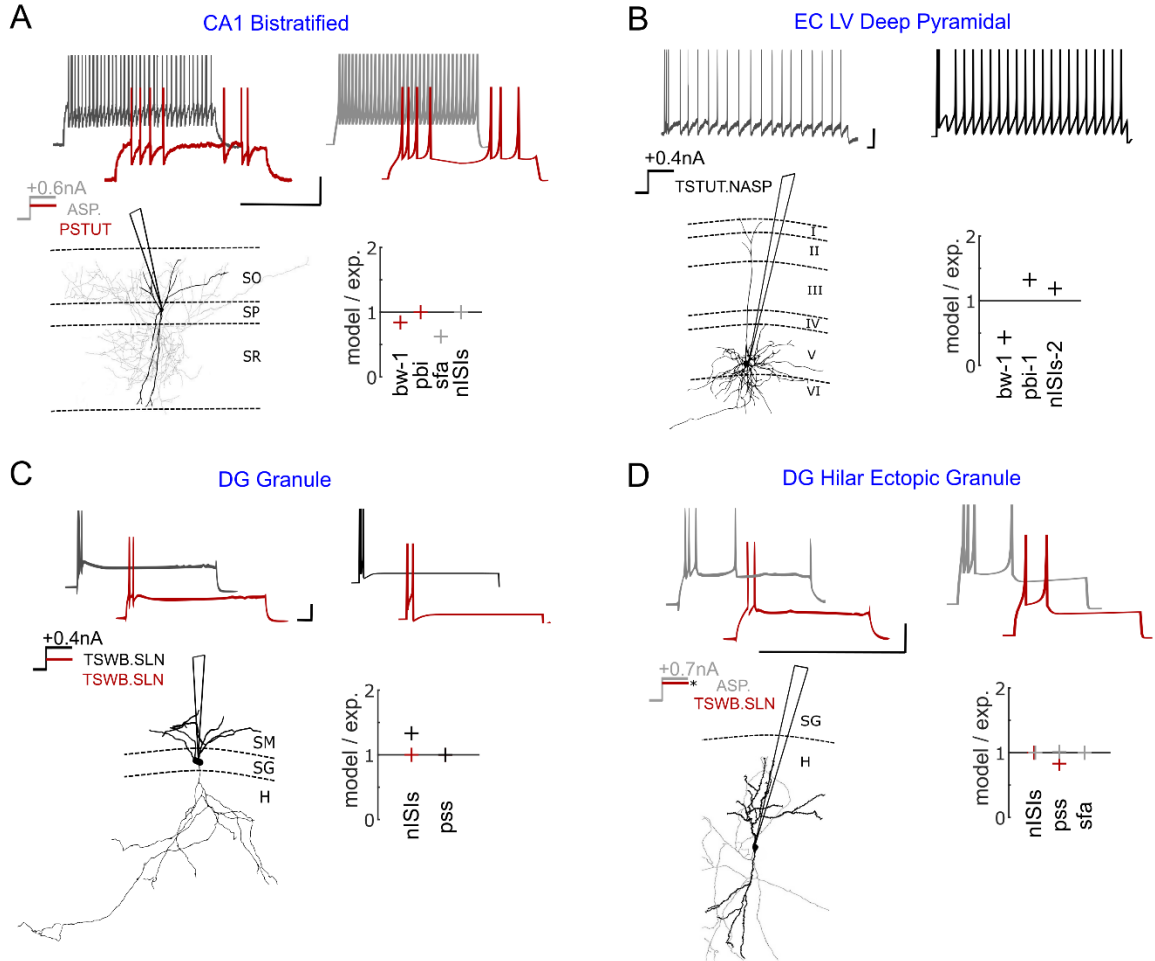
Figure 4.2: Exemplar models of stuttering/bursting phenotypes.
(A) Complex phenotype of a Bistratified neuron in CA1. This neuron elicits a stuttering pattern for +0.4*nA* (red) and a spiking pattern for +0.6*nA* (grey) (Pawelzik et al., 2002). The digitally reconstructed morphology (Katona et al., 2014) was reproduced from *NeuroMorpho.org* (Ascoli et al., 2007). (B) The voltage trace recorded from an entorhinal layer-5 neuron shows both (transient) bursting and (steady state) spiking features for +0.4*nA* (Hamam et al., 2002). (C) A DG granule neuron transiently bursts for both +0.2*nA* and +0.4*nA* with quantitative difference (Williams et al., 2007). The digitally reconstructed morphology was reproduced from *NeuroMorpho.org* (Ascoli et al., 2007; Bausch et al., 2006). (D) A dentate gyrus neuron that transiently bursts just above its rheobase (red) elicits a spiking pattern with a strong *sfa* (grey) for a higher input current (Pierce et al., 2011). '*' indicates the unknown magnitude of the input current near rheobase. All voltage traces were digitized by *Hippocampome.org*. Experimental spike amplitudes are truncated. Calibration bars denote 200*ms* and 20*mV* in all panels. Goodness-of-fit is given only for key features (see appendix table A3 for all features). The experimental traces in panels A, B and D are intracellular recordings and the trace in panel C is a whole-cell patch clamp recording.

In the simplest case, a neuron exhibits spike patterns of the same class regardless

of the input current strength. For example, the three spike patterns recorded under

different input currents from a DG Total Molecular Layer neuron were identified as ASP.

(Fig 1A), and the two patterns recorded from a CA1 Basket neuron were identified as

NASP. (Fig 1B). Such simple-behavior neurons typically show different quantitative

features among different patterns of the same class. In the former example, the three

ASP. traces were experimentally recorded under $+0.075nA$ (red), $+0.100nA$ (black), and

$+0.200nA$ (grey) (Mott et al., 1997). The ISI counts (*nISIs*) are 5, 9, and 19, and *sfa*

magnitudes are 0.142, 0.114, and 0.056 respectively for the red, black and grey traces.

The model of this neuron type was constrained to quantitatively reproduce the spike

pattern features for similar input currents: *nISIs* of 5, 9 and 19, and sfa magnitudes of

0.142, 0.082, and 0.032 respectively for $+0.073nA$, $+0.102nA$ and $+0.205nA$. Appendix

Fig A1 illustrates examples of models reproducing frequency responses of neurons for a

range of input currents.

Additionally, a neuron can show more complex behaviors by eliciting patterns of

different classes under different input currents (Fig 4.1C-D). Both CA1 Trilaminar and

MEC LV-VI Pyramidal-Polymorphic neurons include ASP. in their phenotypes (grey

traces), but they show different dynamics close to their respective rheobases. Whereas the

former quickly fires a few spikes before going into a silence mode (ASP.SLN), the latter

shows delayed-spiking (D.NASP). The model quantitatively reproduces the

characterizing features of these different classes (see *pss* for ASP.SLN and *fsl* for

D.NASP). Also, note that the model reproduces the rebound-spiking behavior for a

hyperpolarizing input current, a known feature of CA1 Trilaminar neurons (Tricoire et

al., 2011).

Another level of complexity in spike pattern phenotypes is when the intrinsic dynamics show sharply distinguishable spike-pattern classes, which differ across super-families, under different input conditions. For example, a CA1 Bistratified neuron stutters (PSTUT) for +0.4nA, and spikes for +0.6nA (ASP.) (Fig 4.2A). A few neuron types and subtypes in the hippocampus exhibit such a complex phenotype, where PSTUT is typically observed just above the rheobase of a neuron (e.g. CA1 Neurogliaform (Price et al., 2005) and DG Total Molecular Layer subtype (Mott et al., 1997)). Our simple models capture the characterizing features of both PSTUT and ASP. (Fig 4.2A) under the right input conditions. It is worth mentioning that all PSTUT neurons are inhibitory neurons and the CA1 region has a proportionately larger number of these phenotypes (Klausberger and Somogyi, 2008; Komendantov et al., 2018). In many cases, however, the characteristic features of interrupted spiking can be only transiently present (Fig 4.2B). Here, a single pattern presents features of both bursting and spiking, where a relatively longer interval separates a few high frequency spikes (burst) from a train of regular spikes. In another set of examples, Granule and Hilar Ectopic Granule cells in the dentate gyrus (DG) show only transient bursting just above their respective rheobases (Fig 4.2C and 4.2D). However, for an increased input current, Granule cells still maintained the same TSWB.SLN pattern with quantitative differences such as increased number of spikes, whereas Hilar Ectopic Granule cells transitioned to ASP. These constrained representations of two different DG neurons fall under the same family of non-persistent bursting, but they are optimized to capture the finer quantitative differences in the input-dependent responses between these two neuron types. Thus, our

simple models do not only qualitatively capture the rich diversity of dynamical classes

defined systematically, but they are also quantitatively constrained representations of

experimentally recorded patterns from hippocampal neuron types.

3.2. Multi-compartment models as compact extensions of point-neuron models

The point-neurons with only two state variables, which were presented in the last

section, would tremendously reduce the computational cost of simulating large-scale

networks of hippocampal circuits relative to morphologically detailed Hodgkin-Huxley

type models. However, since they lack spatial dimension, they do not differentiate

synaptic inputs from different layers, unlike their biological counterparts. For example,

hippocampal pyramidal neurons receive entorhinal projections on the apical dendrites in

stratum lacunosum moleculare (SLM), and intra-hippocampal connections in stratum

radiatum (SR), thereby compartmentalizing synaptic integration of distinct laminar

inputs. While it is not possible to spatially segregate synaptic integration in a network of

point-neurons, it is of interest to see the effects of such segregated synaptic integration

mechanisms in a network. Hippocampome.org (version 1.4) identifies 87 neuron types

with their dendrites invading at least two layers. Therefore, for these neuron types, in

addition to point neuron models, we created compact-MC models with up to four

compartments. Here, each compartment corresponds to a hippocampal layer, allowing

layer-level connectivity specifications at the neuron type level.

One example for each of the four out of five possible multi-compartment layouts

are illustrated here, and the fifth layout is discussed in detail in Section 3.3. The somatic

compartment of a compact-MC model quantitatively reproduces the spike patterns

experimentally recorded from the soma of the respective neuron type for similar input currents (Fig 4.3 and Fig 4.4A). The number and layout of the coupled compartments is determined by the layers of dendritic invasion and known/possible soma locations of real neurons as illustrated by various examples in Fig 4.3. The dendritic compartments in a compact-MC model are less excitable and have higher input resistances than the somatic compartment (Appendix Fig A2 B) (Ledergerber and Larkum, 2010; Spruston, 2008).

A

CA1 Perforant Path Associated

+0.7nA
ASP.SLN

SP
SR
SLM
DG-SM

DG MOLAX

+0.4nA
PSTUT

SM
SG
H

MEC LIII Multipolar

+0.25nA
NASP
RBS

I
II
III
IV
V

DG AIPRIM

+0.2nA
ASP.NASP

H
SG
SMi
SMo
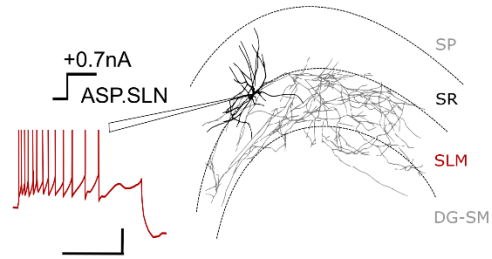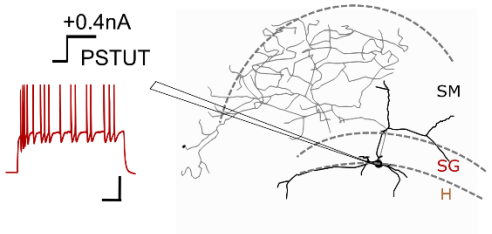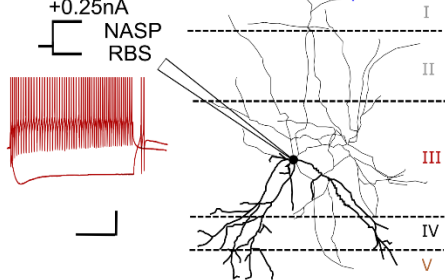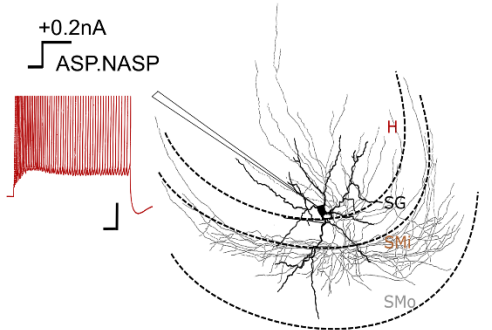
B
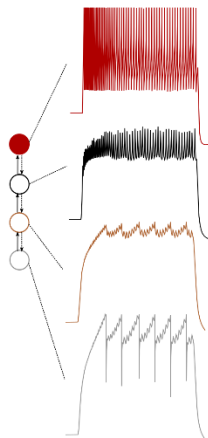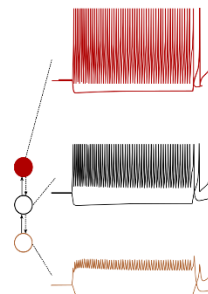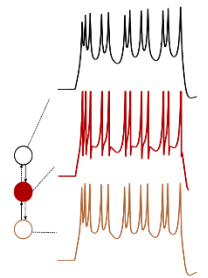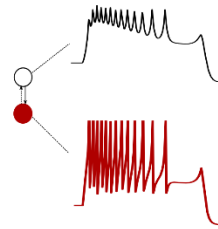
Figure 4.3: Multi-compartment models compactly extend point neurons to allow layer-level spatial context.
(A) Experimentally recorded somatic voltage traces (left) are given for four different morphological types (right). Dendritic invasion (darker) of layers and relative soma location determine the number and layout of compartments. (B) Layout of compartments coupled asymmetrically (left) correspond to the layers of dendritic invasion shown in A. Filled circles denote somata. Compartment responses for somatic input currents that are $\pm 0.01\,nA$ from experimental input are shown on the right side. See Fig 4 for quantitative comparison of spike pattern features, Supplementary Fig S2 for dendritic features, and Fig 5 for another possible 4-compartment layout. The digitally reconstructed morphology of DG MOLAX (Mott et al., 1997) was reproduced from *NeuroMorpho.org* (Ascoli et al., 2007). Other experimental traces were digitized by *Hippocampome.org* from the following sources (from top to bottom): (Vida et al., 1998), (Mott et al., 1997), (Canto and Witter, 2012) and (Lübke et al., 1998). Morphological abbreviations: SMi and SMo – inner one-third and outer two-third of stratum moleculare. Experimental spike amplitudes are truncated. Calibration bars denote $200\,ms$, $20\,mV$. The experimental trace ASP.SLN is an intracellular recording and the remaining experimental traces are whole-cell patch clamp recordings.
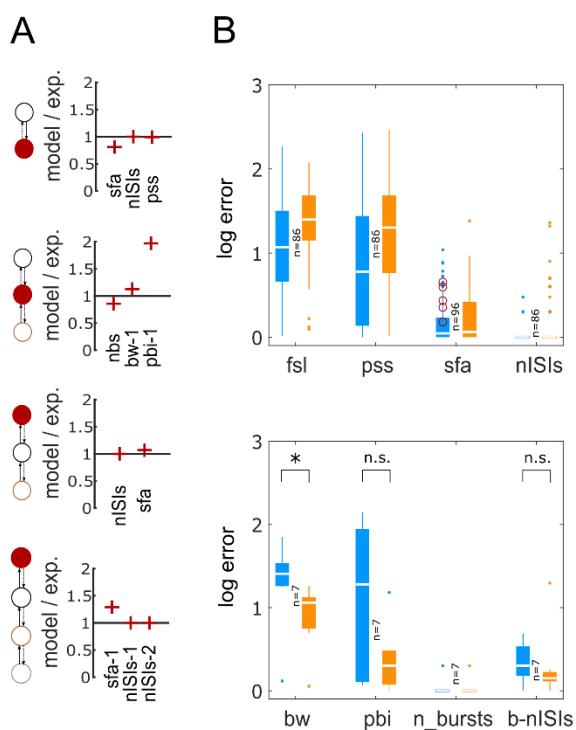
Figure 4.4: Accuracy of compact multi-compartment models in reproducing spike pattern features.
(A) The goodness-of-fit is given (only) for key features for each of the four examples from Fig 4.3 (see Appendix table A4 for all features). (B) Pairwise comparisons of accuracy between single-compartment (blue) and compact-MC (orange) models for spiking features (top) and bursting features (bottom). While single-compartment models, in general, showed smaller errors for spiking features, they did not satisfy statistical criteria for RASP.ASP. patterns (denoted by circles in top panel). See Appendix Fig A4 for an example for RASP.ASP. pattern. At the same time, compact-MC models generally improved the accuracy of bursting features (bottom) with a significant improvement in *bw* (p<0.005 for paired-sample *t*-test).

93

Furthermore, forward-coupling (from dendrite to soma) between compartments is just strong enough to evoke a somatic excitatory postsynaptic potential (EPSP) with an amplitude in the range [0.1, 0.9] mV for a single synaptic stimulation at a dendritic compartment and to achieve a forward-spike propagation (from dendrite to soma) ratio in the range [0.5, 1.0] (Appendix Fig A2C-D). Forward- and backward-coupling strengths are defined by $G \cdot P$ and $G \cdot (1 - P)$, respectively (see eqns 3 – 4). As mentioned in Methods, the backward-coupling (from soma to dendrite) is much stronger than the forward-coupling in most of our compact-MC models, consistent with the electrotonic profiles reported for various neuron types (Carnevale et al., 1997; Chitwood et al., 1999; Mainen et al., 1996). Such an asymmetric design for coupling enables the somatic compartment to dominantly define the model's overall intrinsic dynamics, while still preserving forward propagation properties for sub- and supra-threshold signals from dendrites. Thus, our multi-compartment models are compact extensions of point neuron models, which allow spatial contexts for synaptic integration.

Although the major motivation for creating compact-MC models is to allow synaptic segregation in a network model, we also investigated if additional dendritic mechanisms implemented in our compact-MC models could help achieve a better fitting of somatic spike patterns than their point-neuron counterparts. Therefore, we performed pairwise comparisons between the somatic spike pattern features of single-compartment and compact-MC models. In general, implementing additional dendritic mechanisms in the models only improved the accuracy of bursting features (Fig 4.4B). Interestingly, *fsl* and *pss* errors were higher in the models due to the addition of dendritic compartments.

However, it should be noted that each additional compartment not only adds two state variables, which require more computations for numerical simulation, but also adds ten open parameters (including coupling parameters) making it a more-challenging optimization task. Although our single-compartment models were able to reproduce quantitatively comparable experimental bursting/stuttering patterns (Fig 4.2) (see (Venkadesh et al., 2018) for two exceptions), compact-MC models significantly improved the accuracy of *bw*, a key feature of bursting/stuttering patterns (Fig 4.4B).

Furthermore, while the single-compartment models quantitatively captured various classes of adapting spike pattern phenotype such as ASP., ASP.SLN, ASP.NASP and RASP.NASP, they failed to reproduce RASP.ASP. patterns. These patterns exhibit a strong and rapid adaptation in the first few ISIs, which is then followed by a very weak and sustained adaptation. Interestingly, we found that such a combination was not possible in the IM (red circles in Fig 4.4B), unless additional dendritic compartments were included. Two different time constants (parameter 'a') for the adaptation variable (state variable U) were required for the somatic and dendritic compartments, respectively, in order to capture such complex transients in the soma. In our single-compartment models, RASP.ASP. is represented by RASP.NASP, since the adaptation followed by RASP. is usually very weak. See Appendix Fig A4 for an example.

3.3. Properties of dendritic compartments in compact-MC models

In addition to the features discussed in the last section, our compact-MC models show electrotonic structures and interplay between different compartments that are similar to those observed experimentally and in morphologically detailed multi-

compartment (morpho-MC) models. To illustrate this, here we present a 4-compartment model of CA1 Pyramidal neurons and discuss the spike propagation and voltage attenuation properties of apical compartments. First of all, the somatic compartment quantitatively captures frequency adaptation (Fig 4.5B), a characterizing feature of experimentally recorded spike patterns from CA1 Pyramidal neurons (Fig 4.5A (Chevaleyre and Siegelbaum, 2010) and Fig 4.5C - top). Secondly, the dendritic compartments (SR, SLM and SO) are less excitable and have higher input resistances than the somatic compartment (Fig 4.5C - bottom).
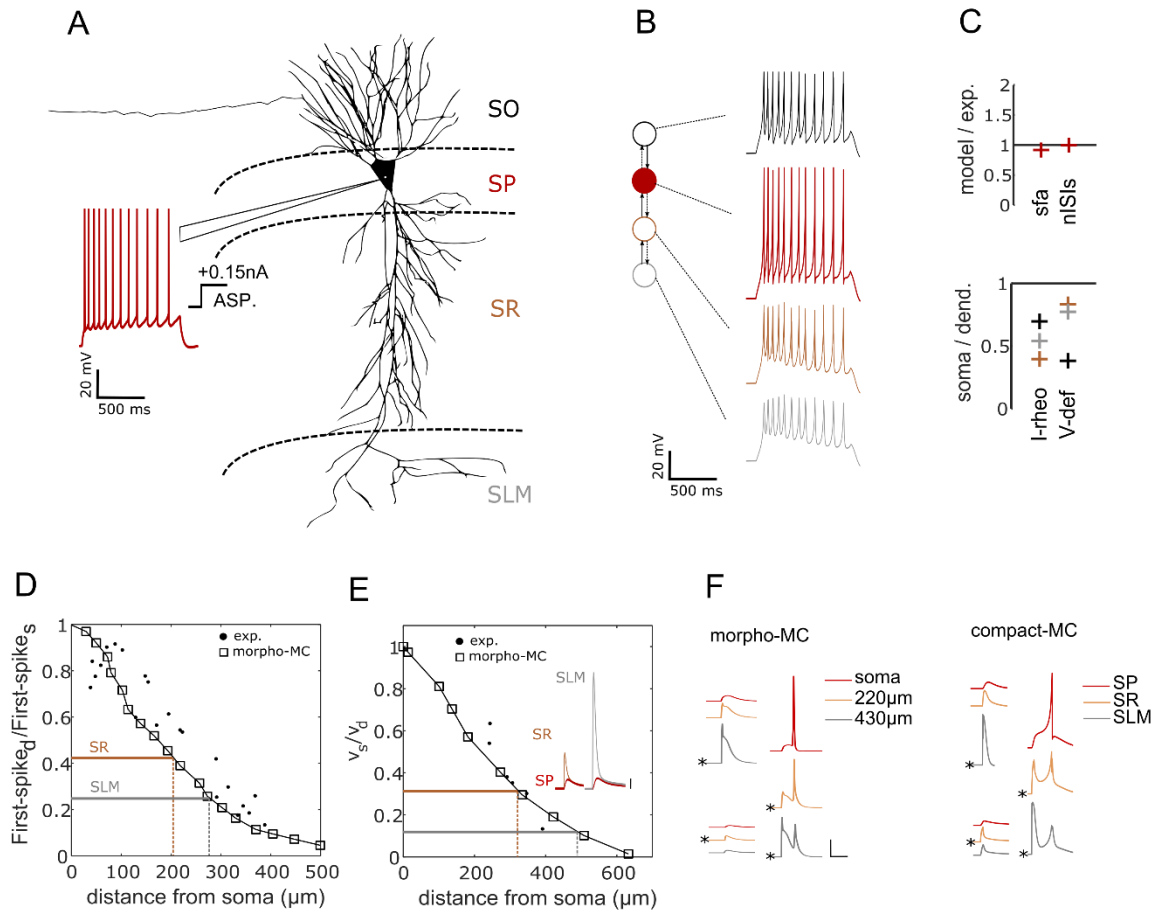
Figure 4.5: A 4-compartment model of CA1 Pyramidal neuron.
(A) A whole-cell patch clamp recording from a CA1 Pyramidal neuron (Chevaleyre and Siegelbaum, 2010) digitized by *Hippocampome.org*, and digitally reconstructed morphology of the same type (Ishizuka et al., 1995) reproduced from *NeuroMorpho.org* (Ascoli et al., 2007). (B) Layout of the compartments (left) and their responses to somatic input current of +0.15*nA*. (C) Somatic compartment reproduces key features that are quantitatively comparable to the experimental features (top). Minimum depolarizing input required to elicit a spike (I-rheo) and steady-state voltage deflection (V-def) for a hyperpolarizing input are higher in dendritic compartments than the somatic compartment (bottom). (D) Attenuation of first back-propagating spike from experimental recordings (exp.), in morphologically detailed multi-compartment model (morpho-MC) and in compact-MC model (horizontal lines; for the spike trains in B). First-spike$_d$ and First-spike$_s$ denote amplitudes of first spikes at dendrite and soma, respectively. Vertical lines indicate the distances of the morpho-MC sections from the soma that correspond to the attenuation profiles of proximal (SR) and distal (SLM) compartments in the IM. (E) Attenuation of dendritic EPSPs as they propagate towards the soma. V_s and V_d are amplitudes of EPSPs at soma and dendrite, respectively. Inset shows compartment responses for a single synaptic stimulation at SR (left) and SLM (right). Calibration: 0.2mV. (F) Conditional spike propagation in morpho-MC (left) and compact-MC (right) models of a CA1 Pyramidal neuron. '*' denote the stimulated compartment. A single spike initiated at the distal compartment (top left traces: stimulation at 430µm in SLM) failed to propagate to the soma. Additional depolarization level at the proximal compartment (bottom left traces: stimulation at 220µm in SR) facilitates propagation of spike initiated at the distal compartment (right traces) to the soma in both models. Experimental data digitized from (Golding et al., 2001) (D) and (Golding et al., 2005)(E). Multi-compartment CA1 Pyramidal model from (Jarsky et al., 2005) was used to obtain morpho-MC data. Calibration: 20mV, 20ms.

CA1 Pyramidal neurons exhibit strong attenuation of spike amplitudes as they propagate from the soma to apical dendrites (Golding et al., 2001; Hoffman et al., 1997). This attenuation has been attributed to the highly dense expression of transient A-type K+ conductance in the dendrites (Hoffman, 1999; Hoffman et al., 1997). We compared the attenuation of back-propagating spikes between compact-MC and morpho-MC models (Fig 4.5D and appendix Fig A3A). The compartments SR and SLM in the compact-MC model matched the attenuation profiles of morpho-MC sections at ~210µm and ~275µm, respectively, from the soma. However, it should be noted that the experimental dendritic recordings distal to ~300 µm showed a dichotomy of attenuation exhibiting either strong (71-87%) or weak (26-42%) attenuation (Golding et al., 2001), and we only included data corresponding to strong attenuation for comparison in Fig 4.5D.

In real neurons, integration of an EPSP is influenced by the location of the synapse, because the voltage attenuates more from a distal dendritic location to the soma,

than from a proximal location. This is partly due to the higher input resistances of more distal dendrites with smaller diameters. Such an attenuation profile will also hold for a uniform diameter cable with appropriate electrotonic asymmetry between the ends. The attenuation of EPSPs in our compact-MC models is consistent with experimental observations and morpho-MC simulations (Fig 4.5E and Fig A3B). The SR and SLM compartments in the compact-MC model matched the EPSP attenuation profiles of morpho-MC sections at ~320µm and ~470µm from the soma, respectively. It has been shown in some CA1 Pyramidal neurons that the synapses might be able to compensate for their distance by scaling their conductances in order to sufficiently influence somatic voltage (Magee and Cook, 2000; Nicholson et al., 2006). In our model, compared to a synapse stimulated at SR to evoke a somatic (SP) EPSP with an amplitude of $0.2mV$, a 4-fold increase in synaptic weight was required at SLM in order to evoke an EPSP with the same amplitude at SP (Fig 4.5E inset).

Furthermore, the distal compartments in our 3- and 4-compartment models rarely initiated a spike that successfully propagated to the soma, and additional depolarization levels at the proximal compartment facilitated forward-propagation of spikes from distal compartments. Such an interplay between proximal and distal compartments in a compact-MC model is qualitatively comparable to that of a morpho-MC model (Fig 4.5F). This is also consistent with the experimental observation that the activation of CA1 neurons by perforant path alone, which projects to SLM, is limited, but modest activation of Schaffer-collateral synapses in SR facilitates forward propagation of distal spikes (Jarsky et al., 2005). It has thus been suggested that Schaffer-collateral evoked EPSPs

"gate" perforant path spikes in CA1 Pyramidal neurons, underscoring the functional interaction between these different dendritic domains (Spruston, 2008). Such compartmentalization might be crucial to appropriately capture the integration of distinct laminar inputs and it is therefore notable that our compact-MC models with "active" dendritic compartments qualitatively reproduce such observations. Although voltage attenuation profiles could be modeled in IMs with passive dendritic compartments that are appropriately coupled, capturing the interplay between compartments such as gating as demonstrated here requires that the distal dendrites are optimized to initiate a spike.

Finally, spatially segregating the temporal integration of presynaptic spikes might enhance the range of responses of the postsynaptic neuron. We illustrate this using a simple example, where we compared the responses of single- (point neuron) and 2-compartment models of a CA1 Perforant Path-Associated neuron (from Fig 4.3) for arbitrary excitatory and inhibitory presynaptic spike trains (Fig 4.6). Following a spike-triplet, while the point neuron elicited a single spike, the 2-compartment counterpart exhibited different responses (2 or 0 spikes) depending on the location of integration of distinct spike trains. To what extent these differences influence the emergent network properties remains to be answered, but our models allow one to explore such questions.
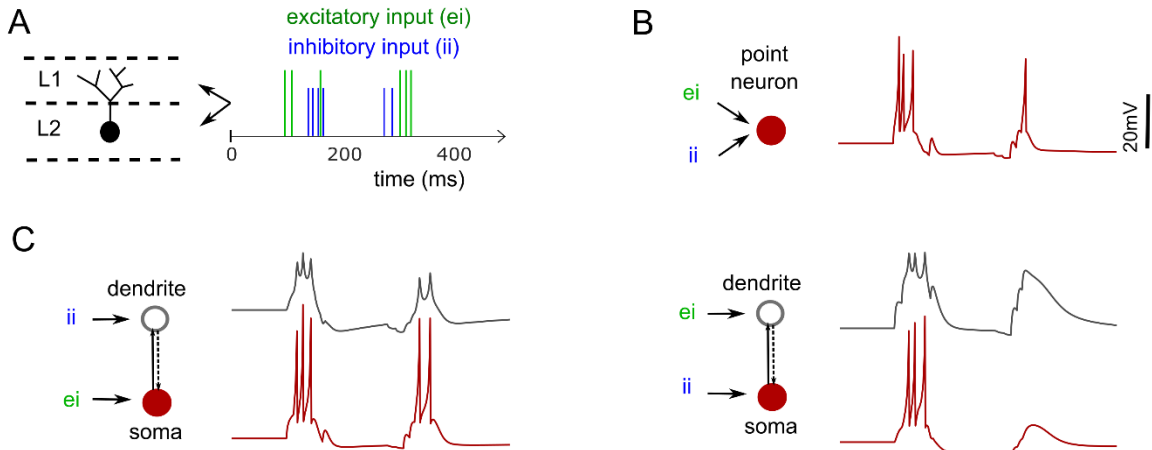
Figure 4.6: An example of segregated synaptic integration in a 2-compartment model.
(A) A schematic illustration of a biological neuron with its soma and dendrites in different layers L1 and L2. This neuron receives two distinct presynaptic spike trains in L1 and L2. (B) A simplified point-neuron model integrates both the excitatory and inhibitory presynaptic spikes at the same point. (C) A 2-compartment model (see Fig 3) can integrate distinct inputs in different compartments. The model behaves differently (left vs. right) depending on the location of integration of distinct inputs. Excitatory weight = 8.0 and Inhibitory weight = 1.5 for B and C, respectively. Dendritic synapses scale 4x (see Fig 4.5E inset for details).

3.4. Online repository of models: An enhancement to Hippocampome.org

A comprehensive list of models of 68 types and 52 subtypes of neurons is freely available at *Hippocampome.org*. Mapping the intrinsic dynamics of each neuron type in a low-dimensional model space enhances the existing information accumulated in this rich knowledge base of hippocampal neuron types.

All the single-compartment and compact-MC model parameters are presented in a matrix on the main page for easy browsing (Fig 4.7A). Within a Neuron page, models for all subtypes (if any) of the given morphological type are available for download. This page includes both the experimentally recorded voltage traces and simulated ones for all models (Fig 4.7B). Simulated spike patterns are also annotated with their class labels. Each type/subtype presents three downloadable files (Fig 4.7C): a *Fit-file* including both the experimental and simulated values for spike pattern features such as *fsl* and *sfa* for

100

each available pattern in a JSON format; an XPP (Ermentrout, 2002) script for single-compartment models; and a csv input file that includes both single-compartment and compact-MC models for CARLsim (Beyeler et al., 2015), a high performance GPU-based simulator. The Help section of Hippocampome.org provides links to explanatory pages on model definition, fitting, and simulation, including instructions to run the scripts and feature descriptions, under "Simulation of Firing patterns". This section also provides a link to download all single-compartment model descriptions in simulator-independent NeuroML format (Cannon et al., 2014). Furthermore, neuron pages include an online simulator, which allows the simulation of single-compartment dynamics for custom input.

3.5. Relationship between model parameters and biological features

A limitation of many phenomenological models such as the IM used here is the lack of biological interpretability of their parameters. One advantage of our approach of densely covering the diversity among neuron types is to allow one to explore relationships between the mathematical parameters of the IM and various known biological features. Our analysis revealed interesting trends and correlations in this regard.
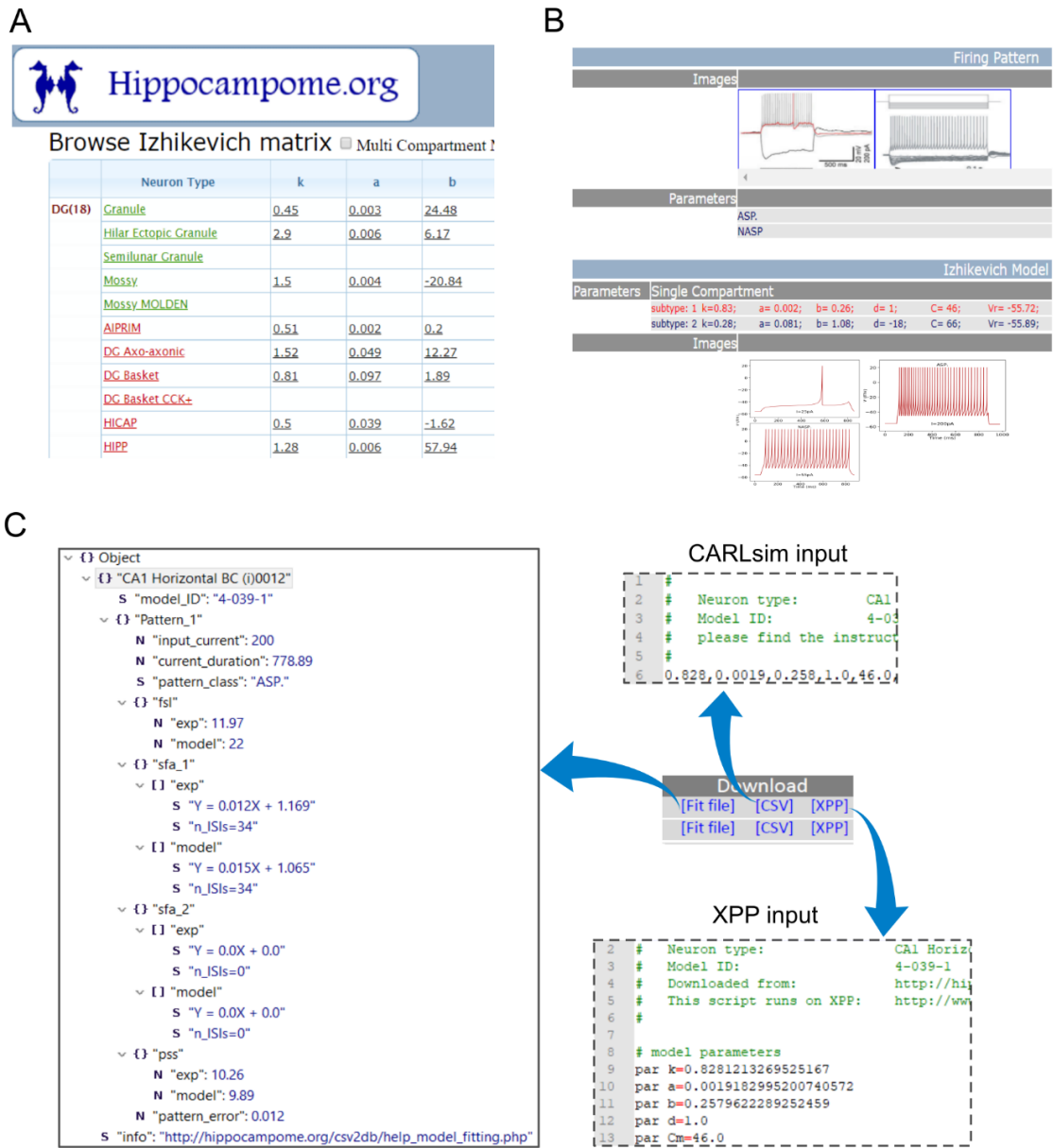
Figure 4.7: *Hippocampome.org* **provides a comprehensive list of models and ready-to-run scripts**. (A) Single- and multi-compartment model parameters for all neuron types are presented in a matrix form on the main page. Each row is linked to a Neuron page. (B) The Neuron page for each neuron type has been enhanced to include model parameters and simulated traces for all types and subtypes (if any). (C) The Neuron page provides the user with three downloadable files for each subtype: a *Fit-file* that lists both experimental and simulated features for each pattern, an XPP script to simulate single-compartment models, and a CARLsim input file for single- and multi-compartment models.

In general, the parameters of the IM collectively determine its spike pattern phenotype. However, the parameter '*b*', which determines if the model is an integrator

(b<0) or a resonator (b>0), sufficiently distinguishes two families of phenotypes. Most of the models that show delayed spiking near their depolarizing rheobases were found in the negative regions of 'b,' whereas models that show rebound spiking for hyperpolarized input currents were sharply restricted to the positive regions (Fig 4.8A). These results are consistent with the fact that 'b>0' is a necessary condition for rebound spiking (Izhikevich, 2007), and we find that most delayed spikers are integrators with the exception of the ones found in the narrow range 0<b<20. Thus, rebound (Fig 4.1C) and delayed (Fig 4.1D) spiking are, in general, instances of two qualitatively distinct types of intrinsic dynamics.

Next, we studied how much the parameter 'b' quantitatively influences the respective features in delayed and rebound spiking types. We used delay factors for the former and measured rebound rheobases for the latter. Increasing 'b' makes the model more rebound excitable until 'b' reached a value of +50, beyond which there was no noticeable effect (Fig 4.8B). Furthermore, there was no clear trend in the relationship between 'b' and delay factors. Thus, while 'b' alone can define a sharp qualitative change in the intrinsic dynamics, its interaction with other parameters, such as 'a,' determine precise quantitative features. In addition, pairwise correlations revealed several interesting trends between model parameters and electrophysiological or molecular properties of neuron types (Box 1) (also see Fig 4.8C for the data distributions and further analyses).
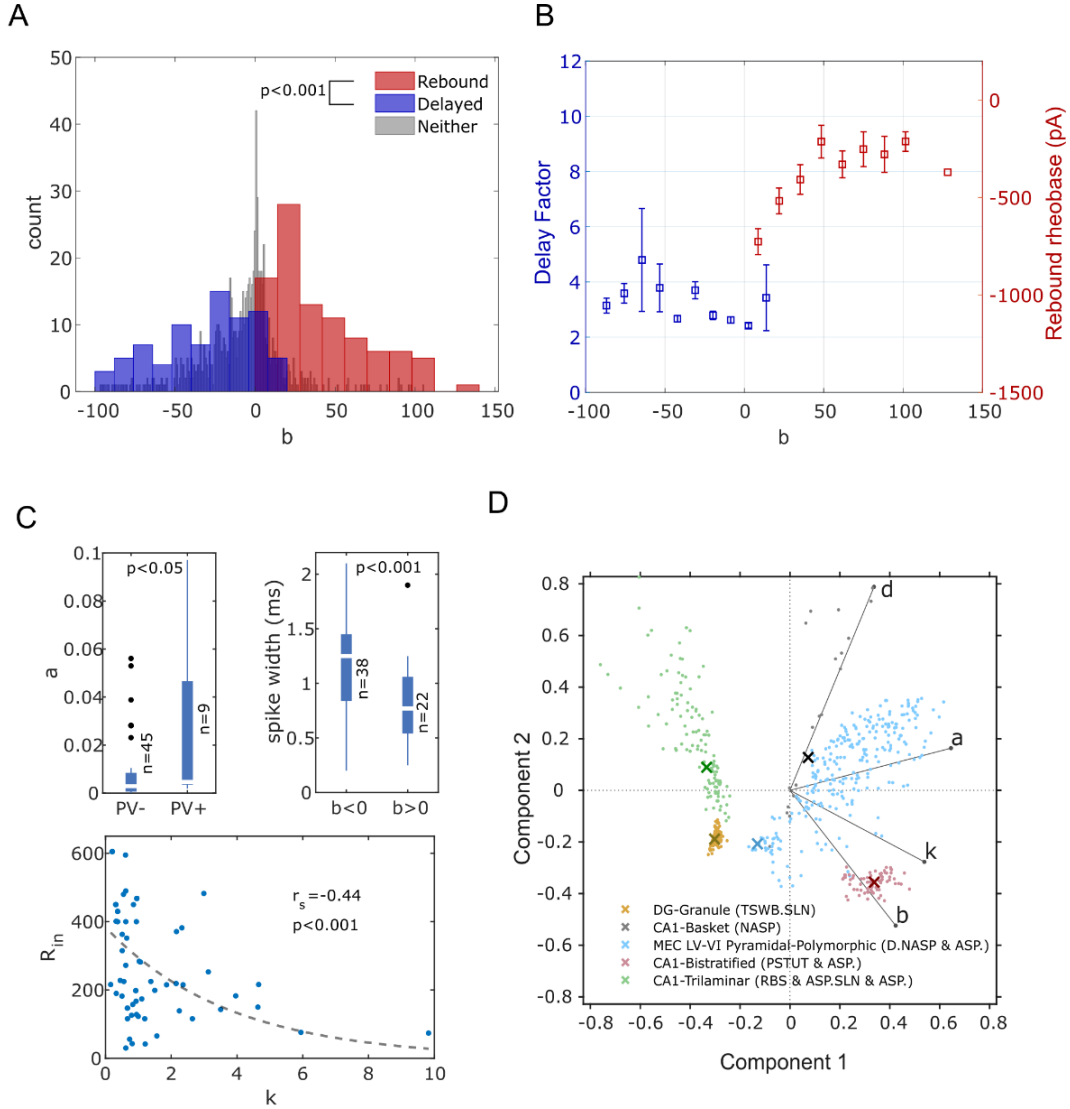
Figure 4.8:Relationship between model parameters and biological features.
(A) Distribution of parameter '*b*' for the models that show rebound spiking (red), delayed spiking (blue), and neither (grey). Rebound spiking types were sharply restricted to the positive region of '*b*.' In contrast, delayed spiking types were mostly found in the negative region (two-sample *t*-test). (B) Mean and SEM of delay factors and rebound rheobases of the models from the blue and red histogram bins respectively from A. Delay factor is the ratio between *fsl* and average of the first two *ISIs*. Rebound rheobase is the minimum magnitude hyperpolarizing current required to elicit rebound spikes. (C) Neuron types with positive expression of Parvalbumin (PV) have higher values for parameter '*a*' than the types with negative expression of PV (one-tailed Wilcoxon Rank-Sum test; $p < 0.0005$ in Anderson-Darling normality test) (top-left). Neuron types with negative values for '*b*' have wider spikes compared to the types with positive values for '*b*' (one-tailed Student *t*-test) (top-right). Input resistance (R_{in}) of a neuron type is negatively correlated with the parameter '*k*' ('r_s' denotes Spearman's Rank-Order correlation coefficient, n=67. An exponential fit was added for illustration only, and not used to measure correlation) (bottom). (D) Separation of spike pattern phenotypes in the space of first two principal components. 'x' denotes the best model for each type. Vectors denote the principal component coefficients of the respective parameters.

Box 1. Categorical correlations between model parameters and electrophysiological and molecular properties in hippocampal neurons

None of the neuron types that show **PSTUT** has a low value for *'k'* (p<0.01, n=43). In contrast, none of the neuron types that show **ASP.NASP** has a high value for *'k'* (p<0.05, n=43). Moreover, no neuron type with high input resistance (R_{in}) has a high value for *'k'* (p<0.001, n=15) (also see Fig 4.8C).

None of the 23 neuron types except CA3 Lucidum ORAX has **narrow spikes** and a low value for *'a'* (p<0.05). Moreover, clearly positive expressions of somatostatin (**SOM**) tend to co-occur with high values of *'a'* (p<0.05, n=18).

Neuron types with **wide spikes** tend to have negative values for *'b'* (p<0.001, n=31) (also see Fig 4.8C).

Low values of resting voltage (V_{rest}) tend to co-occur with high values of '*d*' (p<0.05, n=21). In contrast, no neuron type with positive expression of serotonin (**5HT-3**) has a high value for '*d*' (p<0.05, n=14).

The p values and sample sizes (n) pertain to Barnard's exact test for 2 x 2 contingency tables (see 'Methods').

Parvalbumin (PV)-positive and somatostatin (SOM)-positive interneurons have been shown to elicit narrow spikes of high frequency, with no or weak spike frequency adaptation (Jonas et al., 2004). Lower (and higher) values of '*a*' result in slower (and faster) recovery of adaptation variable '*U*' (Izhikevich, 2003), resulting in ASP. (and NASP) behaviors as we reported previously (Venkadesh et al., 2018). Consistent with the above facts, high values of '*a*' co-occurred with positive expressions of PV (Fig 4.8C) and SOM (Box 1), and low values of '*a*,' with one exception, never co-occurred with narrow spikes (Box 1).

Negative values of 'b' correspond to a saddle-node bifurcation, which is necessary for the neuron to elicit low-frequency spikes (Izhikevich, 2007). Our analysis

linked negative values of 'b' with wide spikes, a well-known property of regular (non-fast) spiking neurons. It should be noted that our modeling approach only enforces the temporal features of the overall spike patterns, such as *sfa*, and not the characteristics of individual spikes, yet makes expected links between the model parameters and spike width in the original (experimental) traces.

Cortical interneurons expressing serotonin receptor 3 (5HT-3) have been shown to elicit spike patterns with sustained *sfa* (van der Velden et al., 2012). The parameter '*d*' is the magnitude of offset for the state variable '*U*' during a spike reset, and high values of '*d*' prevent the model from exhibiting sustained *sfa*. As mentioned before, low values of '*a*' can result in sustained *sfa* (ASP.) behavior. However, the model would quickly reach the steady-state when a low value of '*a*' is combined with a high value of '*d*,' typically resulting in a RASP.NASP pattern. Consistently, high values of '*d*' never co-occurred with expressions of 5HT-3.

Parameter '*k*' scales the difference between the membrane potential state variable (V) and threshold voltage (V_t) (see eqn-1). Near resting equilibrium (V_r), higher values of '*k*' will require higher values of depolarizing '*I*' to compensate for the scaling effect to initiate a spike. Thus, '*k*' affects the excitability in the IM (appendix figure A5), and higher values of '*k*' result in lower excitability. It is known that neurons with higher rheobase (lower excitability) have lower input resistances (see for instance (O'Leary et al., 2010)). Consistent with these facts, high input resistances were never found with high values of '*k*.'

Another interesting correlation is that the PSTUT phenotypes were never found

for low values of 'k' (also see appendix figure A5). Our analysis revealed that the number

of periodic loops in the limit cycle attractor changes from infinite-period

(aperiodic/chaotic) to single-period, as the value of 'k' is decreased in PSTUT

phenotypes (not shown in figure). Such higher-periodic attractor loops are necessary to

capture the criteria for bursting/stuttering phenotypes in the IM. This suggests a

mathematically interesting relationship between 'k' and the maximum intrinsic

periodicity in the model. However, the in-depth study required to fully uncover this

relationship is beyond the scope of this study. Nevertheless, these correlations are also

consistent with our previous finding that PSTUT neurons never have high input

resistances (Komendantov et al., 2018).

Our modeling framework represents each neuron type as a cloud of possibilities in

the model parameter space (Fig 4.8D). Spike patterns produced by all the models in a

cloud strictly adhere to the criteria for the respective target qualitative class, but small

errors in the quantitative features were accepted to allow variabilities in the spike pattern

features (not shown here; see Venkadesh et al., 2018 for details on the optimization

framework design that allows such variabilities and for examples of ranges of

quantitative features). This provides a sampling region for each neuron type to create

network models with intragroup neuron variabilities. Several factors affect the size and

shape of these clouds: bursting/stuttering phenotypes typically result in smaller clouds

than spiking phenotypes. Similarly, spike patterns with unknown input currents (see Fig

4.1D) result in bigger clouds, since the models are searched in a broad range of input

currents for such cases. At present, these clouds are only identified for single-compartment models due to the computational cost of exploring higher dimensional parameter spaces of multi-compartment models.

4. Discussion

Hippocampal neurons show diverse features in their morphological, electrical and molecular properties (Harris et al., 2018). Hippocampome.org (v.1.4) identifies 122 types of neurons defined primarily based on their neurite invasion patterns in the hippocampal parcels (Wheeler et al., 2015). Their intrinsic spike pattern features were extracted from relevant publications, and systematic characterization of such features revealed diverse and complex spike pattern phenotypes among the 122 morphological types (Komendantov et al., 2018). The present work described a comprehensive set of simple models that are accurate quantitative representations of such spike pattern phenotypes. Correlation analysis revealed novel insights into the relationship between IM parameters and various biological features. In addition, point neuron models were compactly extended to create multi-compartment models with up to four compartments. Our compact-MC models, in addition to quantitatively reproducing the somatic spike pattern phenotypes, exhibited voltage attenuation profiles and interplay between different compartments that are consistent with experimental observations and simulations using morpho-MC models (Fig 4.5 & Fig A3).

The compact-MC models constitute a useful balance between computational efficiency and biological interpretability, but it is also important to recognize their limitations. The distal apical dendrites in CA1 Pyramidal neurons and their morpho-MC

108

models show activity-dependent attenuation of back-propagating spikes, such that the last spike in a spike train attenuates more markedly than the first spike (Golding et al., 2001; Hoffman, 1999). This is due to the activity-dependent changes in the ratio of sodium to potassium current in the dendrites (Colbert et al., 1997). Our compact-MC models did not show such activity-dependent attenuation of back-propagating spikes. The instantaneous reset of the voltage following its peak in the IM might be a limiting factor in this context. In addition, due to the lack of specific dendritic recordings and higher computational costs of optimizing the compact-MC models, we only enforced a minimum set of general constraints to create qualitatively accurate dendritic compartments. While we lack data to verify if the dendritic compartments in many of our models quantitatively reproduce the properties of their biological counterparts, their somatic compartments are quantitatively accurate (Fig 4.3). It should also be mentioned that we only considered coupling topologies with consecutive compartments for deeper layers, whereas, in real neurons, the deeper layer synapses may be on different branches than superficial layers. However, our compact-MC representations are useful for studies that aim to extend a baseline network of single-compartment neurons with minimum necessary dendritic properties to enable layer-level connectivity specifications.

Our single-compartment and compact-MC representations emphasize biological realism in the context of somatic intrinsic diversity, but it is also worth discussing their biological realism in the context of intra-neuron type variability in intrinsic dynamics. The intrinsic property of a neuron revealed in its spike patterns is determined by the types and precise distribution of the underlying ion channel conductances, such as sodium,

potassium, and calcium. However, it has been shown that similar dynamics can arise from a broad range of combinations of these conductances (Foster et al., 1993; Marder, 2011; Migliore et al., 2018; Rathour and Narayanan, 2014; Schulz et al., 2006). Consistent with this notion, our modeling framework represents a spike pattern phenotype as a cloud of possibilities in the parameter space (Fig 4.8D). Two closely related considerations motivate such representation.

The first issue is the existence of intrinsic variabilities in the spike pattern features among different neurons of the same type. For example, all the models representing the CA1 Trilaminar type (Fig 4.8D) were obtained using the features of voltage traces recorded from a single neuron (Fig 4.1C). While this particular neuron elicited 22 spikes with a sfa magnitude of 0.038 for 0.05nA, a different CA1 Trilaminar neuron might show slightly different values for these features, under the same input conditions, due to intrinsic variability. Furthermore, the recorded intrinsic spike pattern features might be influenced by the conditions such as the type of recording electrode and difference in animal strain, sex, or age. However, current knowledge about the intrinsic dynamics of these neuron types is limited to the representative traces that the researchers who studied these neuron types chose to publish. Therefore, we allowed a small range in the spike pattern features of a model as long as these features strictly adhere to the definitions of the respective target qualitative class. While the cloud boundaries defining such ranges are currently arbitrary, one could easily enhance our modeling framework to include more realistic ranges, when such ranges are experimentally obtained for all neuron types.

Secondly, neurons have intrinsic plasticity and undergo homeostatic regulations to maintain some constancy in the network activity (Desai, 2003; Desai et al., 1999; Marder, 2011; Marder and Goaillard, 2006; Turrigiano et al., 1994). In cell cultures, intrinsic homeostasis has been shown to modify non-synaptic ion channel conductances of pharmacologically isolated neurons. Such modifications shift the input-dependency of a neuron's responses based on the history of activity. For example, activity deprived neurons showed higher firing rates than control group for the current injections of the same magnitude (Desai et al., 1999). In another study, chronic isolation from normal inputs switched a neuron's response from tonic spiking to intrinsic bursting and this transition was reversed by applying a rhythmic inhibitory drive (Turrigiano et al., 1994). While these results suggest that each neuron has a working range that flexibly defines its input-dependent responses, such ranges likely preserve the overall qualitative spike pattern phenotypes (Marder and Goaillard, 2006). Our EA search for a cloud of models not only included the space of intrinsic IM parameters that define a phenotype, but also included a small range for input current (a $20pA$ range symmetrically encompassing experimental input current magnitude), allowing a reasonable flexibility for its input-dependency.

Considering the issues discussed above, an approach to modeling biological circuits should assume a flexible range for its components. While Hebbian plasticity rules can enable flexible ranges in synaptic conductances, the rules governing a neuron's intrinsic plasticity remain largely unknown. Although cell-autonomous regulatory rules have been proposed (O'Leary et al., 2015), from a network perspective, intrinsic

111

homeostasis has been shown to synergistically result from multiple interacting components in a circuit (Lane et al., 2016; Maffei and Fontanini, 2009). Exhaustively reductionist approaches to modeling brain regions specify *precise* descriptions at the level of ion channel conductances. While data gathered from different experimental conditions or inevitably from different animals drive such intrinsic descriptions, there is no guarantee that they specify dynamically compatible critical ranges necessary for a higher-level integrative property (Frégnac, 2017).

A large-scale approach to modeling a brain region, rather than being purely reductionist, should attempt to complement the descriptions of individual components with syntactically relevant descriptions at an integrative level. For example, temporal sequences of activity in ensembles of hippocampal neurons are correlated with the locations of an animal during spatial navigation (Dragoi and Buzsáki, 2006; O'Keefe and Recce, 1993; Skaggs et al., 1996). Such self-organizing ensembles of neurons, in general, have been suggested to form neural syntax (Buzsáki, 2010). Complex periodic structures in these ensembles, such as theta-modulated gamma activity patterns, should be enforced in a network model as sparse higher-level descriptions.

Future studies should aim to identify a family of models for an experimentally known network-level property, within the anatomical constraints of connectivity among hippocampal neuron types (Rees et al., 2016), using the sampling regions for those types created in this study. Then, the identified family of models should be evaluated for their predictive power, or one could investigate how the predictive abilities increase by scaling up the network or by adding more mechanisms, such as synaptic plasticity and spatial

context for synaptic integration. This approach emphasizes the goal of creating the simplest model with the most predictive power iteratively.

Finally, it is important to identify recurring patterns of self-organization in biological complex systems and translate such patterns into mathematical descriptions that could be enforced using optimization techniques, such as an EA that heuristically explores the given parameter space. If a biological complex system can indeed allow flexibility and compensation among multi-level components, then it suggests that a certain property could emerge from multiple, similar configurations in a network parameter space, which a metaheuristic approach (Yang, 2010), such as an EA, can take advantage of. While this might be a computationally expensive task, our simple models, with only two state variables per neuron, as opposed to hundreds in a biophysically detailed multi-compartment model, allow one to approach this problem much more efficiently. Future releases of *Hippocampome.org* are aimed at approximating the counts of different neuron types and mapping synaptic properties to potential connections. These enhancements will further narrow down the space of biological possibilities to create realistic large-scale models of hippocampal circuits.

CHAPTER 5: ITINERANT COMPLEXITY IN NETWORKS OF INTRINSICALLY BURSTING NEURONS[⊥]

Active neurons can be broadly classified by their intrinsic oscillation patterns into two classes characterized by periodic spiking or periodic bursting. Here we show that networks of identical bursting neurons with inhibitory pulsatory coupling exhibit itinerant dynamics. Using the relative phases of bursts between neurons, we numerically demonstrate that the network exhibits endogenous transitions among multiple modes of transient synchrony. This is true even for bursts consisting of two spikes. In contrast, our simulations reveal that identical singlet-spiking neurons do not exhibit such complexity in the network. These results suggest a role for bursting dynamics in realizing itinerant complexity in neural circuits.

1. <u>Introduction</u>

Neural systems exhibit transitions across multiple spatiotemporal scales. While individual neurons exhibit spiking events, which are sharp changes to the resting membrane potential, an ensemble of self-organized neurons can exhibit transitions among multiple coexisting metastable states (Fingelkurts and Fingelkurts, 2004; Freeman and Holmes, 2005; Tognoli and Kelso, 2014). In a metastable state, the interacting elements

---

[⊥] Authors: *Siva Venkadesh, Ernest Barreto[*], Giorgio A. Ascoli[*]*

[*]*co-senior authors*

114

enter into a transiently fixed relationship to each other, or "mode", before subsequently diverging and visiting a different transient mode. Metastability has been suggested to underlie the necessary coordination within and between brain regions (Tognoli and Kelso, 2014). Moreover, experimental evidence shows that the coordinated transitions among neural ensembles correlate with changes in an organism's behavior (O'Keefe and Recce, 1993; Skaggs et al., 1996; Jones and Wilson, 2005; Dragoi and Buzsáki, 2006; van der Meer and Redish, 2011).

Chaotic itinerancy (Tsuda, 2001) is a special case of metastability and has been observed in many complex systems, including globally coupled maps (Kaneko, 1997; Tsuda and Umemura, 2003) and electrically coupled point neurons (Fujii and Tsuda, 2004a, 2004b; Tsuda et al., 2004). Those coupled systems show endogenous transitions through a sequence of quasi attractors in the state space. Among possible scenarios underlying itinerancy in coupled systems (Alexander et al., 1992) are attractors with riddled basins (Tsuda, 2009), where initial conditions that are arbitrarily close to an attractor can generate trajectories leading to a different attractor. However, the intrinsic property of interacting elements that is necessary for the emergence of network itinerancy has not yet been clarified.

Neurons can be dynamically classified based on their intrinsic patterns of activation (Komendantov et al., 2019). In the current work, we constructed three separate networks of identical elements based on two broad classes of neurons: bursting neurons, which have either chaotic or two-loop periodic trajectories in the phase space, and spiking neurons, which have a single-loop trajectory. Analysis of the ensuing network

115

dynamics revealed several novel results. First, networks of bursting neurons showed transiently stable phase differences in pairs of neurons at the level of bursts, which transitioned to other transiently stable arrangements endogenously. Previous reports have described ensembles of bursting oscillators that synchronize on the bursting timescale and desynchronize on the spiking timescale (Ivanchenko et al., 2004). Our results show that synchronized bursting is only one of the multiple modes of stability observed in the network. We illustrate these complex dynamics using the burst-level phase differences between neurons as a variable of coordination. Second, we demonstrate that even networks consisting of bursting elements as simple as doublet-spikers can exhibit multiple stable phase differences and endogenous transitions. Third, singlet-spiking neurons only display, in contrast, perfectly phase-synchronized and desynchronized modes between pairs of neurons in the network. These results suggest that complex periodic oscillators such as bursters are crucial for the emergence of itinerant dynamics in neural networks.

2. <u>Burst-level phase difference as a coordination variable</u>

We use Izhikevich model (IM) neurons (Izhikevich, 2003), whose dynamics are described by (eqn1-2):

$$C \cdot \frac{dv}{dt} = k \cdot (V - V_r) \cdot (V - V_t) - U + I - I^{syn} \qquad (1)$$

$$\frac{dU}{dt} = a \cdot \{b \cdot (V - V_r) - U\} \qquad (2)$$

$$if\ V = V_{peak}\ then\ V = V_{min},\ U = U + d$$

Here, I is a constant current, and I^{syn} is the total synaptic current from all presynaptic neurons. The parameters were identified by an optimization framework (Venkadesh et al., 2018) to match the spike patterns of an isolated ($I^{syn}=0$) IM neuron to experimentally-obtained voltage traces from a stuttering CA1 neurogliaform cell (a GABAergic neuron type) from the rodent hippocampus (Price et al., 2005) ($k = 3.59, a = 0.01, b = -10, d = 120, C = 195, V_r = -63.5, V_t = -46.6, V_{peak} = 11.4, V_{min} = -50.6$). The bifurcation diagram with respect to the constant input current I was obtained by making a Poincaré cut at $V = V_{peak} - 20mV$ in the direction of increasing U after discarding 1s of initial transient behavior. This revealed period-doubling cascades leading to chaos (fig 5.1A). For chaotic bursting neurons, we set I=500pA. A network of 100 identical neurons, which were coupled using a delta function (eqn-3), was then constructed with

$$I_j^{syn} = \sum_{i=1}^{n} \delta_i . W \qquad (3)$$

where n is the number of presynaptic neurons connecting to the postsynaptic neuron j and W is the connection weight. δ_i is 1 (for a single time step) if neuron i spikes and is 0 otherwise. All networks were constructed with a connection probability of 0.7 and an inhibitory connection weight of 8 unless otherwise noted. Simulations were

performed on CARLsim (Beyeler et al., 2015) for a duration of 120s using the fourth order Runge-Kutta integration method with 100 steps per millisecond. The first 5s of simulation was discarded, and the analysis was performed for a total duration (ΔT) of 115s.

In order to extract the relative phases of bursts, the following steps were carried out for each neuron. First, discrete spike events were lowpass-filtered to obtain a continuous periodic signal which captures bursting cycles (Fig 5.1C, also see Fig S1A-C top). Then, the instantaneous phase of this signal was extracted using the Hilbert transform. Finally, the instantaneous phase differences between pairs of neurons were calculated for each millisecond in a given duration. We find that pairs of neurons predominantly exhibit phase differences near 0, $2\pi/3$, or $4\pi/3$ radians, and that they endogenously transition among these transiently locked states (Fig 5.1D).

Next, we studied the stability of transiently phase-locked modes and the nature of transitions among them. Specifically, we asked the following questions pertaining to pairs of neurons: (i) What is the locked duration in each of the three modes? (ii) For what fraction of the total duration (ΔT) does a pair exhibit stable phase differences in each of the three modes? (iii) What are the transition probabilities among the three modes?

The stability of a pair of neurons over a duration δT was quantified by averaging all the instantaneous phase differences $\Delta\theta(t)$ represented on a unit circle (eqn-4). $\delta T = 500ms$ unless specified otherwise.

$$Z_{\delta T}^{n} = \left\langle e^{n \cdot i \cdot \Delta\theta(t)} \right\rangle_{t \in [t_1, t_1 + \delta T]} \qquad (4)$$
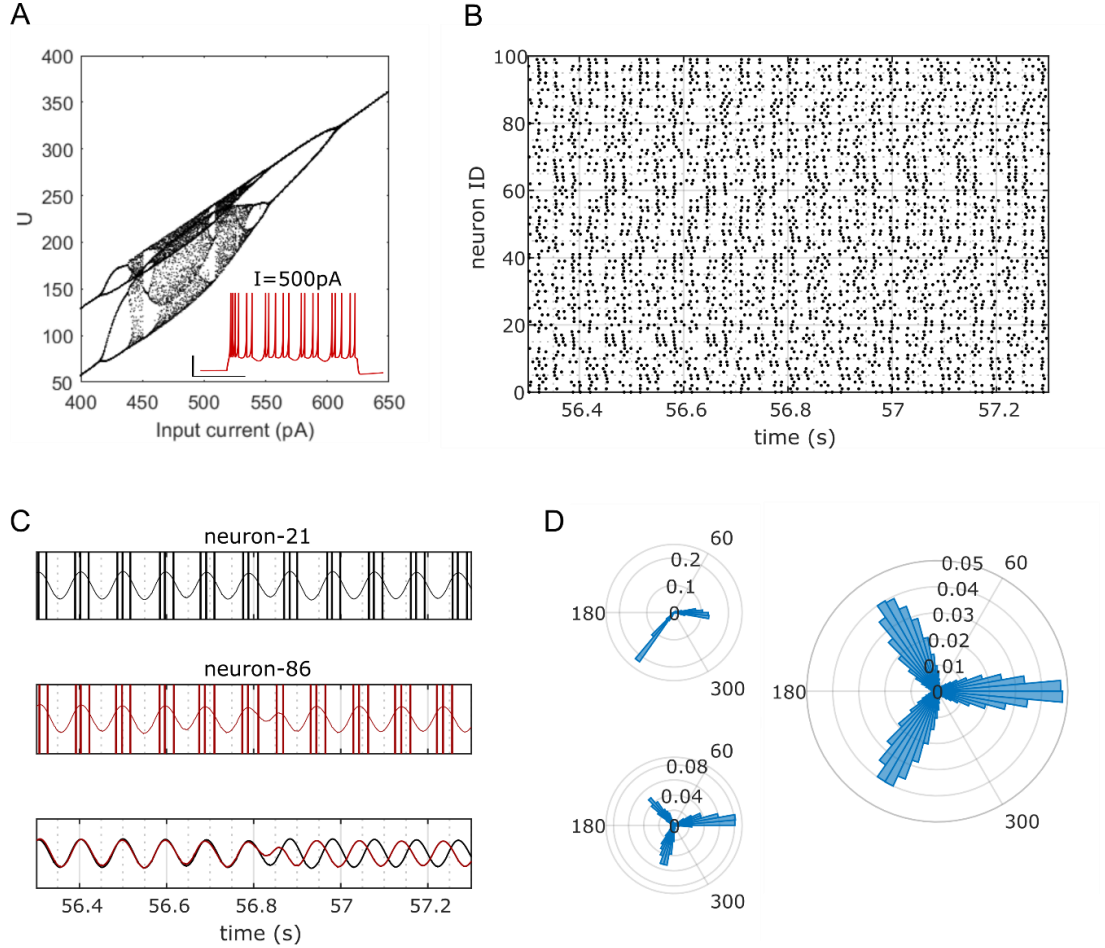
Figure 5.1: Endogenously transitioning phase-locked modes in a network of 100 identical bursting neurons.
Endogenously transitioning phase-locked modes in a network of 100 identical bursting neurons. A. Bifurcation diagram of the bursting neuron showing period-doubling cascades leading to chaos for increasing input current. Inset shows the activity pattern (voltage vs. time) of the isolated neuron. B. Raster plot showing the spike times of a network of neurons for a duration of 1 second. C. The discrete spike times of two neurons are transformed into a continuous signal corresponding to burst cycles (top & middle, also see Fig S1). The phase-locked mode endogenously transitions from **mode − 0** to **mode − 4π/3** (bottom). D. Normalized distributions of phase differences between the neurons shown in C during the same 1 second window as in C (left-top), and for 115 seconds (left-bottom). The distribution of phase differences between 100 randomly selected neuron pairs (right) show three clearly preferred locked modes (**0, 2π/3 , 4π/3**).

Here, $\langle f \rangle$ denotes the time average of f. The magnitude of $Z_{\delta T}^{n}$ was used as a

measure of stability. The parameter n indicates the number of stable clusters of phase

differences between pairs of neurons. For example, if the bursts of two neurons are

perfectly synchronized over δT, then $\left|Z_{\delta T}^{n=1}\right| = 1$. If their phase differences segregate into two equally populated clusters at 0 and π radians, then $\left|Z_{\delta T}^{n=2}\right| = 1$ and $\left|Z_{\delta T}^{n=1}\right| = 0$ (Golomb and Hansel, 2000).

A pair of neurons was deemed to be 'stable' or 'phase-locked' in a mode if $\left|Z_{\delta T}^{n=1}\right| \geq 0.95$ during δT. Such stable pairs were also assigned a mode 0, $2\pi/3$, or $4\pi/3$ based on the angular range in which the phase of $Z_{\delta T}^{n=1}$ lies (see Fig 5.1D for the bounds of the three ranges). In order to identify how long a pair remains phase-locked in a given mode, $\left|Z_{\delta T}^{n=1}\right|$ was calculated sequentially for non-overlapping δTs until either the pair was unstable ($\left|Z_{\delta T}^{n=1}\right| < 0.95$ for a duration δT) or a new mode was detected. The sum of all stable intervals (δTs) calculated from this sequential search was taken as the locked duration of the given mode. This gives a sequence of modes and a locked duration (in increments of δT) in each mode visited by a pair.

The locked durations of any of the three modes for 100 randomly selected pairs were exponentially distributed (Fig 5.2A-C), consistent with a previous report (Tsuda and Umemura, 2003). Pairs exhibit an expected locked duration of roughly 2s in all three modes. It is worth mentioning here that the expected locked durations do not give information about the fraction of the overall time ΔT that such locked modes were observed, because of their transient nature. We refer to this fraction as the fraction of locked time, given by $N \times \delta T/\Delta T$, where N is the total number of phase-locked δT intervals observed for a pair. The average of the fractions of locked time was 0.22 for each mode (Fig 5.2A-C insets).

In addition, the sequences of modes visited by 100 pairs were used to gain insights into the nature of transitions. The counts of transitions among the modes, which were given by the number of pairwise occurrences of modes in the sequence, were used to construct a 3x3 mode transition probability matrix (Fig 5.2D). Interestingly, there were several occurrences where pairs of neurons, after becoming unstable, failed to exhibit successful transitions. In other words, after losing stability from a certain locked mode, they were attracted back to the same mode rather than escaping to a different one (see Fig A7 for an example). The probability of successfully transitioning to a different mode (i.e. escape probability) is 0.72 from each of the three modes (Fig 5.2D). The apparently random nature of successful transitions from a given mode, which is noted by the approximately equal probabilities of transitions to the *other* two modes, is suggestive of a high entropic network exhibiting states that persist over several cycles of bursts.
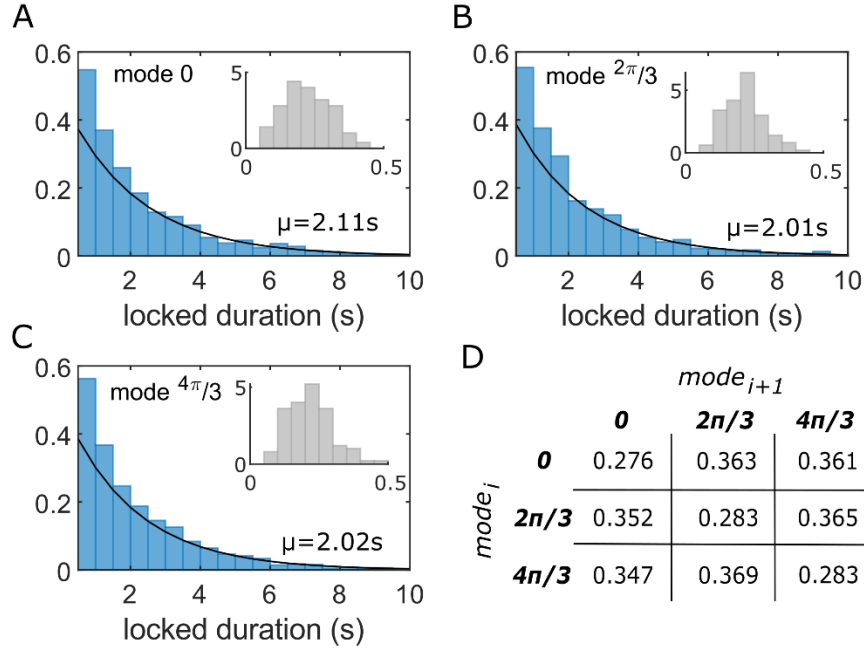
Figure 5.2: Stability and transitions in the network of chaotic bursting neurons.
A-C. Probability densities of locked durations in **modes − 0** (A), **2π/3** (B) and **4π/3** (C) are exponentially distributed with the expected locked durations (**μ**) of 2.11s, 2.01s and 2.02s with 95% confidence intervals [2.0, 2.24], [1.91, 2.13] and [1.91, 2.14] respectively for 100 randomly selected pairs. Insets show probability density distributions of the fractions of locked time for 100 pairs. D. Probabilities of transitions among the three modes. Each table entry denotes the probability of a pair transitioning from $mode_i$ to $mode_{i+1}$ after losing its stability from $mode_i$, where i denotes the sequence index.

3.   Itinerancy in the simplest form of bursting

Bursting dynamics include a spectrum of oscillatory patterns ranging from a double loop trajectory in the phase space (e.g. doublet-spiking observed for I=580pA in Fig 5.1A) to an aperiodic trajectory (I=500pA in Fig 5.1A). In this section, we consider networks separately consisting of doublet-spiking neurons (the simplest form of bursting with only two timescales) and singlet-spiking neurons. While the periodicity of oscillations in the chaotic-spiking IM neuron depends on the bifurcation parameter I (Fig 5.1A), here we considered IM neurons with the highest periodicity of only two for doublet-spiking and one for singlet-spiking (Fig 5.3A).

It was previously reported that bursting dynamics do not exist for low values of the parameter k in the IM neuron (see eqn-1) (Venkadesh et al., 2019). We obtained doublet- and singlet-spiking neuron models by only varying parameter k from the chaotic-spiking model ($k=1.5$; $I=175pA$ and $k=0.5$; $I=200pA$ for doublet- and singlet-spiking neurons respectively) (Fig 5.3). It should be noted that the bifurcation diagrams only illustrate the asymptotic behavior of the isolated neurons (Figs 5.1A&5.3A). Networks were constructed using these models and the steps explained in the previous section were carried out for the analysis (Fig A8, also see A6 A-C middle & bottom). We found that the network of doublet-spikers (ND) showed phase-differences that were clustered near 0, $2\pi/3$, and $4\pi/3$ radians (Figs 5.3B-C top & A8 A-B) like the network of chaotic-spikers (NC). Interestingly, the network of singlet-spikers (NS) only phase-locked near 0 radians (Figs 5.3B-C bottom & A8 C-D).

The average locked duration in the ND is less than a second for each of the three modes (Fig 5.4A). The average fractions of locked times are 0.1, 0.07 and 0.07 (Fig 5.4A inset), and the escape probabilities are 0.62, 0.66, and 0.67 for the modes 0, $2\pi/3$, and $4\pi/3$ respectively. Thus, the network of neurons that are intrinsically as simple as that of a doublet-spiking exhibits itinerant dynamics. Although the NS did not exhibit multiple metastable phase differences, its neuron pairs still exhibited simpler metastability, where desynchronized spiking occurred in between synchronized (mode 0) spiking (Fig A8 C-D). This is similar to the transitory dynamics reported in (Fujii and Tsuda, 2004a, 2004b; Tsuda et al., 2004), where the networks of point neurons coupled with gap junctions alternated between synchronized and desynchronized states. The NS showed an average
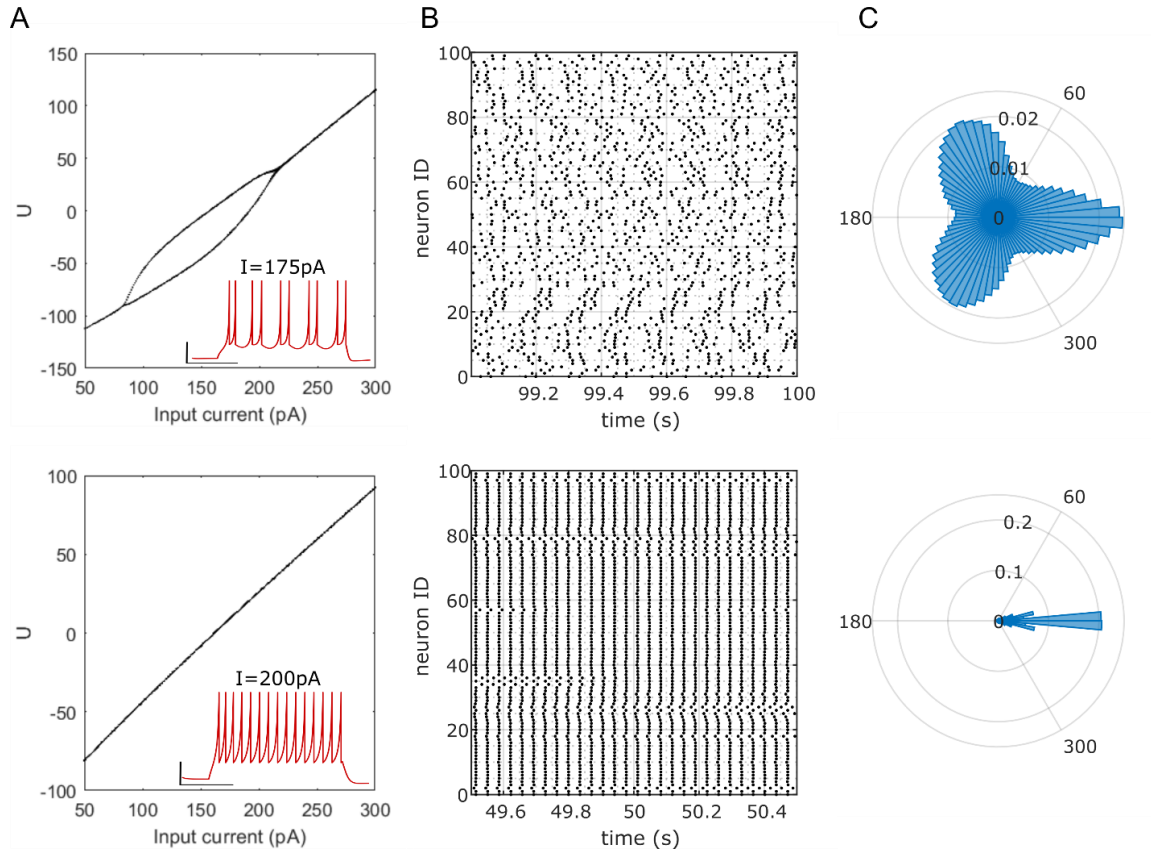
Figure 5.3: Dynamical complexity is preserved in the network of doublet- (ND) spiking neurons
A. An isolated neuron with a 2-loop limit cycle attractor (spike doublets shown in inset) was obtained by reducing the value of parameter k from the chaotic- model to 1.5 (top). Further reducing the value of k to 0.5 result in a singlet-spiking model (bottom). B. Raster plot shows the spike times of ND (top) and NS (bottom) in the network for a duration of 1 second. C. The phase differences between 100 randomly selected neuron pairs in the ND (top) show three preferred locked modes (0, $2\pi/3$, $4\pi/3$), although these distributions have a wider spread compared to NC (see Fig 1). There is only a single preferred locked mode for NS (bottom), although they show scattered distributions of non-zero phase differences (see Fig S3).

locked duration of over 5s and an average fraction of locked time of 0.74 in mode 0 (Fig 5.4C left). While the transitions among the three metastable modes in NC and ND are generally abrupt (for instance, see Fig 5.1C), the transitions between successive synchronized states in NS showed scattered phase differences (Fig A8C). The occasionally slower dynamics of such transitions lead to a few stable δTs in mode $2\pi/3$.

However, the fraction of locked time in mode $2\pi/3$ is negligible (Fig 5.4C right, also see Fig 5.3C bottom).
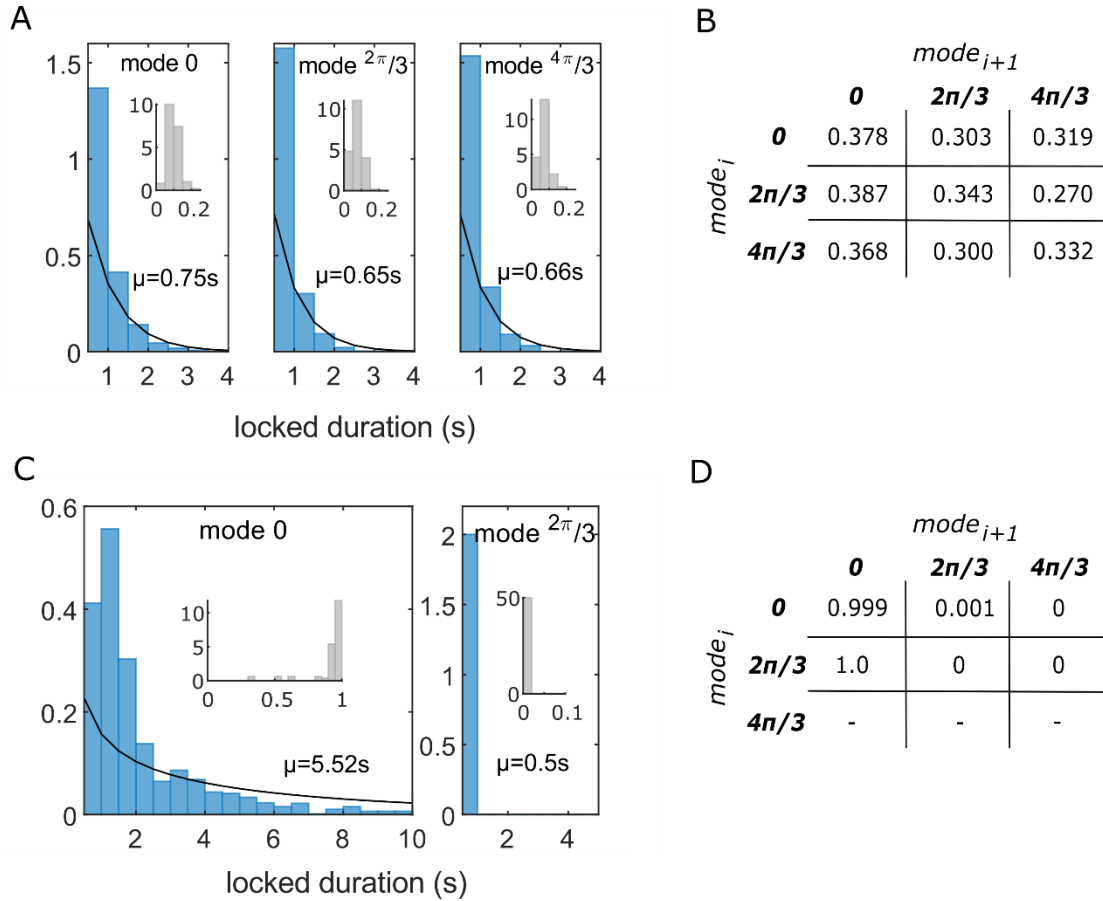
Figure 5.4: Stability and transitions in network of doublet- (ND) and singlet- (NS) spikers.
A. Distributions of locked durations in **modes** $-$ **0** $2\pi/3$ and $4\pi/3$ are exponentially distributed in ND with the expected locked durations (μ) of 0.75s, 0.65s and 0.66s with 95% confidence intervals (CI) in [0.71, 0.79], [0.61, 0.68] and [0.63, 0.70], respectively, for 100 randomly selected pairs. B. Probabilities of transitions among the three modes in ND. C. The locked durations in **mode** $-$ **0** (left) roughly follow a gamma distribution in NS with $\mu = 5.52s$ ($\alpha = 0.54$ with CI [0.51, 0.57] and $\beta = 10.29$ with CI [9.41, 11.25] are the shape and scale parameters, respectively, of the gamma distribution, and $\mu = \alpha \times \beta$). There are 2 occurrences of locked **mode** $-$ **2$\pi/3$** (right), which are due to the slower phase scattering dynamics. Insets show probability density distributions of the fraction of total time a pair was locked in the mode. D. Probabilities of transitions in NS show no stable transitions to the **mode** $-$ **4$\pi/3$**.

The itinerant dynamics that emerges from the collective interaction of complex-periodic spiking neurons is also sensitive to the network connectivity parameters such as W. Therefore, we studied how the tri-stability (as illustrated in Fig 5.1D – right and Fig 5.3C – top) is affected by changing the strength of the inhibitory connections. We plotted two measures, $\left|Z_{\Delta T}^{n=1}\right|$ and $\left|Z_{\Delta T}^{n=3}\right|$ (see eqn – 4) for connection weights in [0, 40]. For a weakly connected NC ($W = 4$), both measures are near zero (Fig 5.5A – left) because the phase differences between pairs of neurons are mostly asynchronous and they are uniformly distributed with predominantly transitioning δTs (Fig 5.5B – top). At $W = 8$, $\left|Z_{\Delta T}^{n=3}\right|$ reaches its maximum value of 0.62, while $\left|Z_{\Delta T}^{n=1}\right|$ remains near zero. These measures correspond to the tri-stability illustrated in Fig 5.5B – middle, where the stable δTs are more prevalent than the transitioning ones. Similarly, the maximum of $\left|Z_{\Delta T}^{n=3}\right|$ when the corresponding $\left|Z_{\Delta T}^{n=1}\right|$ is near zero is only 0.22 for the ND (Fig 5.5A – middle), as their phase differences are more spread-out (Fig 5.5C – bottom) than the most stable NC. Furthermore, the ND required stronger inhibitory connections ($W = 20$) to reach this maximum (Fig 5.5A – middle). Interestingly, for weaker connections ($W = 4$), ND's metastability is qualitatively similar to that of the NS, where $\left|Z_{\Delta T}^{n=1}\right|$ scores higher than $\left|Z_{\Delta T}^{n=3}\right|$ (Fig 5.5A – middle & right) and the modes $2\pi/3$ and $4\pi/3$ are nearly non-existent (Fig 5.5C – top & Fig 5.5D).

Thus, there are optimal connection weights that maximize the stability of the states visited by the networks of bursters. In addition, the network of simpler bursters exhibits states that are less stable than those of the network of more complex bursters.
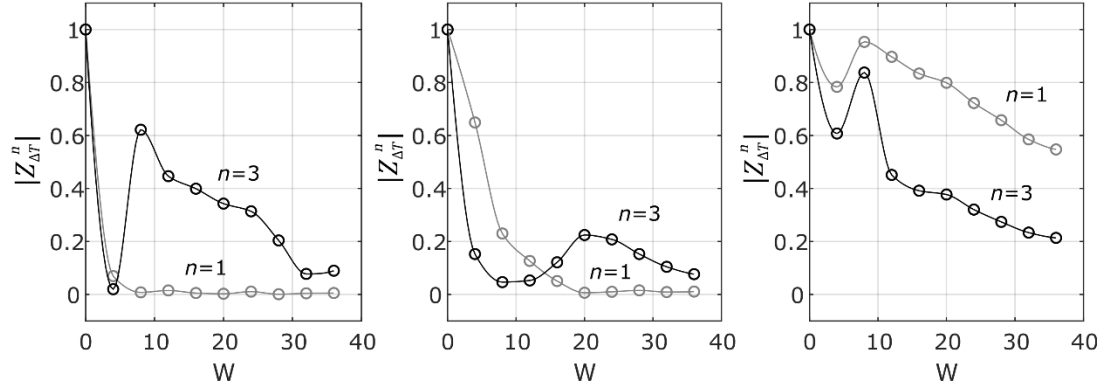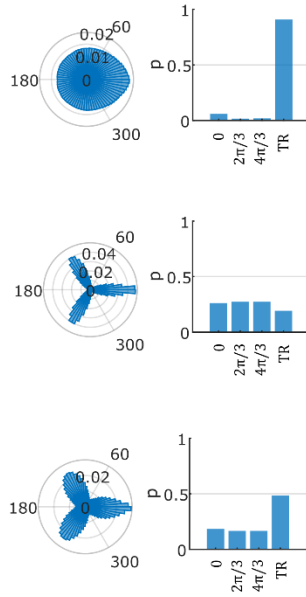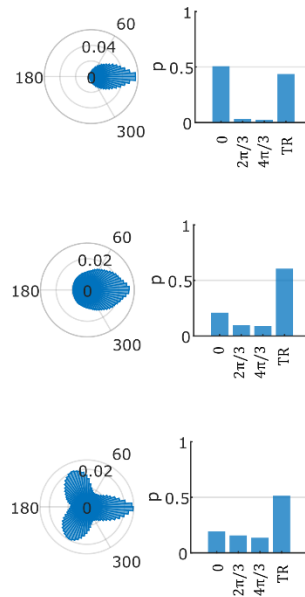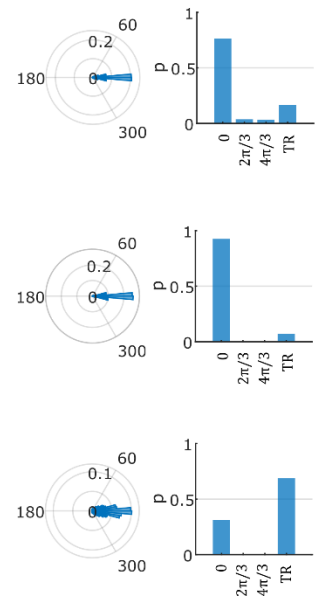
Figure 5.5: Stability as a function of connection weight.
A. Magnitude of the average of phase differences between 100 randomly selected pairs of neurons (see eqn – 4) for NC (left), ND (middle) and NS (right). $\Delta T = 115s$. Note that $W = 0$ corresponds to isolated neurons that fire in perfect synchrony. Therefore, $|Z_{\Delta T}^n| = 1$ for any n. B. Distributions of phase differences for weakly connected NC (top-left) and distributions of the probabilities of the modes visited (top-right) Here, $W = 4$. A total of 1000 δTs was analyzed to calculate the probabilities. $\delta T = 100ms$ and 'TR' denotes transitioning δTs. B – D: Distributions of phase differences and the probabilities of visited modes when $W = 4$ (top), $W = 8$ (middle) and $W = 20$ (bottom) for the NC (B), ND (C) and NS (D).

4. <u>Summary and discussion</u>

Metastability is a useful framework to characterize the existence of synchronized and desynchronized states in a system (Shanahan, 2010; Tognoli and Kelso, 2014). However, the relationship between metastability and itinerancy has not been very clear. It has been suggested that the appearance of metastable states is a necessary but not sufficient condition for itinerancy (Tsuda, 2015). Along this line, a few scenarios for the existence of itinerancy have been proposed (Tsuda, 2009). The current study finds that while the networks of both the simple-periodic (singlet-spiking) neurons and complex-periodic (chaotic- and doublet-spiking) neurons show metastability, only the latter class showed multiple synchronized modes.

The chaotic-spiking model used in this work was obtained by tuning the IM parameters to reproduce the stuttering behavior of a neurogliaform interneuron (Price et al., 2005). Neurogliaform interneurons in the cerebral cortex connect nonspecifically to almost all other neuron types within their somatic layer as well as across layers (Jiang et al., 2015). In addition to electrical and chemical synapses, they also influence target neurons by volume release of GABA and were suggested to play a crucial role in broadly regulating the synchronized activity of neural circuits (Price et al., 2005; Oláh et al., 2009; Rudy et al., 2011), a role aptly described as "master regulators" (Jiang et al., 2015).

The network of identical simple-periodic spiking neurons did not exhibit itinerant complexity. However, it should be noted that the broad class of such simple-periodic neurons include a range of spiking timescales such as the regular spiking observed in many pyramidal neurons and fast-spiking observed in many Parvalbumin positive

128

interneurons near their respective rheobases. A system can exhibit bursting if it consists of mutually interacting fast and slow subsystems, where the slow dynamics modulate the fast-spiking (Izhikevich, 2007). Further work is required to determine if the additional mechanisms that are necessary to induce bursting in simple-periodic neurons are sufficient for the emergence of itinerant complexity.

CHAPTER 6: SUMMARY AND FUTURE DIRECTIONS

In this dissertation, I have created an optimization system to quantitatively match the Izhikevich model responses to experimentally recorded spike patterns. Using this system, I have captured a variety of complex spike pattern phenotypes experimentally observed among over a hundred neuron types/subtypes in the rodent hippocampus. Such a comprehensive coverage of intrinsic diversity in a phenomenological modeling system will significantly reduce the computational burden of simulating large-scale circuits of the hippocampus. In addition to the compact model descriptions of neuronal intrinsic dynamics, I have characterized the collective dynamics of two broad classes of neurons in terms of their metastable features. While the ensemble of identical spiking neurons showed synchronous and asynchronous states, the ensembles of identical bursting neurons showed multiple metastable states.

It has been proposed that the transitions among metastable states in the brain are the temporal identities of moment-to-moment transitions in consciousness, and a single moment of experience, in and of itself, is irresolvable in time (Freeman, 1999). In a separate line of inquiry, integrated information theory (IIT) (Tononi et al., 2016) postulates about the necessary properties of conscious physical systems, and it formulates complexity measures that quantify to what extent a system of mechanisms is both integrated and differentiated (Oizumi et al., 2014).

The mathematical framework of IIT formally defines quantities such as cause-effect information, which measures the specificity of a mechanism in a certain state in constraining the system's past and future states, and integration, which measures the irreducibility of the information generated by the whole system to the information generated by its parts. A set of elements is partitioned into all possible subsets, and their elements are perturbed into all possible states to identify the local maxima of information integration. Moreover, IIT postulates that the global maximum of integrated information (ϕ^{Max}) is specified at a *definite* spatiotemporal grain in conscious physical systems. However, identifying ϕ^{Max} is only possible for small and simplified systems due to combinatorial explosion. Using systems of (<10) simplified neuronal-like elements, it was demonstrated that ϕ^{Max} can occur at a coarser-grained level in space (grouped elements) and time (grouped timesteps) (Hoel et al., 2016).

The relationship between the temporal grain size of information integration and metastability has also been previously discussed (Tononi, 2012). It was suggested that the timescale of metastable attractors in the cortex could correspond to the macro-time scale at which integrated information reaches a maximum. Future studies can verify this in small bursting neural networks, which exhibit distinguishable states at multiple timescales as illustrated in chapter – 5. At the timescale of a few milliseconds, a neuronal state can be described by the presence or absence of a spike. At a coarser-grained timescale of tens of milliseconds, a neuronal state can be described as one of low-mean or high-mean firing states as illustrated in (Tononi et al., 2016). Finally, the state of a neuron in a self-organized ensemble can also be described by its relative phase at burst-

level as shown in chapter – 5. The relative phase of a neuron that is stable over several cycles of bursts is a temporally coarse-grained description of its state, and it does not average or approximate finer-grained events such as spikes or bursts that constitute the attractor macro-states. By measuring integrated information (ϕ) across these temporal grains, one can see if ϕ^{Max} indeed occurs at the temporal grain that corresponds to the metastable attractors.

Future studies can also explore the possibilities of relating metastable attractors at the postulate level of IIT. Particularly, parts of IIT's postulate of exclusion, which apply to temporal grains, could be expanded in a way that would allow for a direct mathematical translation of temporally coarse-grained (macro) states into transient attractors. This would reduce the computational burden of exhaustively searching through all possible temporal grains to identify the relevant macro state and allow for more rigorous validations of other postulates of IIT. Furthermore, the presence of gradients in ϕ across different levels of spatial groupings of elements (Hoel et al., 2016) suggests that a heuristic search, in place of an exhaustive one, could be employed to accelerate the process of identifying optimal spatial grain in large networks. Such scalable mathematical translations of IIT's postulates could pave the way for evolving biologically realistic and causally autonomous neural networks.
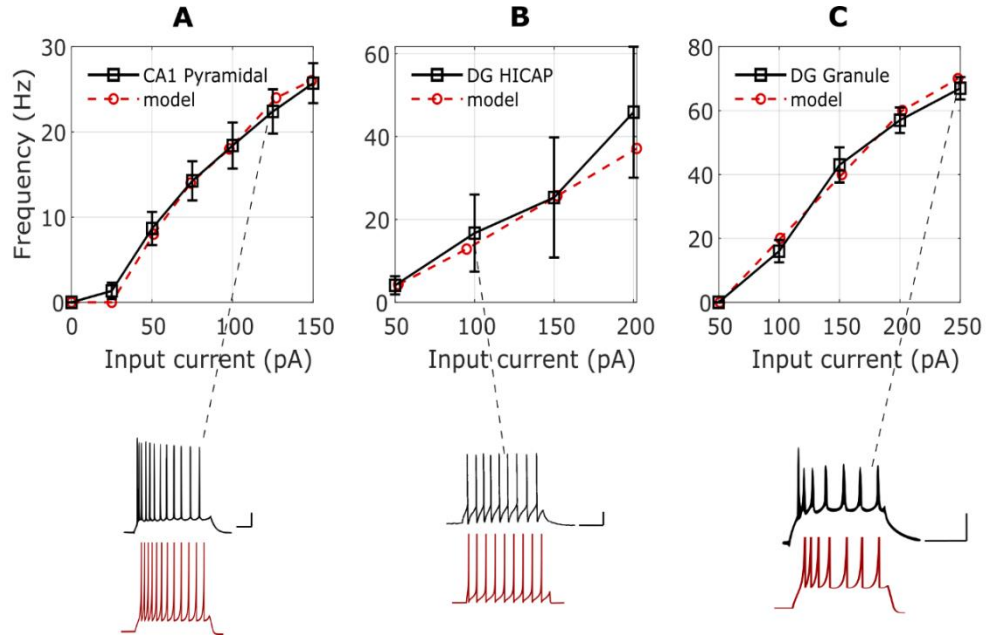
A1 Fig. Models reproduce frequency-response curves of different neuron types. Experimentally measured mean firing frequencies of (A) CA1 Pyramidal (Babiec et al., 2017), (B) DG HICAP (Mott et al., 1997) and (C) DG Granule (Yun et al., 2006) for various input current magnitudes (±5pA), were used to constrain the model responses. Representative experimental (black) and corresponding model (red) traces are given in the bottom. Calibrations: 20mV, 100ms (left); 20mV, 200ms (middle); 40mV, 40ms (right).
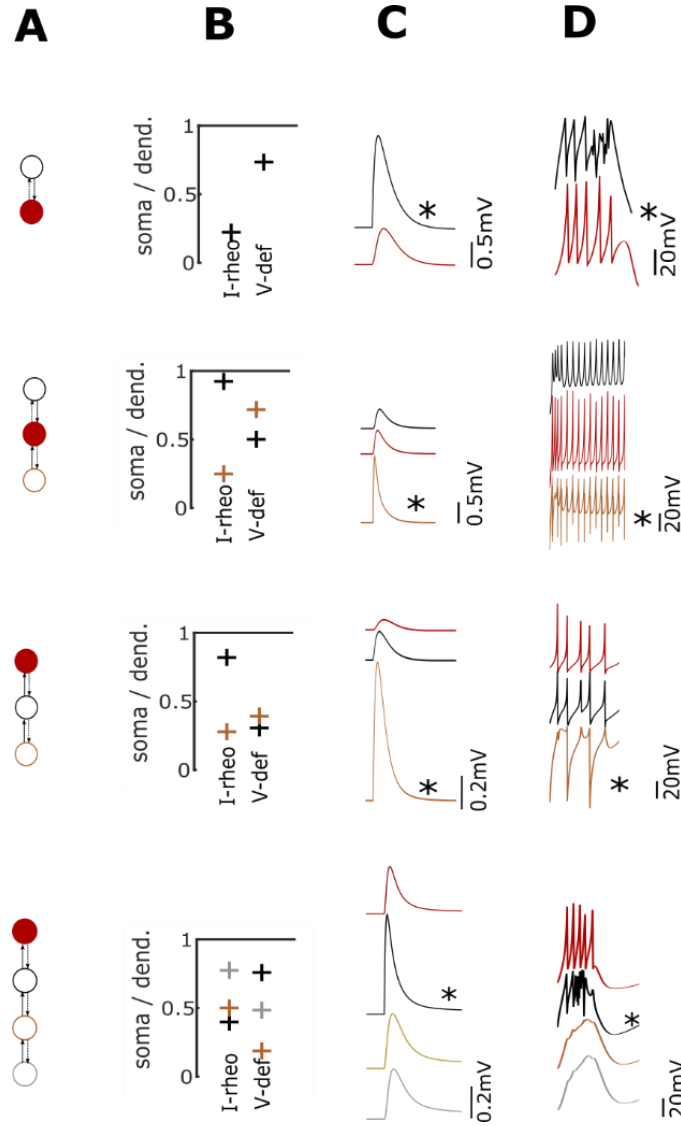
A2 Fig. Multi-compartment models capture qualitative dendritic properties and sub- and supra-threshold signal propagation. (A) Four different layouts of asymmetrically coupled compartments from Fig 4.3. (B) Minimum depolarizing input required to elicit a spike (I-rheo) and steady-state voltage deflection (V-def) for a hyperpolarizing input are higher in dendritic-compartments than in the somatic-compartment. (C) A single synapse stimulated at a dendritic-compartment (denoted by '*') evokes a unitary EPSP at the somatic-compartment (red traces), with an amplitude in the range [0.1, 0.9] mV. (D) Coupling mechanism implemented in the models allows forward propagation of spikes initiated at a dendritic-compartment (denoted by '*').
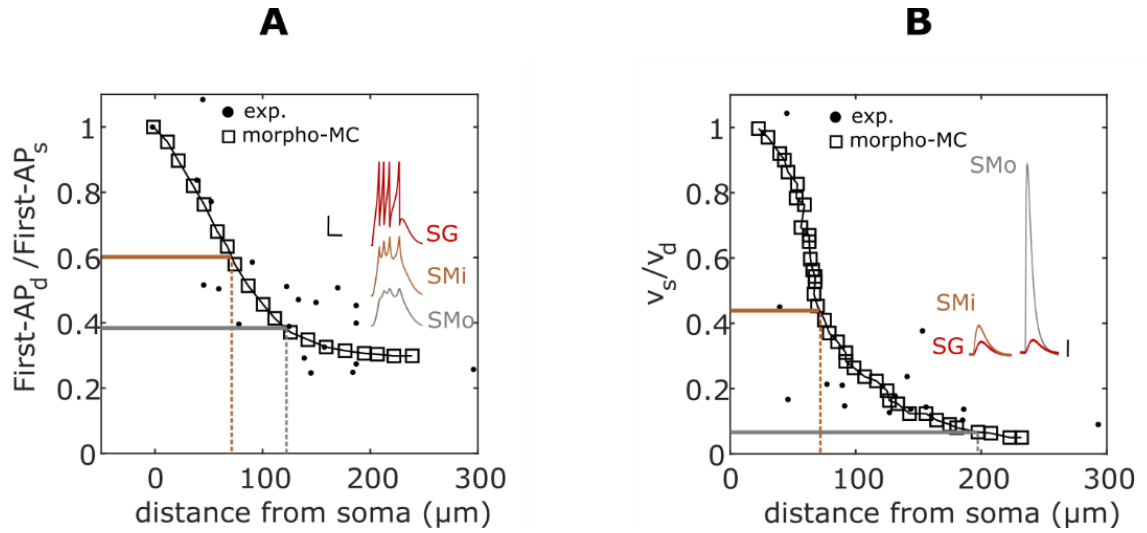
A3 Fig. Dendritic properties of the 3-compartment DG Granule model. Stratum Granulosum (SG), Stratum moleculare-inner (SMi), and Stratum moleculare-outer (SMo) denote the somatic, proximal, and distal dendritic compartments, respectively. (A) Attenuation of first back-propagating action potential (AP) from experimental recordings (exp.), biophysically and morphologically detailed multi-compartment model (morpho-MC) and three-compartment IM. Inset shows compartment responses for somatic current injection. (B) Attenuation of dendritic EPSPs as they propagate towards soma. Inset shows compartment responses for a single synaptic stimulation at SMi and SMo. Experimental and model data were digitized from (Krueppel et al., 2011). Calibrations: 25mV, 20ms (A) and 2mV (B).
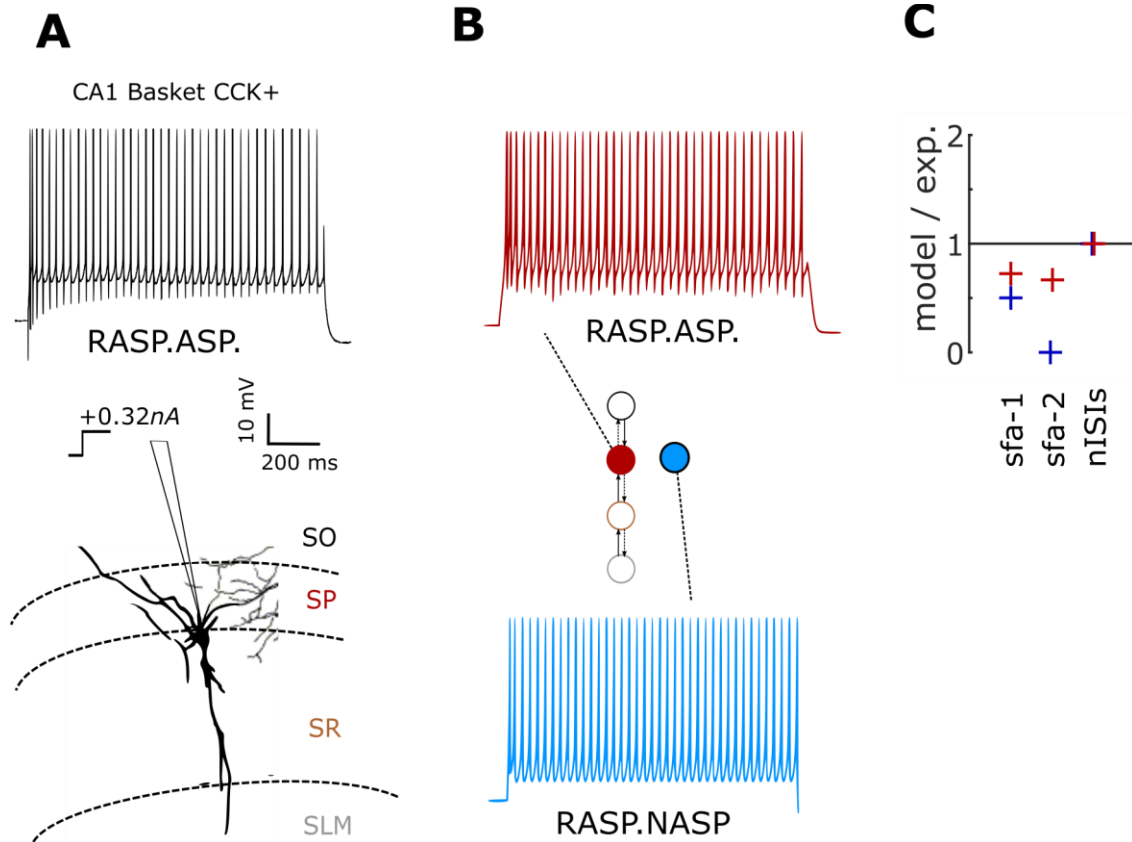
A4 Fig. Additional compartments are necessary to capture the complex transient pattern 'RASP.ASP.'. (A) Experimentally recorded voltage trace from a CA1 Basket CCK+ neuron (Cope et al., 2002) digitized by Hippocampome.org. (B) 4-compartment model reproduces the pattern RASP.ASP. (red), and the single-compartment counterpart failed to do so (blue). (C) While both versions reproduce nISIs accurately, the multi-compartment model more accurately reproduces sfa. Sfa-1 is the rapid frequency adaptation measured in the first three ISIs (RASP.), and sfa-2 is the weak adaptation measured in the remaining 35 ISIs (ASP.) Note that sfa-2=0 in the single-compartment model. Spike amplitudes are truncated.
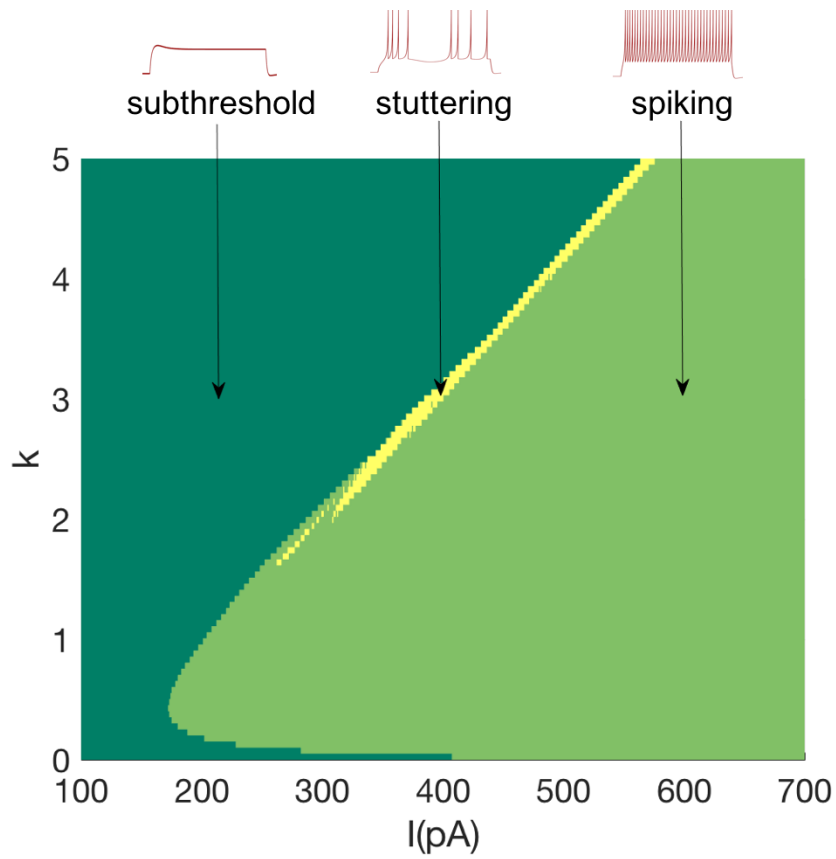
A5 Fig. Parameter 'k' affects the excitability level in the IM. Arrows represent the CA1 Bistratified model (see Fig 2). Model responses were classified by only varying the parameter 'k' and input current 'I' for this plot. As the value of 'k' is increased, higher values of depolarizing current are required to elicit stuttering (yellow) or spiking (light green) patterns. Notice that the stuttering behavior occurs just above the rheobase and is non-existent for 'k'<1.75. It should also be noted that the stuttering region could be wider in a different sub-region of the parameter space.

A1-A Table. Quantitative features of firing patterns

fsl	First Spike Latency
sfa	Spike Frequency Adaptation
ISI	Inter-Spike Interval
nISIs	number of ISIs
pss	Post-Spike Silence
n_bursts	Number of bursts
bw	Burst Width
pbi	Post-Burst Interval
b-nISIs	nISIs within a Burst

A1-B Table. Elements of firing patterns

D	Delayed
ASP	Adapting SPiking
NASP	Non-Adapting SPiking
RASP	Rapidly Adapting SPiking
TSTUT	Transient Stuttering
TSWB	Transient Slow Wave Bursting
PSTUT	Persistent Stuttering
PSWB	Persistent Slow Wave Bursting
SLN	SiLeNce
RBS	ReBoundSpiking

A1-C Table. Other abbreviations

IM	Izhikevich Model
compact-MC	Compact Multi-Compartment model
morpho-MC	Morphologically detailed Multi-Compartment model
EA	Evolutionary Algorithm
SP	Stratum Pyramidale
SR	Stratum Radiatum
SLM	Stratum Lacunosum Moleculare
SO	Stratum Oriens
SG	Stratum Granulosum
SMi	Inner one-third of Stratum Moleculare
SMo	Outer one-third of Stratum Moleculare
H	Hilus

A2 Table. Features and errors for all the traces from Fig 4.1

Neuron type	pattern class	*I (pA)* exp, model	*fsl (ms)* exp, model, model/exp	*sfa* exp, model, model/exp	*nISIs* exp, model, model/exp	*pss (ms)* exp, model, model/exp
DG Total Molecular Layer	-	50, 42	150, 367, **2.45**	-	1, 1, **1***	-
	ASP.	75, 73	64.71, 96, **1.49**	y=0.142x+0.947, y=0.142x+0.975, **1.01**	5, 5, **1**	99.06, 96.96, **0.98**
	ASP.	100, 102	22.25, 64, **2.88**	y=0.114x+0.911, y=0.082x+0.987, **0.90**	9, 9, **1**	52.97, 27.37, **0.52**
	ASP.	200, 205	13.05, 33, **2.53**	y=0.056x+1.073, y=0.032x+1.014, **0.76**	19, 19, **1**	18.67, 17.40, **0.93**
CA1 Basket	NASP	150, 151	175.00, 141, **0.81**	y=0.000x+1.197, y=0.000x+1.197, **1**	2, 2, **1**	210, 210.15, **1**
	NASP	310, 316	4.97, 18.00, **3.62**	y=0.000x+2.080, y=0.000x+1.165, **0.56**	55, 55, **1**	20.90, 0, **0**
CA1 Trilaminar	RBS	-100, -100	770, 810, **1.05**	-	1, 1, **1**	-
	ASP.SLN	25, 23	50.73, 56.00, **1.1**	y=0.720x+1.000, y=0.491x+1.000, **0.84**	2, 2, **1**	541.95, 542.17, **1**

Neuron type	pattern class	I (pA) exp, model	fsl (ms) exp, model, model/exp	sfa exp, model, model/exp	nISIs exp, model, model/exp	pss (ms) exp, model, model/exp
	ASP.	50, 46	14.49, 28, **1.93**	y=0.038x+1.340, y=0.036x+1.006, **0.85**	21, 21, **1**	26.21, 24.59, **0.94**
MEC LV-VI Pyramidal Polymorphic	D.NASP	unknown, 78	292.34, 292, **1**	y=0.000x+1.055, y=0.000x+1.042, **0.99**	5, 5, **1**	40.00, 63.57, **1.59**
	ASP.	200, 197	56.40, 56.00, **0.99**	y=0.036x+1.103, y=0.030x+1.024, **0.88**	18, 18, **1**	23.70, 23.33, **0.98**

*number of spikes is compared for single-spike traces

A3-A Table. Features and errors for all the traces from Fig 4.2 (spiking features)

Neuron type	pattern class	I (pA) exp, model	fsl (ms) exp, model, model/exp	sfa exp, model, model/exp	nISIs exp, model, model/exp	pss (ms) exp, model, model/exp
CA1 Bistratified	PSTUT	400, 408	40.48, 37.00, **0.91**	NA	NA	43.48, 43.75, **1.01**
	ASP.	600, 602	12.38, 16.00, **1.29**	y=0.008x+1.213, y=0.005x+1.187, **0.8**	35, 35, **1**	9.63, 0, **0**
EC LV Deep Pyramidal	TSTUT.NASP	400, 410	16.00, 15.00, **0.94**	NA	NA	164, 126, **0.77**
DG Granule	TSWB.SLN	200, 208	41.81, 13.00,	NA	1, 1, **1**	1904.27, 1902.08,

			0.31			1.0
	TSWB.SLN	400, 404	7.79, 7.00, **0.9**	NA	3, 4, **1.33**	1943.55, 1943.16, **1.0**
DG Hilar Ectopic Granule	TSWB.SLN	unknown, 602	14.34, 17.00, **1.19**	NA	1, 1, **1**	156.16, 129.95, **0.83**
	ASP.	700, 699	9.52, 10, **1.05**	y=0.791x+0.693, y=0.790x+0.683, **0.99**	2, 2, **1**	107.94, 109.29, **1.01**

A3-B Table. Features and errors for all the traces from Fig 4.2 (bursting/stuttering features)

Neuron type	pattern class	*I (pA)* exp, model	*n_bursts* exp, model, model/exp	*bw* (ms)* exp, model, model/exp	*pbi* (ms)* exp, model, model/exp	*b-nISIs** exp, model, model/exp
CA1 Bistratified	PSTUT	400, 408	2, 2, **1**	83, 70 56, 69, **1.04**	154, 154**, 1**	3, 3, 2, 2, **1**
EC LV Deep Pyramidal	TSTUT.NASP	400, 410	2, 2, **1**	88, 38 3752, 3654, **0.7**	276, 365**, 1.32**	2, 2, 16, 19, **1.09**

*features are reported for each burst in a pattern

A4-A Table. Features and errors for all the traces from fig 4.3 (spiking features)

Neuron type	pattern class	*I (pA)* exp, model	*fsl (ms)* exp, model, model/exp	*sfa* exp, model, model/exp	*nISIs* exp, model, model/exp	*pss (ms)* exp, model, model/exp
CA1 Perforant Path Associated	ASP.SLN	700, 708	0.16, 12, **75**	y=0.142x+0.915, y=0.115x+0.852, **0.875**	12, 12, **1**	59.55, 59.10, **0.99**
DG MOLAX	PSTUT	400, 397	15.30, 43, **2.81**	NA	NA	56.90, 0, **0**
MEC LIII Multipolar	RBS	-200, 193	625, 625, **1**	NA	1, 1, **1**	NA
	NASP	250, 243	4.05, 8, **1.98**	y=0.000x+1.310, y=0.000x+1.401, **1.06**	53, 53, **1**	7.37, 0, **0**
DG AIPRIM	ASP.NASP	200, 209	0.45, 14, **31.11**	y1=0.031x1+1.268, y1=0.040x1+1.011; y2=0.000x2+3.576, y2=0.000x2+3.567, **1.02**	33, 33, **1**; 24, 24, **1**	1.24, 13.26, **10.7**
CA1 Pyramidal	ASP.	150, 154	29.16, 89, **3.05**	y=0.085x+1.140, y=0.078x+1.137, **0.96**	11, 11, **1**	120.79, 72.12, **0.6**

A4-B Table. Features and errors for all the traces from fig 4.3 (bursting/stuttering features)

Neuron type	pattern class	*I (pA)* exp, model	*n_bursts* exp, model, model/exp	*bw* (ms)* exp, model, model/exp	*pbi* (ms)* exp, model, model/exp	*b-nISIs* exp, model, model/exp
DG MOLAX	PSTUT	400, 397	7, 6, **0.86**	39.90, 45; 0, 39; 47.8, 28; 0, 38; 23.4, 29; 24.5, 0, **0.49**	34, 67; 39.2, 95; 66, 65; 62.8, 88; 64.9, 72; 74.4, 0, **1.32**	4, 3; 1, 2; 3, 2; 1, 2; 2, 2; 2, 1, **1.15**

*features are reported for each burst in a pattern

143

A

B

C

144

A6 Fig. Transforming discrete spike times into a continuous signal capturing bursting cycles. A. Activity patterns of a sample neuron for a duration of one second, which show the existence of periodic bursting in NC (top) and ND (middle) and periodic spiking in NS (bottom). B. Probability density estimates of interspike intervals from all the neurons. The sum of all the local maxima (triangles) are 97, 139 and 37 respectively for NC (top), ND (middle), and NS (bottom). C. Lowpass filtering of spikes to extract bursting cycles using Gaussian convolution. The length of the Gaussian window is equal to the duration of one full cycle of a burst (NC and ND) or a spike (NS), which was estimated from B. This is done so that any frequency higher than that of the burst frequency is filtered in NC and ND.
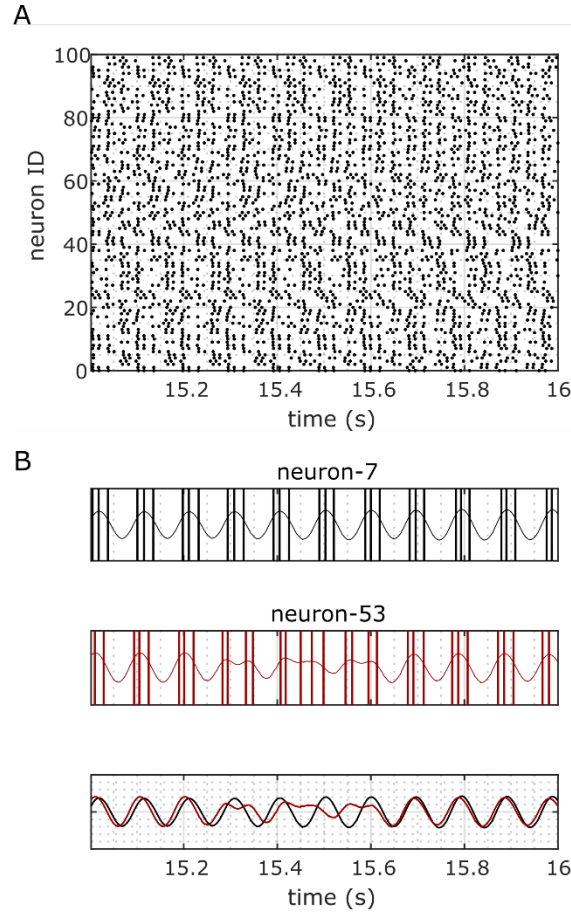
A7 Fig. An example of an unsuccessful transition. Neuron-53 was attracted back to a relative phase near 0 radians after losing stability from the same with respect to neuron-7.
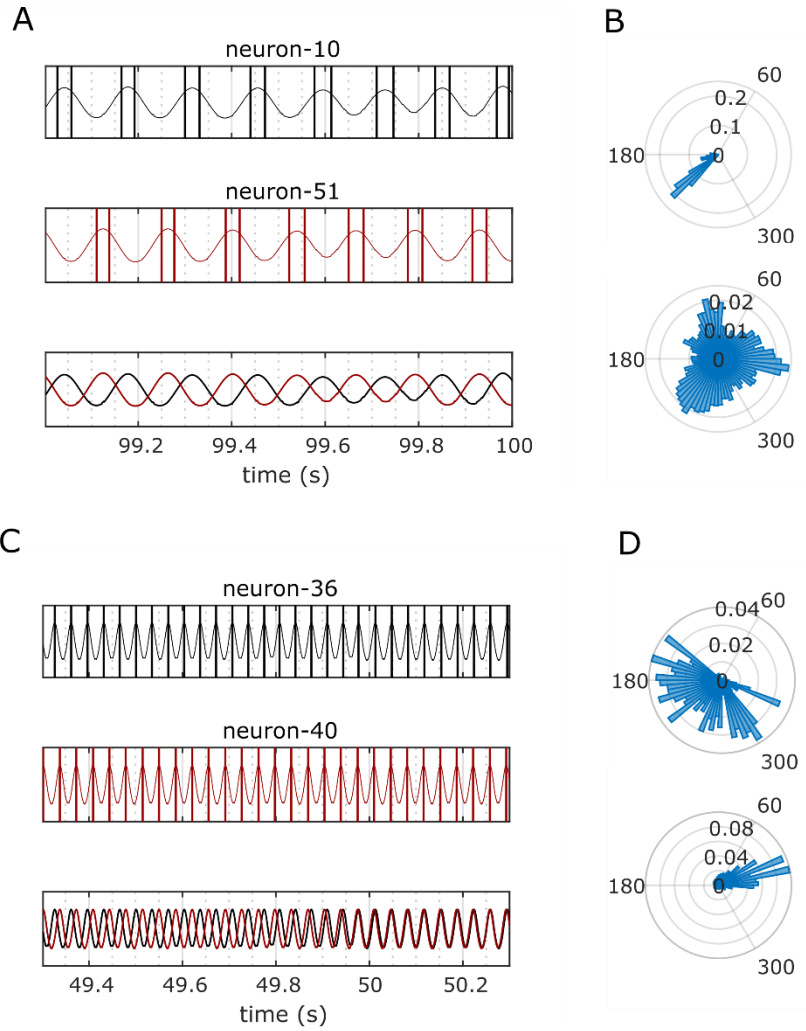
A8 Fig. Phase-locked modes in ND and NS. A&C. Discrete spike times of two neurons are transformed into continuous signals corresponding to burst cycles for ND (A) and spike cycles for NS (C). B. The neuron pair in A shows a locked mode at $4\pi/3$ radians for 1 second (top) and its distribution for 115 second duration is shown in bottom. D. The neuron pair in C shows scattered phase differences for the first 500ms (top), but overall it shows a preferred locked mode near zero radian for 115 second duration (bottom).

Quantitative firing pattern phenotyping of hippocampal neuron types[⊥]

Abstract

Systematically organizing the anatomical, molecular, and physiological properties

of cortical neurons is important for understanding their computational functions.

Hippocampome.org defines 122 neuron types in the rodent hippocampal formation based

on their somatic, axonal, and dendritic locations, putative excitatory/inhibitory outputs,

molecular marker expression, and biophysical properties. We augmented the

electrophysiological data of this knowledge base by collecting, quantifying, and

analyzing the firing responses to depolarizing current injections for every hippocampal

neuron type from published experiments. We designed and implemented objective

protocols to classify firing patterns based on 5 transients (delay, adapting spiking, rapidly

adapting spiking, transient stuttering, and transient slow-wave bursting) and 4 steady

states (non-adapting spiking, persistent stuttering, persistent slow-wave bursting, and

silence). This automated approach revealed 9 unique (plus one spurious) families of

firing pattern phenotypes while distinguishing potential new neuronal subtypes. Novel

statistical associations emerged between firing responses and other electrophysiological

properties, morphological features, and molecular marker expression. The firing pattern parameters, experimental conditions, spike times, references to the original empirical evidences, and analysis scripts are released open-source through Hippocampome.org for all neuron types, greatly enhancing the existing search and browse capabilities. This information, collated online in human- and machine-accessible form, will help design and interpret both experiments and model simulations.

Introduction

Quantitative characterization of neurons is essential for understanding the functions of neuronal networks at different hierarchical levels. The hippocampus provides an excellent test-bed for this exploration as it is one of the most intensively studied parts of the mammalian brain, and is involved in critical functions including learning (Rudy and Sutherland, 1989, 1995), memory (Eichenbaum et al., 1992; Eichenbaum, 2000, 2017), spatial navigation (Hafting et al., 2005; O'Keefe, J. and Dostrovsky, 1971), and emotional associations (Buchanan, 2007).

Transmission of information between neurons is carried out by sequences of spikes, and firing rates are commonly believed to represent the intensity of input stimuli. Since the first discovery in sensory neurons (Adrian and Zotterman, 1926), this principle was generalized and extended to neurons from different brain regions, including the hippocampus (McNaughton et al., 1983). However, it was also found that the firing rate of certain neurons is not constant over time, even if the stimulus is permanently applied. One form of such time-dependent responses is spike frequency adaptation, manifested in a decrease of firing rate (Adrian and Zotterman, 1926). Neurons can produce diverse

148

firing patterns in response to similar stimuli due to the inhomogeneity in their intrinsic properties (Connors and Gutnick, 1990). Both firing rates and temporal firing patterns have long been recognized to play important roles in neural information coding (Ferster and Spruston, 1995).

In electrophysiological experiments *in vitro*, hippocampal neurons demonstrate a vast diversity of firing patterns in response to depolarizing current injections. These patterns are referred to by many names, including delayed, adapting, accommodating, interrupted spiking, stuttering, and bursting (Canto and Witter, 2012; Hemond et al., 2008; Lübke et al., 1998; Mercer et al., 2007; Pawelzik et al., 2002; Tricoire et al., 2011). Uncertainties and ambiguities in classification and naming of neuronal firing patterns are similar to other widely spread terminological inconsistencies in the neuroscience literature, posing obstacles to effective communication within and across fields (Hamilton et al., 2017).

Recent efforts aimed to classify firing patterns for identifying distinct electrical types of cortical neurons (Markram et al., 2004; Markram et al., 2015; Ascoli et al., 2008; Druckmann et al., 2013). Notably, statistical analysis of a large set of electrical features of neocortical interneurons with different firing patterns from a single lab yielded a refinement of the physiological component of the Petilla Nomenclature (Druckmann et al., 2013). However, comparisons across labs and experimental studies are typically limited to qualitative assessments of the illustrated firing traces or subjectively intuitive criteria. Moreover, firing pattern data are seldom unambiguously linked to neuron types independently defined by morphological and molecular criteria.

The Hippocampome.org knowledge base defines neuron types based on the locations of their axons, dendrites, and somata across 26 parcels of the rodent hippocampal formation, putative excitatory/inhibitory output, synaptic selectivity, and major and aligned differences in molecular marker expressions and biophysical properties (Wheeler et al., 2015). Version 1.3 of Hippocampome.org identifies 122 neuron types in 6 major areas: 18 in dentate gyrus (DG), 25 in CA3, 5 in CA2, 40 in CA1, 3 in subiculum (SUB), and 31 in entorhinal cortex (EC). The core assumption of this identification scheme is that neurons with qualitatively different axonal or dendritic patterns, or with multiple substantial differences in other dimensions, belong to different types. For the majority of neuron types, Hippocampome.org reports 10 basic biophysical parameters that numerically characterize passive and spike properties (hippocampome.org/ephys-defs), consistent with other literature-based neuroinformatics efforts (Tripathy et al., 2015).

Here, we developed an objective numerical protocol to automatically classify published electrophysiological recordings of somatic spiking activity for morphologically identified hippocampal neurons from Hippocampome.org. This process revealed specific firing-pattern phenotypes, potential neuronal subtypes, and statistical associations between firing responses and other properties. Inclusion of the classified firing patterns and their quantitative parameters, along with a comprehensive tabulation of the underlying experimental conditions, substantially extends the online search and browse functionalities of Hippocampome.org, providing a wealth of annotated data for quantitative analysis and modeling.

Methods

Data collection, extraction and digitization

The firing patterns of hippocampal neurons were classified based on their spiking responses to supra-threshold step-current pulses of different amplitude and duration as reported in peer-reviewed publications. Firing pattern parameters were extracted from electronic figures using Plot Digitizer (plotdigitizer.sourceforge.net) for all Hippocampome.org neuron types (Wheeler et al., 2015) for which they were available (90 out of 122). A total of 247 traces were analyzed. We extracted values of first spike latency (i.e. delay), inter-spike intervals (ISIs), and post-firing silence (in ms), as well as slow-wave amplitude (in mV) for burst firing recording. For firing pattern identification and analysis, ISIs in each recording were normalized to the shortest inter-spike interval (ISI_{min}) within that time series, to allow meaningful comparison.

All analyzed recordings were obtained in normal artificial cerebrospinal fluids (ACSF) from rodents (rats 85%, mice 12%, and guinea pigs 3%) generally described as "young adults" (ages ranging from 11 to 70 days for rats and from 10 to 56 days for mice). All firing traces considered in this report were recorded in slice preparations; 74% of electrophysiological traces were obtained using whole-cell patch clamp and 26% intracellular recording with sharp microelectrodes. All experimental conditions and solution compositions were extracted and stored with every recording and are available at Hippocampome.org as specified in the "Web portal" section below.

Firing pattern classification

Hippocampal neuron types display a variety of firing pattern elements in both their transient and steady state responses to continuous stimulation (A9 Fig.). Specifically, transients (which we label by dot-notation) can be visually differentiated into delay (D.), adapting spiking (ASP.), rapidly adapting spiking (RASP.), transient stuttering (TSTUT.), and transient slow-wave bursting (TSWB.). Steady states include silence (SLN), non-adapting spiking (NASP), persistent stuttering (PSTUT), and persistent slow-wave bursting (PSWB).

	Transient	Steady-state
SiLeNce	**Delay (D.)** — DG Mossy	**Steady-state SiLeNce (SLN)** — CA2 SP-SR
SPiking	**Adapting SPiking (ASP.)** — CA1 Radiatum $ISI_1 < ISI_2 ... < ISI_n$; **Rapidly Adapting SPiking (RASP.)** — CA1 Radiatum $ISI_1 << ISI_2 << ISI_3$	**Non-Adapting SPiking (NASP)** — DG HICAP $ISI_1 = ISI_2 = ... ISI_n$
STUTering	**Transient STUTering (TSTUT.)** — EC LV Deep Pyramidal $ISI_2 < ISI_3 > ISI_4$	**Persistent STUTering (PSTUT)** — CA1 Neurogliaform Projecting $ISI_4 < ISI_5 >> ISI_6$; ISI_{max}
Bursting	**Transient Slow-Wave Bursting (TSWB.)** — CA3 Pyramidal; sDW; sAHP; PFS	**Persistent Slow-Wave Bursting (PSWB)** — CA1 Pyramidal $ISI_2 << ISI_3 >> ISI_4$; sDW; sAHP; ISI_{max}

A9 Fig. Firing pattern elements observable in hippocampal neurons in vitro. ISI - inter-spike interval, PFS – post firing silence, sDW – slow depolarization wave, sAHP – slow after-hyperpolarization. Original data extracted from Lübke et al., 1998 (D), Vida et al., 1998 (ASP), Pawelzik et al., 2002 (RASP), Hamam et al., 2002 (TSTUT), Chevaleyre and Seigelbaum, 2010 (TSWB), Mercer et al., 2012 (SLN), Mott et al., 1997 (NASP), Fuentealba et al., 2010 (PSTUT), and Golomb et al., 2006 (PSWB, spontaneous bursting in Ca2+-free ACSF).

In certain cases, a constant current injection elicits firing patterns consisting of single firing pattern elements (NASP, PSTUT or PSWB). In other cases, complex firing patterns are observed as sequences of two or more firing pattern elements, such as delayed non-adapting spiking (D.NASP), silence preceded by adapting spiking (ASP.SLN), and non-adapting spiking preceded by delayed transient slow-wave bursting (D.TSWB.NASP). Experimental recordings without identifiable steady states were deemed uncompleted firing patterns (e.g. ASP., D.ASP., or RASP.ASP.).

In order to define the firing pattern elements unambiguously, we developed a set of quantitative classification criteria (Table 1). The transient response was classified as delayed (D.) if the latency to the first spike was longer than the sum of the first two inter-spike intervals (ISI_1 and ISI_2). Similarly, post-firing silence (PFS) was considered to be a steady state (SLN) if it exceeded the sum of the last two inter-spike intervals (ISI_{n-1} and ISI_n). In addition, post-firing silence had to last at least twice the longest inter-spike interval (ISI_{max}).

A persistent firing response with relatively equal inter-spike intervals denotes non-adapting spiking (NASP); in contrast, transients with a progressive increase or decrease of ISIs can be classified as adapting or accelerating spiking, respectively. To discriminate among several possible combinations of these firing patterns objectively and reproducibly, we devised a minimum information description criterion by comparing

154

piecewise (segmented) linear regression models of increasing complexity. Specifically,

non-adapting spiking (NASP) can be described by a single parameter, namely the

(average) firing rate ($Y=c$). Similarly, fitting normalized inter-spike intervals versus

normalized time with a (2-parameter) linear function $Y=aX+b$ (with $a>0$) corresponds to

adapting spiking (ASP.). Fitting data with a piecewise linear function

$$Y = \begin{cases} a_1 X + b_1 & if \ X < \dfrac{b_2 - b_1}{a_1 - a_2} \\[2em] a_2 X + b_2 & if \ X \geq \dfrac{b_2 - b_1}{a_1 - a_2} \end{cases}$$

corresponds to adapting-non-adapting spiking (ASP.NASP) when $a_1>0$ and $a_2=0$

(3 parameters), and to adapting-adapting spiking with different adaptation rates

(ASP.ASP.) when both $a_1>0$ and $a_2>0$ (4 parameters). We only selected a model with

more parameters if the fit relative to a less complex model improved in a statistically

significant way. The significance threshold for the differences between one-parameter

fitting (NASP) and two-parameter linear-regression fitting (ASP.) was conventionally set

at 0.05. Furthermore, in order to avoid identifying very weak adaptations as ASP., a

minimum threshold of 0.003 was used for the slope a_1.

A5 Table. Principles of classification of firing pattern elements

Firing pattern element	Transient responses	Steady-state responses	Characteristics of responses	Values of parameters
Silence	Delayed (D.)		$Delay > DF \dfrac{ISI_1 + ISI_2}{2}$	$DF=2$
		SiLeNce (SLN)	$PFS > SF \dfrac{ISI_n + ISI_{n-1}}{2}$ $PFS > SF * ISI_{max}$	$SF=2$
Spiking	Adapting Spiking (ASP.)		$ISI_1 < ISI_2 < ISI_n$; to compare 2 parameter fit $(Y=a_1X+b_1)$ and 3 parameter fit $(Y=a_1X+b_1; Y= b_2)$	$p_{2,1}<0.05$ $p_{3,2}>0.025$ $a_1 > 0.003$
	Rapidly Adapting Spiking (RASP.)		$ISI_1 << ISI_2 << ISI_3$ $Y = a_1X + b_1$ $a_1 > S_{RASP}$	$S_{RASP} = 0.2$
		Non-Adapting Spiking (NASP)	$ISI_1 \approx ISI_2 \ldots \approx ISI_n$; to compare 1 parameter fit $(Y=b_1)$ and 2 parameter fit $(Y=a_1X+b_1)$	$p_{2,1}>0.05$

Interrupted	Stuttering	Transient STUTering (TSTUT.)		$ISI_i > F_{pre} * ISI_{i-1}$ $ISI_i > F_{post} * ISI_{i+1}$ $\dfrac{\sum_{j=i}^{n} ISI_j}{n-j} > F_{pre} \dfrac{\sum_{j=1}^{i-1} ISI_j}{j}$ $\forall j < i-1 : \dfrac{1}{ISI_j} > f_{min}$ (T1.1)	F_{pre}=2.5 F_{post}=1.5 f_{min}= 25 Hz i=2,3,4
			Persistent STUTering (PSTUT)	$\dfrac{ISI_i^{max}}{ISI_{i-1}} + \dfrac{ISI_i^{max}}{ISI_{i+1}} > F_{PSTUT}$	F_{PSTUT}=5
	Slow-Wave Bursting	Transient Slow-Wave Bursting (TSWB.)		Inequalities T1.1, $SWA > SWA_{min}$	F_{pre}=2.5 F_{post}=1.5 f_{min}=25 Hz i=2,3,4 SWA_{min}=5 mV
			Persistent Slow-Wave Bursting (PSWB)	$\dfrac{ISI_i^{max}}{ISI_{i-1}} + \dfrac{ISI_i^{max}}{ISI_{i+1}} > F_{PSWB}$ $SWA > SWA_{min}$	F_{PSWB}=5 SWA_{min}=5 mV

For each subsequent stage of comparison, we used Bonferroni-corrected *p*-values. Specifically, in order for a pattern with an adapting spiking transient (i.e. ASP.) to be qualified as ASP.NASP, the *p*-value must be less than 0.025. Similarly, the *p*-value for the differences between three-parameter piecewise-linear-regression fitting (ASP.NASP) and four-parameter piecewise-linear-regression fitting (ASP.ASP.) must be less than 0.016. Supplementary Fig. S1 shows examples of fitting spiking activity with linear regression and piecewise linear regression models. If adaptation was only observed in the first two or three ISIs in a longer train of spikes, and if the linear fitting of slope a_1 exceeded 0.2, then this transient was classified as rapidly adapting spiking (RASP.) (see Fig.1; Pawelzik et al., 2002). For accelerating spiking (ACSP.), the linear fitting slope must be negative.

We defined transient stuttering (TSTUT.) as a short high-frequency (>25 Hz) cluster of action potentials (APs) followed by other distinctive activity. In addition, the first ISI after a TSTUT cluster must be 2.5 times longer than the last ISI of the cluster and 1.5 times longer than the next ISI (see A9 Fig.; Hamam et al., 2000). Under transient slow-wave bursting activity (TSWB.), a cluster of two or more spikes rides on a slow depolarization wave (>5mV) followed by a strong slow after-hyperpolarization (AHP) (see A9 Fig.; Chevaleyre and Siegelbaum, 2010). Persistent stuttering (PSTUT) was classified as firing activity with high-frequency clusters of APs separated by long silence intervals, moreover, the sum of its ratios to the preceding ISI and the following ISI is more than 5 (see A9 Fig.; Fuentealba et al., 2010; Price et al., 2005). Similarly, under

persistent slow-wave bursting (PSWB) activity, these clusters of two or more tightly grouped spikes ride on slow depolarizing waves (>5 mV) followed by strong, slow AHPs (Golomb et al., 2006; Bilkey et al., 1990). The amplitude of the slow wave was determined as the difference between the threshold of initiation of the slow wave and the threshold of generation of the action potential at the top of the slow wave. Threshold level was defined as a point of fast rising of the membrane voltage (for slow wave initiation and action potential generation dV/dt should exceed 0.15V s^{-1} and 20 V s^{-1}, respectively). As exemplified above, the choices of firing-pattern identification parameters were consistent with literature reports of experimental results with similar activities.

Based on the aforementioned methods, we implemented a firing-pattern classification algorithm using the values of ISIs, delay, post-firing silence, and slow-wave amplitude as input data (for algorithmic details, see Supplementary Fig. S2).

Statistical analysis

We explored pairwise correlations between 24 observed firing patterns, 9 firing pattern elements, and 212 other properties of Hippocampome.org neuron types, including: primary neurotransmitter, 103 morphological properties (axonal, dendritic, and somatic locations in the 6 sub-regions and 26 parcels of the hippocampal formation; the projecting (between sub-regions) or local (within sub-regions) nature of axonal and dendritic patterns; axon and dendrite co-presence within any parcel; axonal and dendritic presence in a single layer only (intra-laminar) or in ≥3 layers (trans-laminar)), clear positive or negative expression of 98 molecular markers; high (top third) or low (bottom

159

third) values for 10 electrophysiological properties. To evaluate the correlations between these categorical properties, we used 2×2 contingency matrices with Barnard's exact test (Barnard, 1947), which provides the greatest statistical power when row and column totals are free to vary (Lydersen, 2009). A total of 6,996 correlations were analyzed. The results satisfying a p-value cutoff of <0.05 and a false discovery rate (FDR) <0.25 (Benjamini and Hochberg, 1995) were considered as statistically significant. The correlation analysis was implemented in MATLAB (MathWorks, Inc.).

We analyzed numerical electrophysiological data, such as the relationship between the width of an action potential and the minimum ISI using linear regression and histograms. Spike duration was measured as the width at half-maximal amplitude, as is most commonly defined[36]. Minimum inter-spike intervals (ISI_{min}) were measured from the figures or extracted directly from tables or textual excerpts of the corresponding papers.

For cluster analysis of weighted categorical firing pattern data, we assigned weights to firing pattern elements according to the formula $W_e=(N-n_e)/N$, where W_e is the weight of the element e, n_e is the number of cell types expressing firing pattern(s) with element e, N is the total number of cell types/subtypes, and $e=\{$ASP., D., RASP., NASP, PSTUT, PSWB, SLN, TSUT., TSWB.$\}$. We employed a two-step cluster analysis using the IBM SPSS Statistics 24 software. Silhouette measures of cohesion and separation greater than 0.5 indicated that the elements were well matched to their own clusters and poorly matched to neighboring clusters, and that the clustering configuration was appropriate.

Statistical data were expressed as mean ± standard deviation.

Web portal and database representation of firing patterns and experimental conditions

Hippocampome.org provides access to morphological, molecular, electrophysiological, and connectivity information for 122 neuron types. The firing pattern data newly added and made freely available for download with this work include recording illustrations, the duration and amplitude of stimulation, digitized ISIs and firing pattern parameters (as comma-separated-value files), the complete solution compositions of the ACSF and of the micropipettes or patch pipettes, and the result of the firing pattern classification algorithm detailed above. Additional metadata is collected and displayed for all electrophysiological evidence in Hippocampome.org including the animal species (rat vs. mouse) and other details regarding the subject (inbred strain, age, sex, and weight, if reported), slice thickness and orientation, recording methods (intracellular microelectrode or variations of patch clamp), and temperature. Details of the implementation of the portal are presented in the Supplemental Information.

Results

From firing patterns to firing pattern phenotypes

Version 1.3 of Hippocampome.org contains suitable electrophysiological recordings for 90 of the 122 morphologically identified neuron types. Applying the firing pattern identification algorithm to these digitized data resulted in the detection of 23 different firing patterns. A given neuron type may demonstrate distinct firing patterns in

response to different stimuli or conditions. The set of firing patterns exhibited by a given neuron type forms its firing pattern phenotype.

The simplest case consists of those neuron types that systematically demonstrate the same firing pattern independent of experimental conditions or stimulation intensity. These neuron types may still display quantitatively different responses to stimuli of various amplitudes (typically increasing their firing frequency upon increasing stimulation), but their qualitative firing patterns remain the same. We identified 37 such "individual/simple-behavior types" in Hippocampome.org, as exemplified by DG Basket cells with their NASP phenotype (Savanthrapadian et al., 2014).

In contrast to the above scenario, certain neuron types exhibit qualitatively distinct firing patterns in response to different amplitudes of stimulation. We identified 20 such "multi-behavior" types; for instance, medial EC Layer V-VI Pyramidal-Polymorphic cells demonstrate delayed non-adapting and adapting spiking (Canto and Witter, 2012), or CA1 Neurogliaform projecting cells (Price et al., 2005) display adapting spiking and persistent stuttering at different stimulus intensities. The firing phenotypes of these neurons thus consist of the combinations of two firing patterns.

In a different set of cases, subsets of neurons from the same morphologically identified type display distinct firing patterns under the same experimental conditions (typically from the same study) in response to identical stimulation. These neuron types can thus be divided into electrophysiological subtypes. For example, of the CA3 Spiny Lucidum interneurons, some are adapting spikers whereas others are persistent stutterers (Szabadics et al., 2009). In certain neuron types, one or more of the subtypes could also

display multiple behaviors at different stimulation intensities. For instance, a subset of entorhinal Layer III Pyramidal neurons consists of non-adapting spikers and another subset switches from ASP.NASP at rheobase to RASP.ASP. at higher stimuli (Canto and Witter, 2012). Of the 90 neuron types with firing patterns in Hippocampome.org, 22 could be divided into 52 electrophysiological subtypes. Notably, these included the principal neurons of most sub-regions of the hippocampal formation: CA3, CA1, and subiculum Pyramidal cells, entorhinal Spiny Stellate cells, but also several GABAergic interneurons such as dentate Total Molecular Layer (TML) cells (Mott et al., 1997). Specifically, 8 neuron types yielded 18 subtypes exclusively demonstrating single behaviors; for 11 neuron types, at least one of the subtypes exhibited multi-behaviors, resulting in 13 multi-behavior subtypes and 13 additional single-behavior subtypes.

This meta-analysis is complicated by the variety of experimental conditions used in the published literature from which the electrophysiological data were extracted. Several differences in materials and methods could affect firing patterns above and beyond common species (rats vs. mice) or recording (patch clamp vs. microelectrode). For example, 30% of experimental traces were recorded from transverse slices, 24% from horizontal, 8% coronal, 29% mixed (e.g. "horizontal or semicoronal"), and 9% other directions (e.g. custom angles). Furthermore, pipettes were filled with potassium gluconate in 69% of cases, with potassium methylsulfate in 22%, and with potassium acetate in 9% (see e.g. Supplementary Table S2). While these different experimental conditions can affect membrane biophysics substantially (Tebaykin et al., 2018) and often quantitatively influence neuronal firing (e.g. changing the spiking frequency),

occasionally they can also cause a qualitative switch between distinct firing patterns. A striking case is that of rat DG Granule cells, which have demonstrated transient slow-wave burst followed by silence in whole-cell recordings of horizontal slices from Sprague-Dawley animals (Williams et al., 2007); delayed non-adapting spiking in whole-cell recording of transverse slices from Wistar animals (Lübke et al., 1998); or adapting spiking in intracellular recording of horizontal slices from Wistar animals (Han et al., 1993). Because the different firing patterns could be caused by the differences in experimental methods, we annotate a possible "condition-dependence," but cannot conclusively categorize these cells as multi-behavior or subtypes. Most of the condition-dependent behaviors could be attributed at least in part to the occasional use of microelectrode instead of patch-clamp (now considered the preferred recording method) or the animal species as in the case of CA1 Horizontal Basket cells, which display adapting and non-adapting firing in rats and mice, respectively (Tricoire et al., 2011; Zemankovics et al., 2010).

Condition dependence can alter the firing patterns not only in cell types with single behaviors, such as MOPP cells (Han et al., 1993; Armstrong et al., 2011), but also in multi-behavior neuron types, such as CA1 Axo-axonic cells (Pawelzik et al., 2002; Buhl et al., 1994). These cases account for 6 and 5 Hippocampome.org neuron types, respectively. Lastly, condition dependence may also be found in specific electrophysiological subtypes, whether they display single behaviors, such as CA1 Pyramidal neurons (Chevaleyre and Siegelbaum, 2010; Zemankovics et al., 2010; Kirson and Yaari, 2000; Staff et al., 2000) or multi-behavior, such as entorhinal Layer V Deep

Pyramidal neurons (Canto and Witter, 2012; Hamam et al., 2000, 2002). These cases respectively account for 2 and 1 Hippocampome.org neuron types, in turn giving rise to 6 condition-dependent subtypes with single behaviors and 2 condition-dependent subtypes with multi-behavior. In general, types/subtypes with firing pattern recorded under diverse experimental conditions constitute only 16 percent of the total number of types/subtypes with available recordings.

Figure 2 presents the full firing-pattern phenotypes of all 90 Hippocampome.org neurons, with available data in form of separate matrices for the 68 individual neuron types (A10 Fig.a) and the 52 subtypes divided from the remaining 22 types (A10 Fig.b). In both cases the simple behaviors constitute larger proportions than multi-behavior, with condition dependence only reported for a minority of types and subtypes (A10 Fig.c). Across these neuron types/subtypes, 44 distinct phenotypes can be identified as unique combinations of firing patterns, excluding those that differ from others only by the absence of a detectable stable state in one of the firing patterns (like ASP. versus ASP.NASP or ASP.SLN). An interactive online version of these matrices is available at hippocampome.org/php/firing_patterns.
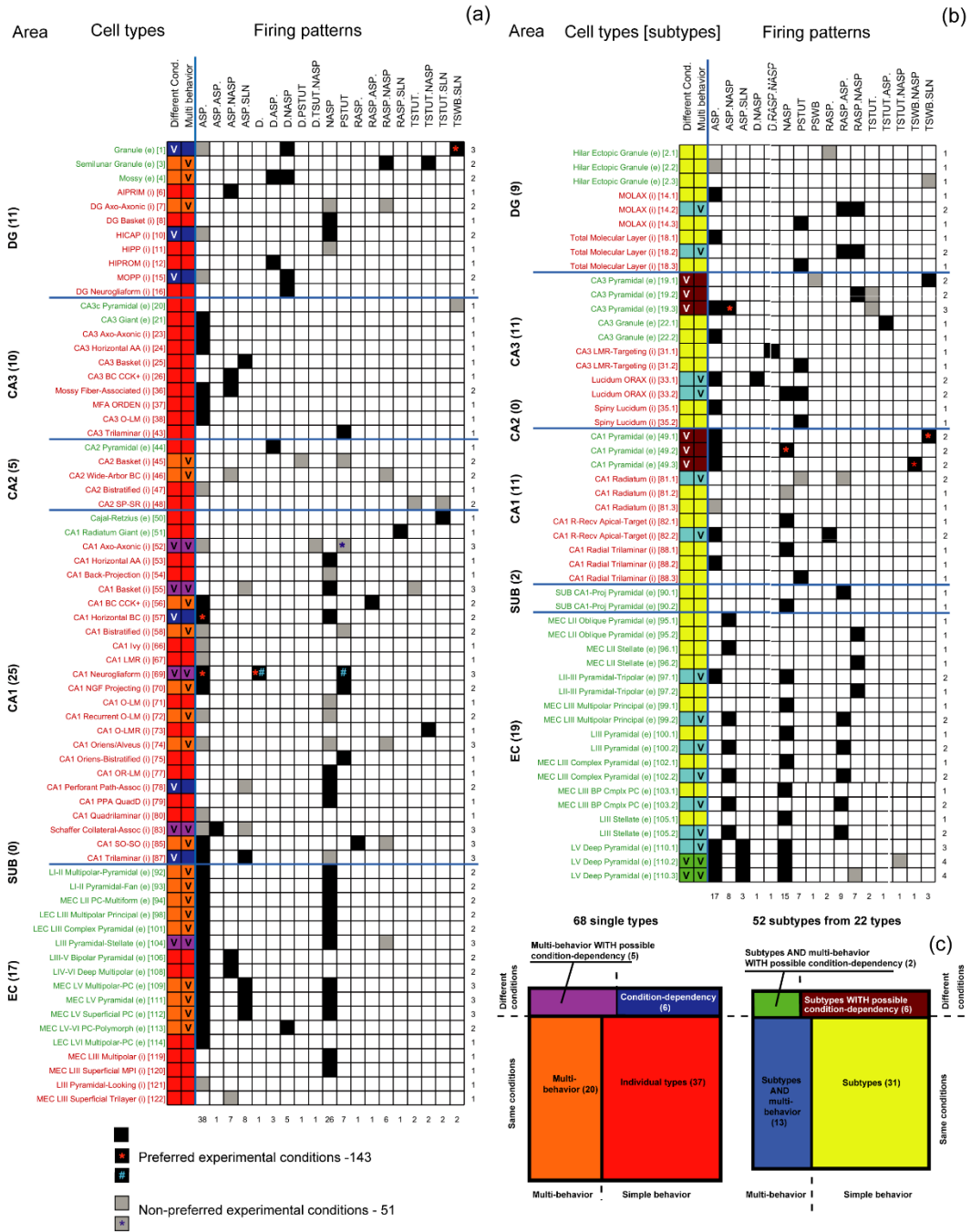
A10 Fig. Identified firing patterns and firing pattern phenotypes complexity of neuron types (a) and subtypes (b). Online matrix: hippocampome.org/firing_patterns. Green and red cell type/subtype names denote excitatory (e) and inhibitory (i) neurons, respectively. FPP is firing pattern phenotype. The numbers in the brackets correspond to the order in which the cell types were presented in the Hippocampome (ver. 1.3). The orange asterisk denotes different

experimental conditions. (c) Complexity of firing pattern phenotypes; percentages and ratios indicate occurrences of phenotypes of different complexity among 120 cell types/subtypes.

Dissecting firing patterns into firing pattern elements across neuron types

Firing patterns and firing pattern elements are also diverse with respect to their relative frequency of occurrence among hippocampal neuron types. Firing patterns can be grouped based on the number of elements comprising them, namely single (e.g., NASP or PSTUT), double (e.g. ASP.NASP or TSWB.SLN), and triple (D.RASP.NASP and D.TSWB.NASP) or based on whether they are completed (ASP.NASP, TSWB.SLN) or uncompleted, as in ASP., RASP.ASP., and TSTUT.ASP. (A11 Fig.a). Of the nine firing pattern elements, the most frequent are ASP and NASP, while the least common are TSTUT, TSWB, and PSWB (A11 Fig.b). Notably, accelerated spiking (ACSP) has not been reported in the rodent hippocampus although it is commonly observed in other neural systems, such as turtle ventral horn interneurons (Smith and Perrier, 2006) and motoneurons (Leroy et al., 2014).

The relationships between sets of firing pattern elements observed in hippocampal neuron types can be summarized in a Venn diagram with firing pattern elements represented as ellipses and the intersections thereof corresponding to complex firing patterns (A11 Fig.c). This analysis highlights the following features: the four main firing transients (ASP., RASP., TSTUT., TSWB.) often end either with NASP or with SLN; ASP. is often preceded by RASP. and occasionally by TSTUT.; interrupted steady-state firings (PSTUT and PSWB) stand out as a separate group; and delay (D.) most often

167

precedes NASP. Fifteen of possible 38 completed firing patterns were discovered in the literature for morphologically identified hippocampal neuron types.
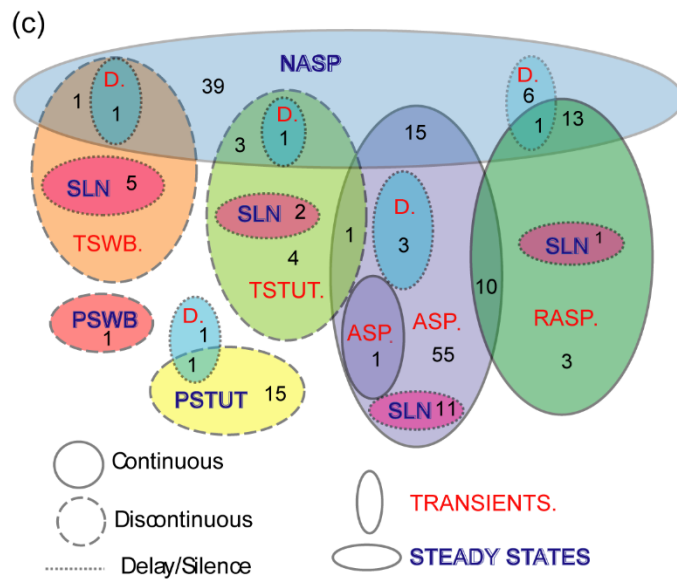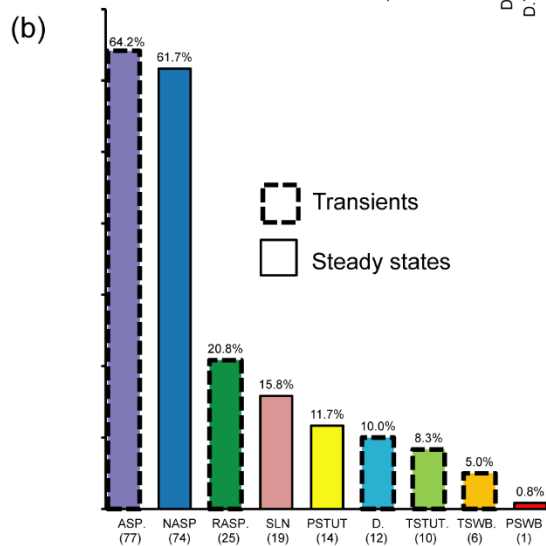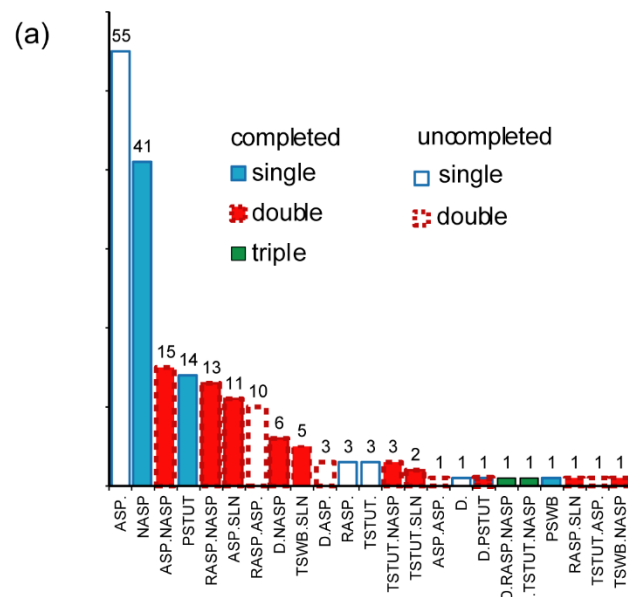
(a)

(b)

(c)

Classification and distribution of firing pattern phenotypes

In order to classify the 44 unique firing pattern phenotypes observed in the hippocampal formation, we weighted the constituent firing pattern elements according to the frequency of occurrence among 120 neuron types and electrophysiological subtypes (see *Methods*). As a result, infrequent firing pattern elements (PSWB, TSTUT and TSWB) received high weights (0.99, 0.95 and 0.93, respectively), very frequent elements (ASP and NASP) were assigned low weights (0.42 and 0.41), and common elements (D, RASP, PSTUT and SLN) obtained intermediate weights (0.90, 0.80, 0.88 and 0.87). Two-step cluster analysis identified ten firing pattern families as leaves of a seven-level hierarchical binary tree (A12 Fig.a). At the highest level, hippocampal neuron types and subtypes are divided into two major groups: those with spiking phenotypes (78%) and those with interrupted firing phenotypes (22%). The latter are separated into bursting (6%) and stuttering (16%), and each of these is subdivided into persistent and non-persistent families. A first group of the neuron types with spiking phenotypes is distinguished based on delay (9% of cell types). The remaining neuron types split into adapting (54%) and non-adapting phenotypes (15%). The adapting group consists of neuron types with rapidly adapting phenotypes (18%) and normally adapting (36%) phenotypes. Among the normally adapting group, the following phenotypes can be distinguished: discontinuous adapting spiking (6%) with ASP.SLN pattern, adapting-non-

adapting spiking (15%) with ASP.NASP patterns, and a last "spurious" phenotype of uncompleted adapting spiking (15%) with ASP. pattern only, for which the steady state (SLN or NASP) was not determined. This division of the adapting spiking groups reflects differences in adaptation rates, duration, and subsequent steady states.

This analysis also highlights the most distinguishing firing pattern elements of each family (A12 Fig.b). In particular, D. is the defining element for delayed spiking, PSTUT for persistent stuttering, ASP. and SLN for discontinuous adapting spiking. Each of the four major elements of interrupted firing patterns (PSWB, PSTUT, TSWB. and TSTUT.) is observed in a single firing pattern phenotype (persistent bursting, non-persistent bursting, persistent stuttering, and non-persistent stuttering, respectively). Other firing pattern elements (D., RASP., ASP., NASP, and SLN) appear in several firing pattern phenotypes. The proportions of non-defining firing pattern elements range from 5% to 83%.

The families of firing pattern phenotypes are differentially distributed within the set of 120 neuron types/subtypes (A12 Fig.c). Certain phenotype families are associated with excitatory neuron types, either exclusively (e.g. persistent bursting and non-persistent bursting) or predominantly (non-persistent stuttering, rapidly adapting, and adapting-non-adapting spiking). Conversely, persistent stuttering, delayed spiking, non-adapting spiking and simple adapting spiking are phenotypes composed largely by inhibitory neuron types. The discontinuous adapting spiking phenotype has relatively balanced proportions of excitatory and inhibitory neuron types.

The firing pattern phenotypes also have different distributions among the sub-regions of the hippocampal formation (A12 Fig.d). Among CA1 neuron types, the persistent stuttering (16%), non-adapting (24%), simple adapting (16%), and rapidly adapting spiking (13%) phenotypes are more common than other phenotypes; in DG, the most expressed phenotypes are delayed (20%), rapidly adapting (20%), and simple adapting spiking (15%); in EC, ASP-NASP (61%), discontinuous ASP. (11%), RASP. (28%), and NASP (19%) occur more often than other phenotypes.
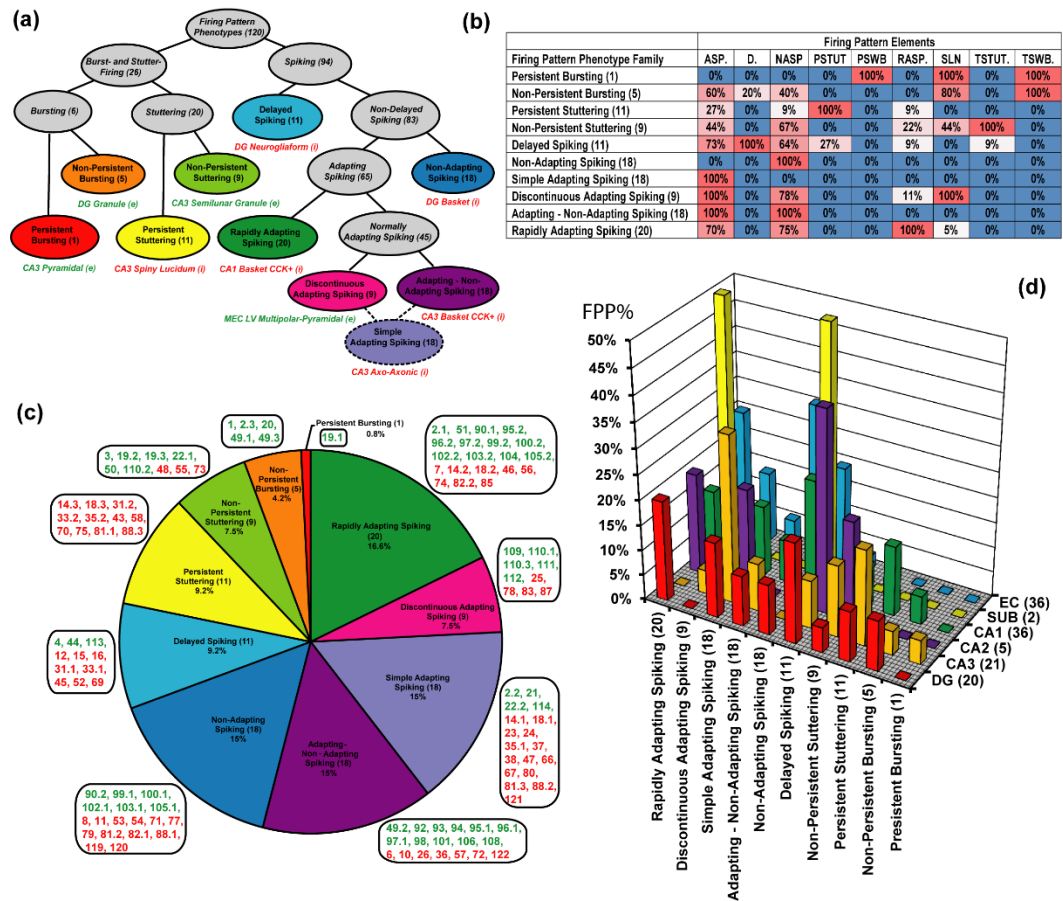
A12 Fig. Firing-pattern phenotype families from 120 neuron types/subtypes. (a) Hierarchical tree resulting from two-step clustering of weighted firing pattern elements with representative examples of cell types/subtypes that belong

to one of the corresponding firing-pattern phenotype families. Note that the simple adapting spiking pattern (ASP. only) constitutes a "spurious" phenotype of uncompleted adapting spiking (15%), for which the steady state (SLN or NASP) was not determined. (b) Percentage of occurrence of firing-pattern elements in families of firing pattern phenotypes. (c) Relative proportions of firing-pattern phenotype families among neuron types/subtypes. Green and red numbers represent excitatory and inhibitory cell types/subtypes as enumerated in A10 Fig.. (d) Distribution of firing-pattern phenotype families in sub-regions of the hippocampal formation. FPP% is percentage of expression of families of firing pattern phenotypes.

Usage of Information from Hippocampome.org

Searching and Browsing

The addition of firing pattern data to Hippocampome.org extends opportunities for broad-scope analytics and quick-use checks of neuron types. Similar to morphological, molecular, and biophysical information, firing patterns and their parameters can be browsed online with the interactive versions of the matrices presented in A10 Fig. (hippocampome.org/php/firing_patterns), along with an accompanying matrix to browse the stimulation parameters (duration and intensity) and the firing pattern parameters (delay, number of inter-spike intervals, etc.). Moreover, all classification and analysis results reported here can be searched with queries containing AND & OR Boolean logic using an intuitive graphical user interface (see Hippocampome.org → Search → Neuron Type). The integration within the existing comprehensive knowledge base enables any combination of both qualitative (e.g. PSTUT) and quantitative firing pattern properties, with molecular (e.g. calbindin-negative), morphological (e.g. axons in CA1 pyramidal layer), and biophysical (e.g. action potential width < 0.8 ms) filters (A13 Fig.). For example, of 13 neuron types with persistent stuttering, in 7 the largest inter-spike interval is more than 4 times longer than the subsequent ISI. When adding the other three selected criteria, the compound search leads to a single hit: CA1 Axo-axonic neurons (A13 Fig.a). Clicking on this result leads to the interactive neuron page (A13

173

Fig.b) where all information associated with a given neuron type is logically organized, including synonyms, morphology, biophysical parameters, molecular markers, synaptic connectivity, and firing patterns. Every property on the neuron pages and browse matrices, including firing patterns and their parameters, links to a specific evidence page that lists all supporting bibliographic citations, complete with extracted quotes and figures (A13 Fig.c). The evidence page also contains a table with all corresponding firing pattern parameters (A13 Fig.d), experimental details including information about animals (A13 Fig.e), preparations (A13 Fig.f), recording method and intra-pipette solution (A13 Fig.g), ACSF (A13 Fig.h), and a downloadable file of inter-spike intervals (A13 Fig.i).

A. Search by Property

Axon in CA1:SP (19)

CB- (24)

$ISI_{max}/ISI_{j+1}>4$ (10)

$AP_{width} <0.8$ ms (34)

PSUT (13)

(7) (3) (1) (8) (7) (6)

B. Neuron Page

Neuron Type

CA1 Axo-Axonic

C. Firing Pattern Evidence Page

CA1 Axo-Axonic
Firing pattern: persistent stuttering (PSTUT)
Source: Pawelzik H, Hughes DI, Thomson AM. Physiological and morphological diversity of immunocytochemically defined parvalbumin- and cholecystokinin-positive interneurones in CA1 of the adult rat hippocampus. J Comp Neurol (2002) 443 (4), 346 - 367. **PMID:** 11807843
Page location: p. 353, Fig. 4B, bottom

20mV
50ms
-66 mV
0.6nA

Parameters: Tstim = 356 ms, Istim = 600 pA
Author original FP description: Interrupted fast-spiking dischrge pattern
Linking PMID: 11807843
Linking Quote: All necessary morphological evidence is present in this self-same publication

D. Firing Pattern Parameters

Parameter Name	Value
Delay [Latency of first spike]	0.02 ms
PFS [Post Firing Silence]	8.45 ms
NISI [Number of ISIs]	53
ISI_{AV} [Average ISI]	6.59 ms
Max ISI [Maximum Interspike Interval]	67.03 ms
Min ISI [Minimum Interspike Interval]	2.85 ms
MaxISI/MinISI [Maximum ISI ratio]	23.55
MaxISIn /ISIn-1 [Ratio MaxISI to the previous ISI]	9.78
MaxISIn /ISIn+1 [Ratio MaxISI to the next ISI]	13.74
. . .	. . .

H. Solution

ACSF Parameter	Value
NaCl (mM)	124
KCl (mM)	3.3
$CaCl_2$ (mM)	2.5
KH_2PO_4 (mM)	1.2
$MgSO_4$ (mM)	1
$NaHCO_3$ (mM)	25.5
Glucose (mM)	15
O_2 %	95
CO_2 %	5
t (°C)	34 - 36
. . .	. . .

I. Interspike Intervals

ISI

E. Animals

Parameter	Value/ Characteristic
Species	rats
Inbred strain	Dawley Sprague
Age/Postnatal days	adult
Sex	male
Weight (g)	120 - 200
. . .	. . .

F. Preparation

Parameter	Value/Characteristic
Type of preparation	slice
Orientation	coronal
Thickness (mm)	450
. . .	. . .

G. Recording

Parameter	Value/Characteristic
Method	Intracellular recording
$KMeSO_4$ (mM)	2000
Biocytin (%)	2
. . .	. . .

A13 Fig. Hippocampome.org enables searching neuron types by neurotransmitter; axon, dendrite, and soma locations; molecular expression; electrophysiological parameters; input/output connectivity; firing patterns and firing pattern parameters. (a) Sample query for calbindin-negative neuron types with axons in CA1 stratum pyramidale, APwidth <0.8 ms, PSTUT firing, and ratio of maximum ISI to the next ISI greater than 4.8. Numbers in parentheses indicate the number of neuron types with the selected property or specific combination of properties. (b) Search results are linked to the neuron page(s). (c) The neuron page is linked to the firing pattern evidence page. Original data extracted from Pawelzik et al., 2002. All firing patterns parameters (d), experimental details including information about animals (e), preparations (f), recording method and intra-pipette solution (g), as well as ACSF composition (h) can be displayed. (i) Downloadable comma-separated-value file of inter-spike intervals.

175

The portal also reports, when available, the original firing pattern name descriptions used by the authors of the referenced publication (Hippocampome.org → Search → Original Firing Pattern) and provides links to corresponding published models from ModelDB (https://senselab.med.yale.edu/modeldb/).

Statistical analysis of categorical data

Firing pattern information more than doubles the Hippocampome.org knowledge base capacity to over 27,000 pieces of knowledge, that is, associations between neuron types and their properties. This extension allows for the confirmation of known tendencies and unearthing hidden relationships between firing patterns and molecular, biophysical, and morphological data in hippocampal neurons, which are otherwise difficult to find amongst the large body of literature. We computed p values using Bernard's exact test for 2×2 contingency tables that had a sum total of more than 9 elements. Comparisons of observable firing pattern elements with molecular markers expression, electrophysiological parameters, primary neurotransmitter and axonal projecting properties, with false discovery rates less than 0.25 ended with 26 statistically significant correlations. Several interesting examples of such findings are presented in A14 Fig.. For instance, adapting spiking (ASP.) tends to co-occur with expression of cholecystokinin (p=0.0113 with Barnard's exact test from all n = 26 pieces of evidence; see Lee et al., 2011 as an example); moreover, silence (SLN) after short firing discharge is not observed in neuron types with low (lower tercile of) membrane time constant (n=32, p=0.0235).

1. None of the 35 **glutamatergic** neuron types show persistent stuttering (**PSTUT**) (p=0.0083). Moreover, none of the 13 cell types with small slow afterhyperpolarization (**sAHP**) demonstrate this steady state (p=0.025). Thus, all PSTUT cells are GABAergic interneurons with large or intermediate sAHP.
2. Neither any of the 63 **non-projecting** (local circuit) neurons nor any of the 55 **GABAergic** neuron types display transient slow-wave bursting (**TSWB.**) (p=0.0214 and p=0.0215, respectively). In other words, TSWB cells in the hippocampus are a subset of projecting (long-range) glutamatergic neurons.
3. None of the 15 neuron types that express neuropeptide Y (**NPY**) and none of the 16 neuron types with low membrane time constant (τ_m) become silent (**SLN**) after short firing discharge (p=0.0037, FDR<0.05 and p=0.0235, respectively). In contrast, half of the 14 NPY-negative cells and nearly one third of the 16 neurons with high τ_m demonstrate this steady state.
4. All of the 10 neuron types that express cholecystokinin (**CCK**) and the overwhelming majority of neuron types with high input resistance (**R$_{in}$**)(17/18, except CA1 Cajal-Retzius) display adapting spiking (**ASP.**) (p=0.0113 and p=0.0373, respectively). On the other hand, this transient state is observed in just above half of CCK-negative cells (9/16) and two-thirds of cells with low or intermediate R$_{in}$ (12/18).
5. Of 14 neuron type with **wide AP**, only one (EC LV-VI Pyramidal-Polymorphic) shows delayed (**D.**) firing (p=0.021). On the contrary, nearly half of neuron types with **narrow AP** demonstrate this transient state (5/11).
6. With the exception of CA1 Basket, none of the 18 neuron types with low threshold potential (**V$_{thresh}$**) exhibit transient stuttering (**TSTUT.**) (p=0.0373). In contrast, one third (6/18) of neuron types with high V$_{thresh}$ demonstrate this transient.
7. While a half of 18 neuron types with high threshold potential (**V$_{thresh}$**) and more than half of neuron type (6/11) with **narrow AP** display non-adaptive spiking (**NASP**), only one (CA1 Shaffer Collateral-Associated) of 18 cells with low V$_{thresh}$ (p=0.0025, FDR<0.05) and only one (EC LVI Multipolar-Pyramidal) out of 25 neuron types with **wide AP** (p=0.021) do not show NASP.

A14 Fig. Examples of statistically significant correlations between firing pattern elements and known molecular, morphological and electrophysiological properties in hippocampal neurons. The p values are computed using Bernard's exact test for 2×2 contingency tables and satisfy FDR<0.25 (see Methods).

Analysis of numerical electrophysiological data

The extracted quantitative data allow one to study the relationship between firing

pattern parameters and membrane biophysics or spike characteristics, such as the

correlations between minimum inter-spike intervals (ISI_{min}) and action potential width

(AP_{width}). We analyzed these two variables in the 81 neuron types and subtypes for which

both measurements are available (A15 Fig.). The scatter plot of AP_{width} against ISI_{min}

reveals several distinct groupings (A15 Fig.a), and the corresponding histograms (Figs.

7b,c) demonstrate poly-modal distributions. The horizontal dashed line (ISI_{min}=34 ms)

separates 9 neurons with slow spikes (all excitatory except one) from 72 neurons (61% of

which are inhibitory) with fast and moderate spikes. The latter group shows a general

trend of ISI_{min} rise with increasing AP_{width} (black dashed line in panel A). This trend was

adequately fit with a linear function $Y = 13.79X - 0.05$ ($R = 0.72$; p=0.03). Neuron types

with slow spikes demonstrate the opposite trend, which was fit with a decreasing linear

function $Y = -26.72X + 76.42$ ($R = -0.91$, $p=10^{-6}$). Furthermore, the neuron types can be

separated by spike width. The vertical dashed lines *w1* (AP_{width}=0.73 ms) and *w2*

(AP_{width}=1.12 ms) separate neuron types with narrow, medium and wide action potentials.

The group of neuron types with narrow spikes (n=22) includes only inhibitory neurons,

which have AP_{width} in the range from 0.20 to 0.73 ms (0.54 ± 0.12 ms). In contrast, the

group of neuron types with wide spikes (n=28) contains only excitatory neurons with

AP_{width} in the range from 1.13 to 2.10 ms (1.49 ± 0.23 ms). The group of neuron types

with medium spikes (n = 31), with AP_{width} range from 0.74 to 1.12 ms (0.89 ± 0.12 ms),

includes a mix of inhibitory (74%) and excitatory (26%) neurons.
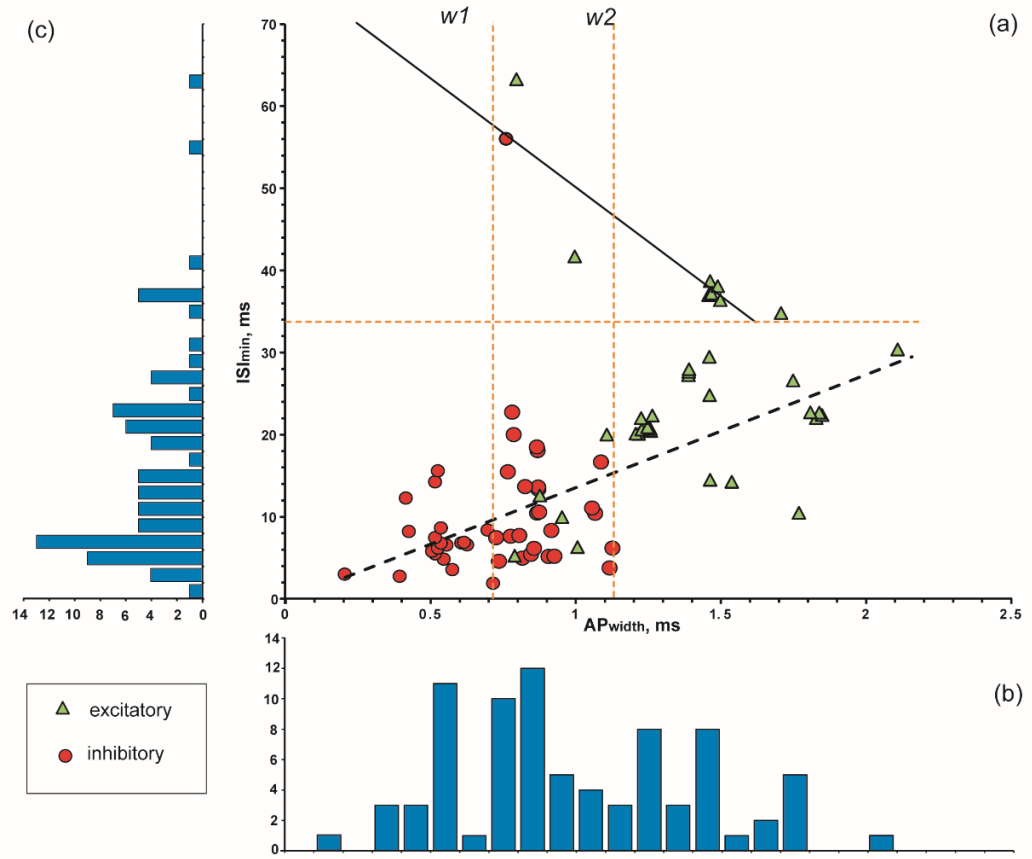
A15 Fig. Relationships between the width of action potentials (APwidth) and minimum of inter-spike intervals (ISImin) for 84 neuron types and subtypes. (a) APwidth - ISImin scatter diagram with results of linear regression.

179

Green triangles and red circles indicate excitatory and inhibitory neurons, respectively. Dashed orange lines: horizontal line separates neurons with slow spikes from neurons with fast and moderate spikes; vertical lines (w1 and w2) separate neurons with narrow, medium and wide action potentials. Black lines: solid line shows linear fitting for slow spike neurons with a function $Y = -26.72X + 76.42$ ($R^2 = 0.83$); dashed line shows general linear fitting for fast and moderate spike neurons with a function $Y = 13.79X - 0.05$ ($R^2 = 0.52$). (b) APwidth histogram. (c) ISI histogram.

Among the 22 neuron types/subtypes from the group with $AP_{width} < 0.72$ ms, 13 demonstrated so-called fast spiking behavior, which is distinguished by narrow spikes, high firing rate, and the absence or weak expression of spike frequency adaptation (Jonas et al., 2004). Besides these common characteristics, however, their firing patterns vary broadly even from a qualitative standpoint. Five of these 13 neuron types belong to the PSTUT family, namely CA3 Trilaminar (Gloveli et al., 2005), CA3 Aspiny Lucidum ORAX (Spruston et al., 1997), CA2 Basket (Mercer et al., 2007), CA1 Axo-axonic (Pawelzik et al., 2002), and CA1 Radial Trilaminar (Tricoire et al., 2011). Three types belong to the NASP family: DG Basket (Savanthrapadian et al., 2014), CA1 Horizontal Axo-axonic (Tricoire et al., 2011), and MEC LIII Superficial Multipolar Interneuron (Kumar and Buckmaster, 2006). Two types, CA3 Axo-axonic (Dugladze et al., 2012) and CA2 Bistratified (Mercer et al., 2007), belong to the simple adapting spiking family; two types, DG HICAP (Mott et al., 1997) and DG AIPRIM (Lübke et al., 1998), belong to the ASP-NASP family; and lastly CA1 Basket (Lee et al., 2011) belongs to non-persistent stuttering family.

Additionally, firing pattern families are unequally distributed among the groupings revealed by the above analysis. Persistent and non-persistent stuttering families and non-persistent bursting phenotypes are composed entirely of neuron types with narrow and medium fast/moderate spikes. Conversely, the rapidly adapting – non-

adapting spiking phenotype is represented solely by neurons with spikes of intermediate width.

Discussion

Neurons differ from each other by morphological and molecular features including the diversity and distribution of ion membrane channels in somata and dendrites. These intrinsic properties determine important physiological functions such as excitability, efficacy of synaptic inputs (Häusser et al., 2000; London et al., 2002; Komendantov et al., 2009), shapes of individual action potentials and their frequency (Bean, 2007), and temporal patterns (Mainen and Sejnowski, 1996; Krichmar et al., 2006).

In the neuroscience literature, the firing patterns of neuronal activity are commonly used to characterize or identify groups of neurons. Examples include descriptions of "strongly adapting, normally adapting, and nonadapting cells" (Mott et al., 1997); "fast-spiking and non-fast-spiking" interneurons (Bjorefeldt et al., 2016); "late spiking" cells (Tamas et al., 2003); "stuttering interneurons" (Song et al., 2013); "bursting" and "non-bursting" neurons (Hablitz and Johnston, 1981; Masukawa et al., 1982); "regular spiking, bursting, and fast spiking" (McCormick et al., 1985), and many more. However, it has until now remained challenging to integrate these characterizations across different laboratories and studies besides largely qualitative summaries.

In this study, we show that a quantitative, data-driven methodology based on the analysis of transients and steady states of evoked spiking activity can meaningfully classify the firing patterns of hippocampal neuronal types. This work is a further

181

development of the effort initiated by the Petilla Interneuron Nomenclature Group (Ascoli et al., 2008), which was applied to firing patterns in cortical neurons (Markram et al., 2015; Druckmann et al., 2013). At the same time, this work demonstrates the feasibility of systematic, comprehensive meta-analysis of electrophysiological data from the published literature. This is especially important as a necessary approach to help link and interpret the growing information from centralized, large-scale, "industrial" neuroscience projects (Kandel et al., 2013; Migliore et al., 2018; Teeter et al., 2018) with the distributed accumulation of data in traditional research laboratories (Ferguson et al., 2014).

From the electrophysiological recordings of 90 neuron types in the rodent hippocampus, we identified 23 firing patterns, 15 of which were completed, that is, included both transient(s) and putative steady state components (see A10 Fig. and A11 Fig.). Taking into consideration the firing pattern information enables a possible refinement of neuron type delineation by identifying 52 putative electrophysiological subtypes among 22 neuron types. Subsequent two-step cluster analysis allows for the clear distinguishing of 9 unique families of 44 firing pattern phenotypes among 120 neuron types and putative subtypes. Notwithstanding the focus of the present research on the hippocampal formation, the firing pattern classification framework introduced with this study can be readily applied to spiking activity of neurons from other brain regions.

The two firing pattern families characterized by bursting phenotypes (transient and persistent) are comprised of excitatory neurons, while the persistent stuttering family only included inhibitory neurons. However, the majority of phenotype families are mixed

between putatively glutamatergic and GABAergic types (A12 Fig.c). Thus, the identification of a firing pattern phenotype by itself is a useful but in most cases insufficient attribute for a reliable categorization of excitatory and inhibitory neurons.

The frequency of discharges is an important characteristic of neuronal communication. Many neuron types, especially interneurons, show fast spiking behavior: they are capable of firing at high frequencies (200 Hz or more) with little decrease in frequency during prolonged stimulation (Bean, 2007; Jonas et al., 2004). Spike frequency correlates with electrophysiological characteristics, such as action potential duration or fast AHP amplitude (Druckmann et al., 2013). Fast spiking neurons typically have narrow action potentials and high-amplitude fast AHP (Bean, 2007). Our correlation analysis of Hippocampome.org data reveals that transient stuttering (TSTUT.) is not typical for cells with extremely high-amplitude fast AHPs and delayed firing (D.) is not characteristic for neuron types with wide action potentials (A14 Fig.). Interestingly, plotting ISI_{min} against AP_{width} for all neuron types with relatively faster firing (maximum frequencies higher than ~30 Hz) and for all neuron types with slower firing (maximum frequencies lower than 29 Hz) reveals opposite, statistically significant linear relationships (A15 Fig.a).

Firing pattern phenotypes of central mammalian neurons are determined by biophysical properties associated with expression and distribution of several types of Ca^{2+} and K^+ channels, which modulate specific ion currents (Bean, 2007; Llinás, 1988; Migliore et al., 2005) and may correlate with expression of other molecular markers (Markram et al., 2004; Ascoli et al., 2008; Caballero et al., 2014). Despite the relative

sparsity of molecular marker information, analysis of the correlations between firing

patterns and other neuronal properties revealed novel interesting relationships in

hippocampal neuron types (A14 Fig.).

Firing patterns play important roles in neural networks including the

representation of input features, transmission of information, and synchronization of

activity across separate anatomical regions or distinct cell assemblies. Although single

spikes can provide temporally precise neurotransmitter release, this release usually has

low probability in central synapses. Neurons can compensate for the unreliability of their

synapses by transmitting signals via multiple synaptic endings or repeatedly activating a

single synapse (Lisman, 1997). Thus, a short high-frequency sequence of action

potentials may cross a synapse more reliably, increasing the likelihood of a postsynaptic

spike (Zeldenrust et al., 2018). This can also be affected by short-term synaptic plasticity

(Zucker and Regehr, 2002; Citri and Malenka, 2008), which varies with age and with the

identity of pre- and post-synaptic neurons. Moreover, single burst of action potentials in

CA3 axons (Schaffer collaterals) can induce robust and stable long-term potentiation at

synapses on CA1 pyramidal neurons, provided that the postsynaptic depolarization

triggers a dendritic spike (Remy and Spruston, 2007). Recent results have also revealed

that single bursts in DG granule cells may selectively alter specific functional

components of the downstream circuit, such as feedforward inhibitory interneurons

(Neubrandt et al., 2018). Experimental studies provide strong evidence that different

brain circuits employ distinct schemes to encode and propagate information (Xu et al.,

2012): while information relay by isolated spikes is insignificant for the acquisition of

recent contextual memories in the hippocampus, it is essential for memory function in the medial prefrontal cortex. However, even within the hippocampus, different neuronal circuits may employ distinct coding schemes by relying on isolated spikes or bursts of spikes for execution of critical functions (Xu et al., 2012). Indeed, distinct sub-regions of the hippocampal formation show differential distributions of spiking, bursting, and stuttering firing pattern phenotypes (A12 Fig.).

In this study, the phenotyping of most types of neurons was based on the quantitative analysis of data extracted from single (or limited numbers of) figures exemplified neuronal electrical activity in relevant publications. Until neuroscience switches to the systematic deposition of all firing traces recorded and analyzed for a given publication to public repositories, such representative illustrations, however limited, constitute a fairly accurate reflection of the communal knowledge about neuronal physiology in particular neural system. Thus, our approach is based on the statistical quantification of integrated data presented in the literature.

The findings presented in this report resulted from the analysis of firing patterns in response to depolarizing current. To this date, this is by far the most common experimental protocol for characterizing the neuronal input-output function. Nevertheless, different types of neurons also exhibit distinct responses to hyperpolarization, as well as to its termination. For example, several neuron types described in Hippocampome.org demonstrate rebound spiking: CA1 Trilaminar (Sik, 1995), CA1 Back-Projection (Sik, 1994), CA1 O-LM (Sik, 1995), CA1 SO-SO (Pawelzik, et al., 2002), MEC LIII Multipolar Interneuron (Kumar and Buckmaster,

2006), MEC LII Stellate (Canto and Witter, 2012), MEC LII Oblique Pyramidal (Canto and Witter, 2012). Such neuronal behaviors, owing to the hyperpolarization-activated cation current (h-current), may play an important role in hippocampal rhythmogenesis (Hasselmo, 2013) and could be locally modulated by activity-dependent changes in intrinsic excitability (Ascoli et al., 2010). It will therefore be interesting to extend the current firing pattern phenotyping by considering these additional neuronal properties in future work.

The information on firing patterns of neuron types further expands the rich knowledge base of neuronal properties Hippocampome.org, which already contained information on morphology, molecular marker expression, connectivity, and other electrophysiological characteristics (Wheeler et al., 2015). Computation of the potential connectivity map of all known 122 neuron types by supplementing available synaptic data with spatial distributions of axons and dendrites enabled the reconstruction of a circuitry containing more than 3200 putative connections (Rees et al., 2016).

Modern experimental techniques allow to conduct detailed morphological analysis (Deitcher et al., 2017) and digital reconstructions of neurons (Ascoli et al., 2007), collect biophysical and electrophysiological data, and develop complex multi-compartmental models in order to study synaptic efficacy (Komendantov and Ascoli, 2009), synaptic (Poirazi et al., 2003) and dendritic integration (Eberhardt et al., 2019), dendritic input discrimination capabilities (Zippo et al., 2015), and other neuronal properties. The main feature of the Hippocampome.org knowledge base is general information about location of dendrites and axons in different sections and layers of the

186

hippocampus, which serves as the basis for neuron type classification. Similarly, we selected, extracted, and systematized basic electrophysiological parameters and firing pattern information, which gave us the opportunity for quantitative firing pattern phenotyping and comprehensive coverage of intrinsic diversity of neuronal types with simple models (Venkadesh et al., 2018). We developed compact multi-compartment models with up to four compartments, which will allow spatial segregation of synaptic integration and significantly reduce the computational cost of large-scale network simulations (Venkadesh et al., 2019). More detailed morphological, electrophysiological and molecular information can be found on the provided links to the cited articles, as well as to the models published in the ModelDB (McDougal et al., 2017). Among them are multicompartment models that consider the details of the morphology and biophysical properties, including distributions of specific ion channels and synaptic inputs, such as models of CA1 Pyramidal cells with non-uniformly distributed A-type potassium and hyperpolarization-activated channels (Migliore et al., 2018; Bezaire et al., 2016) based on experimental observations.

This ongoing accumulation of data and knowledge makes Hippocampome.org a powerful tool for building real-scale models of the entire hippocampal formation, thus substantially expanding the potential scope of recent advances in this regard (McDougal et al., 2017). More generally, such knowledge bases are playing an increasingly important role in neuroscience research by fostering computational analyses and data-driven simulations.

REFERENCES

Adrian, E.D. and Zotterman, Y. (1926). The impulses produced by sensory nerve endings: Part 3. Impulses set up by touch and pressure. J. Physiol. 61, 465-483.

Aizenman, C.D., and Linden, D.J. (2000). Rapid, synaptically driven increases in the intrinsic excitability of cerebellar deep nuclear neurons. *Nature neuroscience.* doi: 10.1038/72049.

Alexander, J. C., Yorke, J. A., You, Z., and Kan, I. (1992). RIDDLED BASINS. *International Journal of Bifurcation and Chaos.* 02, 795–813. doi:10.1142/S0218127492000446.

Ali, A.B., and Thomson, A.M. (1998). Facilitating pyramid to horizontal oriens-alveus interneurone inputs: dual intracellular recordings in slices of rat hippocampus. *The Journal of Physiology.* 507(1):185-99.

Aou, S., Woody, C.D., and Birt, D. (1992). Increases in excitability of neurons of the motor cortex of cats after rapid acquisition of eye blink conditioning. *Journal of Neuroscience.* 12: 560–9.

Armstrong, C., Szabadics, J., Tamás, G., and Soltesz, I. (2011). Neurogliaform cells in the molecular layer of the dentate gyrus as feed-forward γ-aminobutyric acidergic modulators of entorhinal–hippocampal interplay. *Journal of Comparative Neurology.* 519(8):1476-91.

Ascoli, G. A., Donohue, D. E., and Halavi, M. (2007). NeuroMorpho.Org: a central resource for neuronal morphologies. *Journal of Neuroscience.* 27, 9247–9251.

Ascoli, G.A., Gasparini, S., Medinilla, V. and Migliore, M. (2010). Local control of postinhibitory rebound spiking in CA1 pyramidal neuron dendrites. *J. Neurosci.* 30,6434-6442.

Babiec, W. E., Jami, S. A., Guglietta, R., and Chen, P. B. (2017). Differential regulation of NMDA receptor-mediated transmission by SK channels underlies dorsal-ventral differences in dynamics of Schaffer collateral synaptic function. *Journal of Neuroscience.* 3196-16; DOI: https://doi.org/10.1523/JNEUROSCI.3196-16.2017

Badel, L., Lefort, S., Brette, R., Petersen, CC., Gerstner, W., and Richardson, M.J. (2008). Dynamic IV curves are reliable predictors of naturalistic pyramidal-neuron voltage traces. *Journal of Neurophysiology.* 99: 656–666.

Barnard, G.A. (1947). Significance tests for 2×2 tables. *Biometrika* 34, 123–138

Bausch, S. B., He, S., Petrova, Y., Wang, X.-M., and McNamara, J. O. (2006). Plasticity of both excitatory and inhibitory synapses is associated with seizures induced by removal of chronic blockade of activity in cultured hippocampus. *J. Neurophysiol.* 96, 2151–2167.

Bean, B.P. (2007). The action potential in mammalian central neurons. *Nat. Rev. Neurosci.* 8, 451-465

Benda, J., and Herz, A.V. (2003). A universal model for spike-frequency adaptation. *Neural computation* 15: 2523–2564.

Benjamini, Y. and Hochberg, Y. (1995). Controlling the false discovery rate: a practical and powerful approach to multiple testing. *J. R. Stat. Soc. Ser. B Methodol.* 57, 289-300.

Beyeler, M., Carlson, K.D., Chou, T.S., Dutt, N., and Krichmar, J.L. (2015). A User-Friendly and Highly Optimized Library for the Creation of Neurobiologically Detailed Spiking Neural Networks. In *International Joint Conference on Neural Networks*.

Beyeler, M., Richert, M., Dutt, N. D., and Krichmar, J. L. (2014). Efficient spiking neural network model of pattern motion selectivity in visual cortex. *Neuroinformatics*, 12(3), 435-454.

Bezaire, M. J., Raikov, I., Burk, K., Vyas, D., and Soltesz, I. (2016). Interneuronal mechanisms of hippocampal theta oscillations in a full-scale model of the rodent CA1 circuit. *Elife* 5. doi:10.7554/eLife.18566.

Bilkey, D.K. and Schwartzkroin, P.A. (1990). Variation in electrophysiology and morphology of hippocampal CA3 pyramidal cells. *Brain Res.* 514, 77-83.

Bjorefeldt, A., Wasling, P., Zetterberg, H. and Hanse, E. (2016). Neuromodulation of fast-spiking and non-fast-spiking hippocampal CA1 interneurons by human cerebrospinal fluid. *J. Physiol.* 594, 937-952.

Brette, R., and Gerstner, W. (2005). Adaptive exponential integrate-and-fire model as an effective description of neuronal activity. *Journal of neurophysiology*, 94(5), 3637-3642.

Buchanan, T.W. Retrieval of emotional memories. (2007). Psychol. Bull. 133, 761-779.

Buckmaster, P.S., Strowbridge, B.W., and Schwartzkroin, P.A. (1993). A comparison of rat hippocampal mossy cells and CA3c pyramidal cells. *Journal of Neurophysiology*. 70(4):1281-99.

Buhl, E.H. *et al.* (1994). Physiological properties of anatomically identified axo-axonic cells in the rat hippocampus. *J. Neurophysiol.* 71, 1289-1307

Buzsáki, G. (2010). Neural syntax: cell assemblies, synapsembles, and readers. *Neuron* 68, 362–385.

Buzsáki, G., and Chrobak, J. J. (1995). Temporal structure in spatially organized neuronal ensembles: a role for interneuronal networks. *Current opinion in neurobiology*, 5(4), 504-510.

Caballero, A., Flores-Barrera, E., Cass, D.K. and Tseng, K.Y. (2014). Differential regulation of parvalbumin and calretinin interneurons in the prefrontal cortex during adolescence. *Brain Struct. Funct.* 219, 395-406.

Calixto, E., Galván, E. J., Card, J. P., and Barrionuevo, G. (2008). Coincidence detection of convergent perforant path and mossy fibre inputs by CA3 interneurons. *The Journal of Physiology*, 586(11), 2695-2712.

Cannon, R. C., Gleeson, P., Crook, S., Ganapathy, G., Marin, B., Piasini, E., et al. (2014). LEMS: a language for expressing complex biological models in concise and

hierarchical form and its use in underpinning NeuroML 2. *Front. Neuroinform*. 8, 79.

Canto, C. B., and Witter, M. P. (2012). Cellular properties of principal neurons in the rat entorhinal cortex. II. The medial entorhinal cortex. *Hippocampus*, 22(6), 1277-1299.

Cardin, J.A., Carlén, M., Meletis, K., Knoblich, U., Zhang, F., Deisseroth, K., Tsai, L-H., and Moore, CI. (2009). Driving fast-spiking cells induces gamma rhythm and controls sensory responses. *Nature*. 459: 663–667.

Carnevale, N.T., Tsai, K.Y., Claiborne, B.J., and Brown, T.H. (1997). Comparative electrotonic analysis of three classes of rat hippocampal neurons. *Journal of Neurophysiology*. 78: 703–20.

Chevaleyre, V., and Siegelbaum, S. A. (2010). Strong CA2 pyramidal neuron synapses define a powerful disynaptic cortico-hippocampal loop. *Neuron*, 66(4), 560-572.

Citri, A., Malenka, R.C. (2008). Synaptic plasticity: multiple forms, functions, and mechanisms. *Neuropsychopharmacology* 33, 18-41

Chiong, R. (Ed.). (2009). *Nature-inspired algorithms for optimisation* (Vol. 193). Springer.

Chittajallu, R., Craig, M.T., McFarland, A., Yuan, X., Gerfen, S., Tricoire, L., Erkkila, B., Barron, S.C., Lopez, C.M., Liang, B.J., Jeffries, B.W. (2013). Dual origins of functionally distinct O-LM interneurons revealed by differential 5-HT3AR expression. *Nature neuroscience*. 16(11):1598-607.

Chitwood RA, Hubbard A, and Jaffe DB. (1999). Passive electrotonic properties of rat hippocampal CA3 interneurones. *The Journal of Physiology*. 515: 743–756.

Coello, C. A. C., Van Veldhuizen, D. A., and Lamont, G. B. (2002). *Evolutionary algorithms for solving multi-objective problems* (Vol. 242). New York: Kluwer Academic.

Colbert, C. M., Magee, J. C., Hoffman, D. A., and Johnston, D. (1997). Slow recovery from inactivation of Na+ channels underlies the activity-dependent attenuation of dendritic action potentials in hippocampal CA1 pyramidal neurons. *J. Neurosci*. 17, 6512–6521.

Connors B.W. and Gutnick, M.J. (1990). Intrinsic firing patterns of diverse neocortical neurons. Trends Neurosci. 13, 99-104.

Cope, D. W., Maccaferri, G., Marton, L. F., Roberts, J. D. B., Cobden, P. M., and Somogyi, P. (2002). Cholecystokinin-immunopositive basket and Schaffer collateral-associated interneurones target different domains of pyramidal cells in the CA1 area of the rat hippocampus. *Neuroscience*, 109(1), 63-80.

Davidor, Y. (1991). *Epistasis variance: A viewpoint on GA-hardness.Foundations of genetic algorithms*, 1, 23-35.

De Jong, K.A. (2006). *Evolutionary computation: a unified approach.* MIT press.

Deb, K. (2001). *Multi-objective optimization using evolutionary algorithms* (Vol. 16). John Wiley and Sons.

Deitcher, Y. *et al.* (2017). Comprehensive morpho-electrotonic analysis shows 2 distinct classes of L2 and L3 pyramidal neurons in human temporal cortex. Cereb. Cortex 27, 5398-5414

Desai, N.S., Rutherford, L.C., and Turrigiano, G.G. (1999). Plasticity in the intrinsic excitability of cortical pyramidal neurons. *Nature neuroscience*. doi: 10.1038/9165.

Desai, N.S. (2003). Homeostatic plasticity in the CNS: synaptic and intrinsic forms [Online]. *Journal of Physiology-Paris* 97: 391–402. http://www.sciencedirect.com/science/article/pii/S0928425704000166.

Dragoi, G., and Buzsáki, G. (2006). Temporal encoding of place sequences by hippocampal cell assemblies. *Neuron* 50, 145–157. doi: 10.1016/j.neuron.2006.02.023.

Druckmann, S., Banitt, Y., Gidon, A., Schürmann, F., Markram, H., and Segev, I. (2007). A novel multiple objective optimization framework for constraining conductance-based neuron models by experimental data. *Frontiers in neuroscience*, 1(1), 7.

Druckmann, S., Hill, S., Schürmann. F., Markram, H. and Segev, I. (2013). A hierarchical structure of cortical interneuron electrical diversity revealed by automated statistical analysis. Cereb Cortex 23:2994-3006.

Dugladze, T., Schmitz, D., Whittington, M.A., Vida, I. and Gloveli, T. (2012). Segregation of axonal and somatic activity during fast network oscillations. *Science* 336, 1458-1461.

Eberhardt, F., Herz, A.V.M., Häusler, S. (2019). Tuft dendrites of pyramidal neurons operate as feedback-modulated functional subunits. *PLoS Comput. Biol.* 15, 3; 10.1371/journal.pcbi.1006757

Eichenbaum, H., Otto, T. and Cohen, N.J. (1992). The hippocampus - what does it do? Behav. Neural Biol. 57, 2-36.

Eichenbaum, H. (2000). A cortical-hippocampal system for declarative memory. Nat. Rev. Neurosci. 1, 41-50.

Eichenbaum, H. (2017). The role of the hippocampus in navigation is memory. J. Neurophysiol. 117, 1785-1796.

Eliasmith, C., Stewart, T.C., Choo, X., Bekolay, T., DeWolf, T., Tang, Y., Tang, C., and Rasmussen, D. (2012). A large-scale model of the functioning brain. *Science* 338: 1202–5.

Ermentrout, B., Pascal, M., and Gutkin, B. (2001).The effects of spike frequency adaptation and negative feedback on the synchronization of neural oscillators. *Neural Computation*. doi: 10.1162/08997660152002861.

Ermentrout, B. (1996). Type I membranes, phase resetting curves, and synchrony. *Neural computation*, 8(5), 979-1001.

Ermentrout, B. (2002). Simulating, Analyzing, and Animating Dynamical Systems: A Guide to XPPAUT for Researchers and Students. SIAM.

Eshelman, J. D. S. L. J. (2014). Spurious correlations and premature convergence in genetic algorithms. *Foundations of Genetic Algorithms 1991* (FOGA 1), 1, 102.

Ferguson, A.R., Nielson, J.L., Cragin, M.H., Bandrowski, A.E. and Martone, M.E. (2014). Big data from small data: data-sharing in the 'long tail' of neuroscience. *Nat. Neurosci.* 17, 1442-1447.

Ferguson, K. A., Chatzikalymniou, A. P., and Skinner, F. K. (2017). Combining Theory, Model, and Experiment to Explain How Intrinsic Theta Rhythms Are Generated

in an In Vitro Whole Hippocampus Preparation without Oscillatory Inputs. *eNeuro* 4. doi:10.1523/ENEURO.0131-17.2017.

Fingelkurts, A. A., and Fingelkurts, A. A. (2004). Making complexity simpler: multivariability and metastability in the brain. *Int. J. Neurosci.* 114, 843–862. doi:10.1080/00207450490450046.

Foster, W.R., and Ungar, L.H. (1993). Significance of conductances in Hodgkin-Huxley models. *Journal of Neurophysiology* 70(6): 2502-2518.

Freeman, W. J. (1999). Consciousness, intentionality and causality. *Journal of Consciousness Studies*, *6*(11-12), 143-172.

Freeman, W. J., and Holmes, M. D. (2005). Metastability, instability, and state transition in neocortex. *Neural Netw.* 18, 497–504. doi: 10.1016/j.neunet.2005.06.014.

Frégnac, Y. (2017). Big data and the industrialization of neuroscience: A safe roadmap for understanding the brain? *Science* 358, 470–477.

Fujii, H., and Tsuda, I. (2004a). Itinerant Dynamics of Class I* Neurons Coupled by Gap Junctions. in *Computational Neuroscience: Cortical Dynamics* (Springer Berlin Heidelberg), 140–160. doi:10.1007/978-3-540-27862-7_8.

Fujii, H., and Tsuda, I. (2004b). Neocortical gap junction-coupled interneuron systems may induce chaotic behavior itinerant among quasi-attractors exhibiting transient synchrony. *Neurocomputing* 58–60, 151–157. doi: 10.1016/j.neucom.2004.01.036.

Fuentealba., P. *et al.* (2010). Expression of COUP-TFII nuclear receptor in restricted GABAergic neuronal populations in the adult rat hippocampus. *J. Neurosci.* 30, 1595-1609.

Geit, V., Schutter, D., and Achard. (2008). Automated neuron model optimization techniques: a review. *Biological cybernetics* 99: 241–51.

Geit, W., Achard, P., and Schutter E. (2007). Neurofitter: a parameter tuning package for a wide range of electrophysiological neuron models. *Frontiers in neuroinformatics* 1: 1. doi:10.3389/neuro.11.001.2007

Gerken, W. C., Purvis, L. K., and Butera, R. J. (2006). Genetic algorithm for optimization and specification of a neuron model. *Neurocomputing*, 69(10), 1039-1042.

Ghosh-Dastidar, S., and Adeli, H. (2009). Spiking neural networks. *International journal of neural systems*, 19(04), 295-308.

Gloveli, T. et al. (2005). Differential involvement of oriens/pyramidale interneurones in hippocampal network oscillations *in vitro*. *J. Physiol.* 562, 131-147.

Golding, N.L., Mickus, T.J., Katz, Y., Kath, W.L., and Spruston, N. (2005). Factors mediating powerful voltage attenuation along CA1 pyramidal neuron dendrites. *Journal of Physiology*. doi: 10.1113/jphysiol.2005.086793.

Golding, N. L., Kath, W. L., and Spruston, N. (2001). Dichotomy of action-potential backpropagation in CA1 pyramidal neuron dendrites. *J. Neurophysiol.* 86, 2998–3010.

Goldwyn, J. H., and Shea-Brown, E. (2011). The what and where of adding channel noise to the Hodgkin-Huxley equations. *PLoS Comput. Biol*, 7(11), e1002247.

Golomb, D., Yue, C. and Yaari, Y. (2006). Contribution of persistent Na$^+$ current and M-type K$^+$ current to somatic bursting in CA1 pyramidal cells: combined experimental and modeling study. *J. Neurophysiol.* 96, 1912-1926.

Gulyás, A. I., Szabó, G. G., Ulbert, I., Holderith, N., Monyer, H., Erdélyi, F., Szabó, G., Freund, T.F., and Hájos, N. (2010). Parvalbumin-containing fast-spiking basket cells generate the field potential oscillations induced by cholinergic receptor activation in the hippocampus. *The Journal of neuroscience.* 30(45):15134-45.

Gütig, R., and Sompolinsky, H. (2006). The tempotron: a neuron that learns spike timing–based decisions. *Nature neuroscience*, 9(3), 420-428.

Hablitz, J.J. and Johnston, D. (1981). Endogenous nature of spontaneous bursting in hippocampal pyramidal neurons. *Cell. Mol. Neurobiol.* 1, 325-334.

Hafting, T., Fyhn, M., Molden, S., Moser, M.B. and Moser, E.I. (2005). Microstructure of a spatial map in the entorhinal cortex. Nature 436, 801-806.

Hamam, B. N., Amaral, D. G., and Alonso, A. A. (2002). Morphological and electrophysiological characteristics of layer V neurons of the rat lateral entorhinal cortex. *Journal of Comparative Neurology*, 451(1), 45-61.

Hamilton, D.J. *et al.* (2017). Name-calling in the hippocampus (and beyond): coming to terms with neuron types and properties. *Brain Inform.* 4, 1-12.

Han, Z.S., Buhl, E.H., Lörinczi, Z. and Somogyi, P. (1993). A high degree of spatial selectivity in the axonal and dendritic domains of physiologically identified local-circuit neurons in the dentate gyrus of the rat hippocampus. *Eur. J. Neurosci.* 5, 395-410

Harris, K. D., Hochgerner, H., Skene, N. G., Magno, L., Katona, L., Bengtsson Gonzales, C., et al. (2018). Classes and continua of hippocampal CA1 inhibitory neurons revealed by single-cell transcriptomics. *PLoS Biol.* 16, e2006387.

Hasselmo, M.E. (2013). Neuronal rebound spiking, resonance frequency and theta cycle skipping may contribute to grid cell firing in medial entorhinal cortex. *Phil. Trans. R. Soc. B* 369, 20120523.

Häusser, M., Spruston, N. and Stuart, G.J. (2000). Diversity and dynamics of dendritic signaling. *Science* 290, 739-744.

Hemond, P., Epstein, D., Boley, A., Migliore, M., Ascoli, G. A., and Jaffe, D. B. (2008). Distinct classes of pyramidal cells exhibit mutually exclusive firing patterns in hippocampal area CA3b. *Hippocampus*, 18(4), 411.

Hendrickson, P.J., Gene, J.Y., and Song, D. (2016). A million-plus neuron model of the hippocampal dentate gyrus: critical role for topography in determining spatiotemporal network dynamics. *IEEE Transactions on Biomedical Engineering* 63.1: 199-209.

Herculano-Houzel, S., Mota, B., and Lent, R. (2006). Cellular scaling rules for rodent brains. *Proc. Natl. Acad. Sci.* U. S. A. 103, 12138–12143. doi:10.1073/pnas.0604911103.

Hines, M. L., and Carnevale, N. T. (1997). The NEURON simulation environment. *Neural Comput.* 9, 1179–1209.

Hodgkin, A. L., and Huxley, A. F. (1952). A quantitative description of membrane current and its application to conduction and excitation in nerve. *The Journal of physiology*, 117(4), 500-544.

Hoel, E.P., Albantakis, L., Marshall, W. and Tononi, G. (2016). Can the macro beat the micro? Integrated information across spatiotemporal scales. *Neuroscience of Consciousness*, *2016*(1).

Hoffman, D. A. (1999). Role of an A-Type K Conductance in the Back-Propagation of Action Potentials in the Dendrites of Hippocampal Pyramidal Neurons. *J. Comput. Neurosci.* 7, 5–15.

Hoffman, D. A., Magee, J. C., Colbert, C. M., and Johnston, D. (1997). K+ channel regulation of signal propagation in dendrites of hippocampal pyramidal neurons. *Nature* 387, 869–875.

Hong, G., and Lieber, C. M. (2019). Novel electrode technologies for neural recordings. *Nat. Rev. Neurosci.* 20, 330–345. doi:10.1038/s41583-019-0140-6.

Ishizuka, N., Cowan, W. M., and Amaral, D. G. (1995). A quantitative analysis of the dendritic organization of pyramidal cells in the rat hippocampus. *J. Comp. Neurol*. 362, 17–45.

Ivanchenko, M. V., Osipov, G. V., Shalfeev, V. D., and Kurths, J. (2004). Phase synchronization in ensembles of bursting oscillators. *Phys. Rev. Lett.* 93, 134101. doi:10.1103/PhysRevLett.93.134101.

Izhikevich, E. M., and Edelman, G.M. (2008). Large-scale model of mammalian thalamocortical systems. *Proc. Natl. Acad. Sci.* U.S.A. 105: 3593–8.

Izhikevich, E. M. (2000). Neural excitability, spiking and bursting. *International Journal of Bifurcation and Chaos*, 10(06), 1171-1266.

Izhikevich, E. M. (2001). Resonate-and-fire neurons. *Neural networks*. 14(6):883–94.

Izhikevich, E. M. (2003). Simple model of spiking neurons. *IEEE Transactions on Neural Networks*. 14: 1569–72.

Izhikevich, E. M. (2004). Which model to use for cortical spiking neurons?. *IEEE transactions on neural networks,* 15(5), 1063-1070.

Izhikevich, E. M. (2007). *Dynamical Systems in Neuroscience*. MIT Press Available at: https://market.android.com/details?id=book-kVjM6DFk-twC.

Izhikevich, E. M. (2010). Hybrid spiking models. *Philosophical Transactions of the Royal Society of London A: Mathematical, Physical and Engineering Sciences*, 368(1930), 5061-5070.

Izhikevich, E. M., and Edelman, G. M. (2008). Large-scale model of mammalian thalamocortical systems. *Proceedings of the national academy of sciences*,105(9), 3593-3598

Jarsky, T., Roxin, A., Kath, W. L., Spruston, N. (2005). Conditional dendritic spike propagation following distal synaptic activation of hippocampal CA1 pyramidal neurons. *Nature neuroscience*. 8(12):1667-76.

Jiang, X., Shen, S., Cadwell, C. R., Berens, P., Sinz, F., Ecker, A. S., et al. (2015). Principles of connectivity among morphologically defined cell types in adult neocortex. *Science* 350, aac9462. doi:10.1126/science.aac9462.

Jolivet, R., Schürmann, F., Berger, T. K., Naud, R., Gerstner, W., and Roth, A. (2008). The quantitative single-neuron modeling competition. *Biological cybernetics*, 99(4-5), 417-426.

Jonas, P., Bischofberger, J., Fricker, D., and Miles, R. (2004). Interneuron Diversity series: Fast in, fast out--temporal and spatial signal processing in hippocampal interneurons. *Trends Neurosci.* 27, 30–40.

Jones, M. W., and Wilson, M. A. (2005). Phase precession of medial prefrontal cortical activity relative to the hippocampal theta rhythm. *Hippocampus* 15, 867–873. doi:10.1002/hipo.20119.

Kandel, E.R., Markram, H., Matthews, P.M, Yuste, R. and Koch, C. (2013). Neuroscience thinks big (and collaboratively). *Nat. Rev. Neurosci.* 14, 659-664.

Kaneko, K. (1997). Dominance of Milnor Attractors and Noise-Induced Selection in a Multiattractor System. *Phys. Rev. Lett.* 78, 2736–2739. doi:10.1103/PhysRevLett.78.2736.

Katona, L., Lapray, D., Viney, T. J., Oulhaj, A., Borhegyi, Z., Micklem, B. R., et al. (2014). Sleep and movement differentiates actions of two types of somatostatin-expressing GABAergic interneuron in rat hippocampus. *Neuron* 82, 872–886.

Keren, N., Peled, N., and Korngreen, A. (2005). Constraining compartmental models using multiple voltage recordings and genetic algorithms. *Journal of neurophysiology*, 94(6), 3730-3742.

Kirson, E.D. and Yaari, Y. (2000). Unique properties of NMDA receptors enhance synaptic excitation of radiatum giant cells in rat hippocampus. *J. Neurosci.* 20, 4844-4854

Klausberger, T., and Somogyi, P. (2008). Neuronal diversity and temporal dynamics: the unity of hippocampal circuit operations. *Science* 321, 53–57.

Knopp, A., Kivi, A., Wozny, C., Heinemann, U., and Behr, J. (2005). Cellular and network properties of the subiculum in the pilocarpine model of temporal lobe epilepsy. *Journal of Comparative Neurology*, 483(4), 476-488.

Kolarov, K. (1997, April). Landscape ruggedness in evolutionary algorithms. In Evolutionary Computation, 1997*., IEEE International Conference on* (pp. 19-24). IEEE.

Komendantov, A.O. and Ascoli, G.A. (2009). Dendritic excitability and neuronal morphology as determinants of synaptic efficacy. *J. Neurophysiol.* 101, 1847-166.

Komendantov, A. O., Venkadesh, S., Rees, C. L., Wheeler, D. W., Hamilton, D. J., and Ascoli, G. A. (2019). Quantitative firing pattern phenotyping of hippocampal neuron types. *Sci. Rep.* 9, 17915. doi:10.1038/s41598-019-52611-w.

Krichmar, J.L., Velasquez, D. and Ascoli, G.A. (2006). Effects of beta-catenin on dendritic morphology and simulated firing patterns in cultured hippocampal neurons. *Biol. Bull.* 211, 31-43.

Krueppel, R., Remy, S., and Beck, H. (2011). Dendritic integration in hippocampal dentate granule cells. *Neuron* 71, 512–528.

Kumar, S.S. and Buckmaster, P.S. (2006). Hyperexcitability, interneurons, and loss of GABAergic synapses in entorhinal cortex in a model of temporal lobe epilepsy. *J. Neurosci.* 26, 4613-4623.

Lane, B. J., Samarth, P., Ransdell, J. L., Nair, S. S., and Schulz, D. J. (2016). Synergistic plasticity of intrinsic conductance and electrical coupling restores synchrony in an intact motor network. *Elife* 5. doi:10.7554/eLife.16879.

Ledergerber, D., and Larkum, M. E. (2010). Properties of layer 6 pyramidal neuron apical dendrites. *J. Neurosci*. 30, 13031–13044.

Lee, S.Y., Földy, C., Szabadics, J. and Soltesz, I. (2011). Cell-type-specific CCK2 receptor signaling underlies the cholecystokinin-mediated selective excitation of hippocampal parvalbumin-positive fast-spiking basket cells. *J. Neurosci.* 31, 10993-11002.

LeMasson, G., and Maex, R. (2001). Introduction to equation solving and parameter fitting. Computational neuroscience: realistic modeling for experimentalists. CRC Press, London, 1-23.

Leroy, F., Lamotte d'Incamps, B., Imhoff-Manuel, R.D. and Zytnicki, D. (2014). Early intrinsic hyperexcitability does not contribute to motoneuron degeneration in amyotrophic lateral sclerosis. *eLife* 3, e04046; 10.7554/eLife.04046.

Lisman, J.E. (1997). Bursts as a unit of neural information: making unreliable synapses reliable. *Trends Neurosci.* 20, 38-43.

Llinás, R.R. (1988). The intrinsic electrophysiological properties of mammalian neurons: insights into central nervous system function. *Science* 242, 1654-1664.

London, M., Schreibman, A., Häusser, M., Larkum, M.E. and Segev, I. (2002). The information efficacy of a synapse. *Nat. Neurosci.* 5, 332-340.

Lübke, J., Frotscher, M., and Spruston, N. (1998). Specialized electrophysiological properties of anatomically identified neurons in the hilar region of the rat fascia dentata. *Journal of neurophysiology*, 79(3), 1518-1534.

Luke, S., et al. (2015). "Ecj: A java-based evolutionary computation research system." Downloadable versions and documentation can be found at the following url: http://cs. gmu. edu/eclab/projects/ecj.

Lydersen, S., Fagerland, M. W., and Laake, P. (2009). Recommended tests for association in 2×2 tables. *Stat. Med*. 28, 1159–1175.

Lynch, E. P., and Houghton, C. J. (2015). Parameter estimation of neuron models using in-vitro and in-vivo electrophysiological data. *Frontiers in neuroinformatics* 9:10. doi:10.3389/fninf.2015.00010

Ma, Z., Turrigiano, G. G., Wessel, R., and Hengen, K. B. (2019). Cortical Circuit Dynamics Are Homeostatically Tuned to Criticality In Vivo. *Neuron*. doi: 10.1016/j.neuron.2019.08.031.

Maffei, A., and Fontanini, A. (2009). Network homeostasis: a matter of coordination. *Curr. Opin. Neurobiol.* 19, 168–173.

Magee, J. C., and Cook, E. P. (2000). Somatic EPSP amplitude is independent of synapse location in hippocampal pyramidal neurons. *Nat. Neurosci*. 3, 895–903.

Mainen, Z. F, Carnevale, N. T, Zador, A. M, Claiborne, B. J, and Brown, T. H. (1996). Electrotonic architecture of hippocampal CA1 pyramidal neurons based on three-dimensional reconstructions [Online]. *Journal of neurophysiology* 76: 1904–1923.

Mainen, Z.F. and Sejnowski, T.J. (1996). Influence of dendritic structure on firing pattern in model neocortical neurons. *Nature* 382, 363-366.

Marder, E., and Prinz, A. A. (2002). Modeling stability in neuron and network function: the role of activity in homeostasis. *Bioessays*. 24(12):1145-54.

Marder, E., and Goaillard, J. M. (2006). Variability, compensation and homeostasis in neuron and network function. *Nature Reviews Neuroscience*. doi: 10.1038/nrn1949.

Marder, E. (2011). Variability, compensation, and modulation in neurons and circuits. *Proc. Natl. Acad. Sci.* U. S. A. 108 Suppl 3, 15542–15548.

Markram, H. *et al.* (2004). Interneurons of the neocortical inhibitory system. *Nat. Rev. Neurosci.* 5, 793-807

Markram, H., Muller, E., Ramaswamy, S., Reimann, M. W., Abdellah, M., Sanchez, C. A., et al. (2015). Reconstruction and Simulation of Neocortical Microcircuitry. *Cell* 163, 456–492. doi: 10.1016/j.cell.2015.09.029.

Masukawa, L.M., Benardo, L.S. and Prince, D.A. (1982). Variations in electrophysiological properties of hippocampal neurons in different subfields. *Brain Res.* 242, 341–344.

McCormick, D.A., Connors, B.W., Lighthall, J.W. and Prince, D.A. (1985). Comparative electrophysiology of pyramidal and sparsely spiny stellate neurons of the neocortex. *J. Neurophysiol.* 54, 782-806.

McNaughton, B.L., Barnes, C.A. and O'Keefe, J. (1983). The contributions of position, direction, and velocity to single unit activity in the hippocampus of freely-moving rats. Exp. Brain Res. 52, 41-49.

McDougal, R. A., Morse, T. M., Carnevale, T., Marenco, L., Wang, R., Migliore, M., et al. (2017). Twenty years of ModelDB and beyond: building essential modeling tools for the future of neuroscience. *J. Comput. Neurosci*. 42, 1–10.

Mercer, A., Botcher, N. A., Eastlake, K., and Thomson, A. M. (2012). SP–SR interneurones: A novel class of neurones of the CA2 region of the hippocampus. *Hippocampus*, 22(8), 1758-1769.

Migliore, M. and Shepherd, G.M. (2005). Opinion: an integrated approach to classifying neuronal phenotypes. *Nat. Rev. Neurosci.* 6, 810-818.

Migliore, R., Lupascu, C. A., Bologna, L. L., Romani, A., Courcol, J.-D., Antonel, S., et al. (2018). The physiological variability of channel density in hippocampal CA1 pyramidal cells and interneurons explored using a unified data-driven modeling workflow. *PLoS Comput. Biol*. 14, e1006423.

Morgan, R. J., and Soltesz, I. (2008). Nonrandom connectivity of the epileptic dentate gyrus predicts a major role for neuronal hubs in seizures. *Proc. Natl. Acad. Sci.* U. S. A. 105, 6179–6184.

Morris, C., and Lecar, H. (1981). Voltage oscillations in the barnacle giant muscle fiber. *Biophysical journal*, 35(1), 193.

Mott, D. D., Turner, D. A., Okazaki, M. M., and Lewis, D. V. (1997). Interneurons of the dentate–hilus border of the rat dentate gyrus: morphological and electrophysiological heterogeneity. *The Journal of neuroscience*, 17(11), 3990-4005.

Nageswaran, J. M., Dutt, N., Krichmar, J. L., Nicolau, A., and Veidenbaum, A. V. (2009). A configurable simulation environment for the efficient simulation of

large-scale spiking neural networks on graphics processors. *Neural Networks*, 22(5), 791-800.

Neubrandt, M. *et al.* (2018). Single bursts of individual granule cells functionally rearrange feedforward inhibition. *J. Neurosci.* 38, 1711-1724

Nicholson, D. A., Trana, R., Katz, Y., Kath, W. L., Spruston, N., and Geinisman, Y. (2006). Distance-dependent differences in synapse number and AMPA receptor expression in hippocampal CA1 pyramidal neurons. *Neuron* 50, 431–442.

Oizumi, M., Albantakis, L., and Tononi, G. (2014). From the phenomenology to the mechanisms of consciousness: Integrated Information Theory 3.0. *PLoS Comput. Biol.* 10, e1003588.

O'Keefe, J. and Dostrovsky, J. (1971). The hippocampus as a spatial map. Preliminary evidence from unit activity in the freely-moving rat. Brain Res. 34, 171-175.

O'Keefe, J., and Recce, M. L. (1993). Phase relationship between hippocampal place units and the EEG theta rhythm. *Hippocampus* 3, 317–330. doi:10.1002/hipo.450030307.

O'Leary, T., van Rossum, M. C. W., and Wyllie, D. J. A. (2010). Homeostasis of intrinsic excitability in hippocampal neurones: dynamics and mechanism of the response to chronic depolarization: Homeostatic regulation of intrinsic excitability. *J. Physiol*. 588, 157–170.

Oláh, S., Füle, M., Komlósi, G., Varga, C., Báldi, R., Barzó, P., et al. (2009). Regulation of cortical microcircuits by unitary GABA-mediated volume transmission. *Nature* 461, 1278–1281. doi:10.1038/nature08503.

Oliva, A. A, Jiang, M., Lam, T., Smith, K. L, and Swann, J. W. (2000). Novel hippocampal interneuronal subtypes identified using transgenic mice that express green fluorescent protein in GABAergic interneurons. *The Journal of Neuroscience.* 20(9):3354-68.

Padmanabhan, K., and Urban, N. N. (2010). Intrinsic biophysical diversity decorrelates neuronal firing while increasing information content. *Nature neuroscience*. 13: 1276–1282.

Pawelzik, H., Hughes, D. I., and Thomson, A. M. (2002). Physiological and morphological diversity of immunocytochemically defined parvalbumin-and cholecystokinin-positive interneurones in CA1 of the adult rat hippocampus. *Journal of Comparative Neurology*, 443(4), 346-367.

Petilla Interneuron Nomenclature Group, Ascoli, G. A., Alonso-Nanclares, L., Anderson, S. A., Barrionuevo, G., Benavides-Piccione, R., et al. (2008). Petilla terminology: nomenclature of features of GABAergic interneurons of the cerebral cortex. *Nat. Rev. Neurosci*. 9, 557–568.

Pierce, J. P., McCloskey, D. P., and Scharfman, H. E. (2011). Morphometry of hilar ectopic granule cells in the rat. *J. Comp. Neurol*. 519, 1196–1218.

Pinsky, P. F., and Rinzel, J. (1994). Intrinsic and network rhythmogenesis in a reduced Traub model for CA3 neurons. *J. Comput. Neurosci*. 1, 39–60.

Podlogar, M., and Dietrich, D. (2006). Firing pattern of rat hippocampal neurons: a perforated patch clamp study. *Brain research*, 1085(1), 95-101.

Poirazi, P., Brannon, T. and Mel, B.W. (2003). Arithmetic of subthreshold synaptic summation in a model CA1 pyramidal cell. *Neuron* 37, 977-987

Pozzorini, C., Mensi, S., Hagens, O., and Naud, R. (2015). Automated high-throughput characterization of single neurons by means of simplified spiking models. *PLoS computational biology*. 11.6: e1004275.

Price, C. J, Cauli, B., Kovacs, E. R, and Kulik, A. (2005). Neurogliaform neurons form a novel inhibitory network in the hippocampal CA1 area. *Journal of Neuroscience*. 25.29: 6775-6786.

Rathour, R. K., and Narayanan, R. (2014). Homeostasis of functional maps in active dendrites emerges in the absence of individual channelostasis. *Proc. Natl. Acad. Sci.* U. S. A. 111, E1787-96.

Rees, C. L., Wheeler, D. W., Hamilton, D. J., White, C. M., Komendantov, A. O., and Ascoli, G. A. (2016). Graph Theoretic and Motif Analyses of the Hippocampal Neuron Type Potential Connectome. *eNeuro* 3. doi:10.1523/ENEURO.0205-16.2016.

Remy, S. and Spruston N. (2007). Dendritic spikes induce single-burst long-term potentiation. *Proc. Natl. Acad. Sci. U S A* 104, 17192-17197

Rossant, C., Goodman, D., Platkiewicz, J., and Brette, R. (2010). Automatic fitting of spiking neuron models to electrophysiological recordings. *Frontiers in neuroinformatics*. 4: 2. doi: 10.3389/neuro.11.002.2010

Rossant, C., Goodman, D.F., Fontaine, B., Platkiewicz, J., Magnusson, A. K., and Brette, R. (2011). Fitting neuron models to spike trains. *Frontiers in Neuroscience*. 5: 9. doi:10.3389/fnins.2011.00009

Rounds, E. L., Scott, E. O., Alexander, A. S., De Jong, K. A., Nitz, D. A., and Krichmar, J. L. (2016). An Evolutionary Framework for Replicating Neurophysiological Data with Spiking Neural Networks. In *International conference on Parallel Problem Solving from Nature – PPSN XIV* (pp. 537-547): Springer International Publishing

Rudy, J.W. and Sutherland, R.J. (1989). Configural association theory: The role of the hippocampal formation in learning, memory, and amnesia. Psychobiology 17, 129–144.

Rudy, J.W. and Sutherland, R.J. (1995). Configural association theory and the hippocampal formation: an appraisal and reconfiguration. Hippocampus 5, 375-389.

Rudy, B., Fishell, G., Lee, S., and Hjerling-Leffler, J. (2011). Three groups of interneurons account for nearly 100% of neocortical GABAergic neurons. *Dev. Neurobiol*. 71, 45–61. doi:10.1002/dneu.20853.

Saraga, F., Wu, C. P., Zhang, L., and Skinner, F. K. (2003). Active dendrites and spike propagation in multicompartment models of oriens-lacunosum/moleculare hippocampal interneurons. *The Journal of physiology*, 552(3), 673-689.

Savanthrapadian, S. et al. (2014). Synaptic properties of SOM- and CCK-expressing cells in dentate gyrus interneuron networks. *J. Neurosci.* 34, 8197-8209

Savić, N., Sciancalepore, M. (2001). Electrophysiological characterization of "giant" cells in stratum radiatum of the CA3 hippocampal region. *Journal of neurophysiology*. 85(5):1998-2007.

Schulz, D. J, Goaillard, J. M., and Marder, E. (2006). Variable channel expression in identified single and electrically coupled neurons in different animals. *Nature neuroscience* doi: 10.1038/nn1639.

Shanahan, M. (2010). Metastable chimera states in community-structured oscillator networks. *Chaos* 20, 013108. doi:10.1063/1.3305451.

Sik, A., Penttonen, M., Ylinen, A. and Buzsáki, G. (1995). Hippocampal CA1 interneurons: an *in vivo* intracellular labeling study. *J. Neurosci.* 15, 6651-6665.

Sik, A., Ylinen, A., Penttonen, M. and Buzsáki, G. (1994). Inhibitory CA1-CA3-hilar region feedback in the hippocampus. *Science* 265, 1722-1724.

Skaggs, W. E., McNaughton, B. L., Wilson, M. A., and Barnes, C. A. (1996). Theta phase precession in hippocampal neuronal populations and the compression of temporal sequences. *Hippocampus* 6, 149–172.

Smith, G. D., Cox, C. L., Sherman, S. M., and Rinzel, J. (2000). Fourier analysis of sinusoidally driven thalamocortical relay neurons and a minimal integrate-and-fire-or-burst model. *Journal of Neurophysiology*, 83(1), 588-610.

Smith, M. and Perrier, J.F. (2006). Intrinsic properties shape the firing pattern of ventral horn interneurons from the spinal cord of the adult turtle. *J. Neurophysiol.* 96, 2670-2677.

Song, C. *et al.* (2013). Stuttering interneurons generate fast and robust inhibition onto projection neurons with low capacity of short-term modulation in mouse lateral amygdala. *PLoS One* 8, e60154; 10.1371/journal.pone.0060154.

Spruston, N., Lübke, J. and Frotscher, M. (1997). Interneurons in the stratum lucidum of the rat hippocampus: an anatomical and electrophysiological characterization. *J. Comp. Neurol.* 385, 427-440.

Spruston, N. (2008). Pyramidal neurons: dendritic structure and synaptic integration. *Nat. Rev. Neurosci.* 9, 206–221.

Staff, N.P., Jung, H.Y., Thiagarajan, T., Yao, M. and Spruston, N. (2000). Resting and active properties of pyramidal neurons in subiculum and CA1 of rat hippocampus. *J. Neurophysiol.* 84, 2398-2408

Stevenson, I. H., and Kording, K. P. (2011). How advances in neural recording affect data analysis. *Nat. Neurosci.* 14, 139–142. doi:10.1038/nn.2731.

Szabadics, J. and Soltesz, I. (2009). Functional specificity of mossy fiber innervation of GABAergic cells in the hippocampus. *J. Neurosci.* 29, 4239-4251

Szabadics, J., Varga, C., Brunner, J., Chen, K., and Soltesz, I. (2010). Granule cells in the CA3 area. *The Journal of Neuroscience*, 30(24), 8296-8307.

Tamas, G., Lorincz, A., Simon, A. and Szabadics, J. (2003). Identified sources and targets of slow inhibition in the neocortex. *Science* 299, 1902-1905.

Tebaykin, D. et al. (2018). Modeling sources of interlaboratory variability in electrophysiological properties of mammalian neurons. *J. Neurophysiol.* 119, 1329-1339

Teeter, C., Iyer, R., Menon, V., Gouwens, N., Feng, D., Berg, J., et al. (2018). Generalized leaky integrate-and-fire models classify multiple neuron types. *Nat. Commun*. 9, 709.

Tognoli, E., and Kelso, J. A. S. (2014). The metastable brain. *Neuron* 81, 35–48. doi: 10.1016/j.neuron.2013.12.022.

Tononi, G. (2012). Integrated information theory of consciousness: an updated account. *Arch. Ital. Biol.* 150, 293–329.

Tononi, G., Boly, M., Massimini, M., and Koch, C. (2016). Integrated information theory: from consciousness to its physical substrate. *Nat. Rev. Neurosci.* 17, 450–461.

Traub RD, Whittington MA, Stanford IM, and Jefferys JG. (1996). A mechanism for generation of long-range synchronous fast oscillations in the cortex. *Nature* 383: 621–4.

Tricoire, L., Pelkey, K. A., Erkkila, B. E., Jeffries, B. W., Yuan, X., and McBain, C. J. (2011). A blueprint for the spatiotemporal origins of mouse hippocampal interneuron diversity. *J. Neurosci*. 31, 10948–10970.

Tripathy, S. J., Padmanabhan, K., Gerkin, R. C., and Urban, N. N. (2013). Intermediate intrinsic diversity enhances neural population coding. *Proceedings of the National Academy of Sciences* 110(20): 8248-8253.

Tripathy, S.J., Burton, S.D., Geramita, M., Gerkin, R.C. and Urban, N.N. (2015). Brain-wide analysis of electrophysiological diversity yields novel categorization of mammalian neuron types. *J. Neurophysiol.* 113, 3474-3489.

Tsuda, I. (2001). Toward an interpretation of dynamic neural activity in terms of chaotic dynamical systems. *Behav. Brain* Sci. 24, 793–810; discussion 810-48. Available at: https://www.ncbi.nlm.nih.gov/pubmed/12239890.

Tsuda, I., and Umemura, T. (2003). Chaotic itinerancy generated by coupling of Milnor attractors. *Chaos* 13, 937–946. doi:10.1063/1.1599131.

Tsuda, I., Fujii, H., Tadokoro, S., Yasuoka, T., and Yamaguti, Y. (2004). Chaotic itinerancy as a mechanism of irregular changes between synchronization and desynchronization in a neural network. *J. Integr. Neurosci.* 3, 159–182. Available at: https://www.ncbi.nlm.nih.gov/pubmed/15285053.

Tsuda, I. (2009). Hypotheses on the functional roles of chaotic transitory dynamics. *Chaos* 19, 015113. doi:10.1063/1.3076393.

Tsuda, I. (2015). Chaotic itinerancy and its roles in cognitive neurodynamics. *Curr. Opin. Neurobiol.* 31, 67–71. doi: 10.1016/j.conb.2014.08.011.

Turrigiano, G., Abbott, L. F., and Marder, E. (1994). Activity-dependent changes in the intrinsic properties of cultured neurons. *Science* 264, 974–977.

Van der Meer, M. A. A., and Redish, A. D. (2011). Theta phase precession in rat ventral striatum links place and reward information. *J. Neurosci*. 31, 2843–2854. doi:10.1523/JNEUROSCI.4869-10.2011.

Van der Velden, L., van Hooft, J. A., and Chameau, P. (2012). Altered dendritic complexity affects firing properties of cortical layer 2/3 pyramidal neurons in mice lacking the 5-HT3A receptor. *J. Neurophysiol.* 108, 1521–1528.

Van Geit, W., Achard, P., and De Schutter, E. (2007). Neurofitter: a parameter tuning package for a wide range of electrophysiological neuron models. *BMC Neuroscience*, 8(Suppl 2), P5.

Van Geit, W., De Schutter, E., and Achard, P. (2008). Automated neuron model optimization techniques: a review. *Biological cybernetics*, 99(4-5), 241-251.

Venkadesh, S., and Ascoli, G. A. (2017). "Computational Modeling as a Means to Defining Neuronal Spike Pattern Behaviors," in *Mathematical and Theoretical Neuroscience: Cell, Network and Data Analysis,* eds. G. Naldi and T. Nieus (Cham: Springer International Publishing), 25–43.

Venkadesh, S., Komendantov, A. O., Listopad, S., Scott, E. O., De Jong, K., Krichmar, J. L., et al. (2018). Evolving Simple Models of Diverse Intrinsic Dynamics in Hippocampal Neuron Types. *Front. Neuroinform*. 12, 8.

Venkadesh, S., Komendantov, A. O., Wheeler, D. W., Hamilton, D. J., and Ascoli, G. A. (2019). Simple models of quantitative firing phenotypes in hippocampal neurons: Comprehensive coverage of intrinsic diversity. *PLoS Comput.* Biol. 15, e1007462. doi: 10.1371/journal.pcbi.1007462.

Vida, I., Halasy, K., Szinyei, C., Somogyi, P., and Buhl, E. H. (1998). Unitary IPSPs evoked by interneurons at the stratum radiatum-stratum lacunosum-moleculare border in the CA1 area of the rat hippocampus in vitro. *J. Physiol*. 506, 755–773.

Wheeler, D. W., White, C. M., Rees, C. L., Komendantov, A. O., Hamilton, D. J., and Ascoli, G. A. (2015). Hippocampome.org: A knowledge base of neuron types in the rodent hippocampus. *eLife*, e09960.

Williams, P. A., Larimer, P., Gao, Y., and Strowbridge, B. W. (2007). Semilunar granule cells: glutamatergic neurons in the rat dentate gyrus with axon collaterals in the inner molecular layer. *The Journal of Neuroscience*, 27(50), 13756-13761.

Wittner, L., and Miles, R. (2007). Factors defining a pacemaker region for synchrony in the hippocampus. *The Journal of physiology*. 584(3):867-83.

Xu, W. *et al.* (2012). Distinct neuronal coding schemes in memory revealed by selective erasure of fast synchronous synaptic transmission. *Neuron* 73, 990-1001

Yang, X.-S. (2010). *Nature-inspired Metaheuristic Algorithms*. Luniver Press.

Yu, Q., Tang, H., Tan, K. C., and Yu, H. (2014). A brain-inspired spiking neural network model with temporal encoding and learning. *Neurocomputing*, 138, 3-13.

Yu, Y., Shu, Y., and McCormick, D. A. (2008). Cortical action potential backpropagation explains spike threshold variability and rapid-onset kinetics.*The Journal of Neuroscience,* 28(29), 7260-7272.

Yun, S. H., Gamkrelidze, G., Stine, W. B., Sullivan, P. M., Pasternak, J. F., Ladu, M. J., et al. (2006). Amyloid-beta1-42 reduces neuronal excitability in mouse dentate gyrus. *Neurosci. Lett.* 403, 162–165.

Zeldenrust, F., Wadman, W.J. and Englitz, B. (2018). Neural coding with bursts - current state and future perspectives. *Front. Comput. Neurosci.* 48; 10.3389/fncom.2018.00048

Zemankovics, R., Káli, S., Paulsen, O., Freund, T. F., and Hájos, N. (2010). Differences in subthreshold resonance of hippocampal pyramidal cells and interneurons: the

role of h-current and passive membrane characteristics. *The Journal of physiology*, 588(12), 2109-2132.

Zippo, A.G., Biella, G.E. (2015). Quantifying the number of discriminable coincident dendritic input patterns through dendritic tree morphology. *Sci. Rep.* 5, 11543; doi: 10.1038/srep11543

Zucker, R.S., Regehr, W.G. (2002). Short-term synaptic plasticity. *Annu. Rev. Physiol.* 64, 355-405

BIOGRAPHY

Siva Venkadesh Iyappan Latha received his Bachelor of Technology in Information Technology from College of Engineering, Guindy, Anna University in 2007. He was employed as a software engineer for three years and received his Master of Science in Artificial Intelligence from University of Georgia, Athens in 2012.